POLITECNICO DI TORINO

Masters degree in aerospace engineering

Master's thesis

Thermal probe enhanced with pulsed plasma discharges for efficient ice penetration

Supervisors:
Prof. Lorenzo Casalino[1]
Fernando Mier-Hicks[2]
Gareth Meirion-Griffith[2]

Candidate:
Guglielmo Daddi[1][2]

Affiliations:
[1]Politecnico di Torino
[2]Jet Propulsion Laboratory, California Institute of Technology.

May 2020

Abstract

Plasma drilling is a deep drilling technology which leverages electrical discharges to fracture rocks and sediments. In this work, plasma drilling is investigated as a performance enhancer for existing thermal-probe technology for use in planetary sub-glacial exploration missions. The hypothesis is that the cracking of ice induced by the spark discharges results in a local reduction of thermal conductivity capable of decreasing the conductive thermal losses that make up the majority of a thermal probe's power budget in cryogenic ice conditions.
Firstly, a simulation pipeline for melt probe performance is adapted to mimic the effects of plasma drilling on the ice surrounding a thermal probe. The simulation predicts the power necessary to keep a thermal probe moving at a certain descent velocity and can predict the expected energy savings as a function of thermal conductivity reduction and cracked region extent. Variation of ambient conditions, probe geometry and mission time are also investigated.
Subsequently, the design iterations of a bench-top system used to store and distribute of energy $80J$ at $40kV$ are described. This system is at heart of the experimental portion of this work. The first application of the high-voltage setup is an experimental campaign tailored at finding the thermal conductivity reduction prompted by discharging in an ice sample. A commercially available thermal properties analyzer is used to collect thermal conductivity data.
The efforts made to perform a direct comparison between a melt probe and plasma-enhanced thermal probe are also described. Accordingly, the design, construction and testing of a simple melt probe made out of commercial off the shelf components are presented. Subsequently, a high-voltage module capable of delivering pulsed-plasma discharges is designed and tested; this module can be integrated in the melt probe.
In conclusion, the experimental setup intended to house the direct comparison between these two systems is also presented.

Contents

Chapter 1

Introduction

1.1 Glacial and sub-glacial environments in the solar system

Hydrogen and Oxygen are widespread elements in the solar system and their most valuable combination, water (H_2O), appears in all of its phases on some planets, moons and smaller celestial bodies. [1]
From a scientific point of view, studying water deposits is key to understanding the solar system's origin and evolution; in addition, the presence of liquid water as a solvent is one of the prerequisites for life as we know it and therefore any mission with astrobiological focus is expected to look in and around water deposits. [2] [3] [4]
Furthermore, the search for water on planetary bodies is destined to gain importance as signalled by the explicit reference to Astrobiology in the 2023-2032 Decadal Survey. [5]
Ice deposits deserve particular attention as their study might contribute to both astrobiology and planetary science while occasionally being simply obstacles to surpass in order to access sub-glacial liquid water environments such as lake Vostok in Antarctica [6]
The search for life in the solar system has focused attention on two main targets: Ocean worlds and Mars.

Ocean Worlds are celestial bodies on which there is a global liquid water ocean [7]. The strongest evidence in favor of the existence of subterranean liquid water oceans has been found for Europa, Enceladus and Titan which are moons orbiting respectively Jupiter and Saturn. The very existance of a liquid water oceans in such cold and remote regions of the solar system might be surprising, especially as it is not explainable alone by residual heat from the moon's formation or by radioactive decay, but requires also to consider the heat generated by the dissipative action of tidal forces [8].

Europa is a Jovian moon and appears from the surface as a deeply inhospitable icy landscape mangled by linear fractures and irradiated by charged particles captured in Jupiter's magnetic field. It is believed that Europa's ice sheets bury a global salt-water ocean at dephs of 1-10 km [9] [3]. This ocean reaches depths of 80-170 km and interacts directly with a rocky silica floor. The rock-water interface is particularly interesting as it might provide the same kind of hydrothermal-vent environment that might have given rise to life on Earth [10] [11].

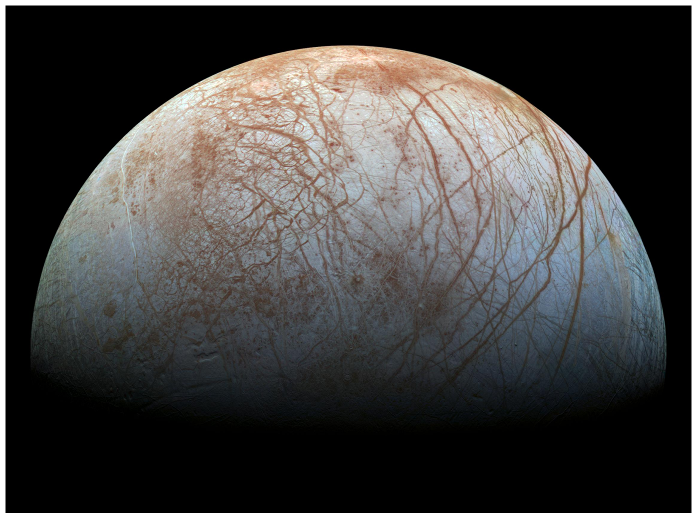

Figure 1.1: Europa's surface as seen from the Galileo spacecraft. Credit: NASA/JPL-Caltech/SETI Institute

Enceladus is a moon of Saturn and is quite similar to Europa in appearance and structure. The ice layer in Enceladus' case is thicker than Europa's and is believed to reach depths of 30-40 km. The most peculiar aspect of Enceladus is that there are plumes of water being ejected from some of the planet's linear fractures. The water in these plumes is believed to have origin in the subterranean ocean and when sampled by the Cassini spacecraft showed evidence of liquid-rock interaction in the ocean's depths [12].

Titan is the least appealing candidate for an ocean-access missions as its ice crust is buried beneath a layer of organic material which would pose a significant technical challenge to penetrate. In addition, Titan's superficial ice sheet is the thickest out of the three planets (55-80 km) and the ocean floor is composed by a high pressure phase of ice which would exclude the possibility of hydrothermal vents.

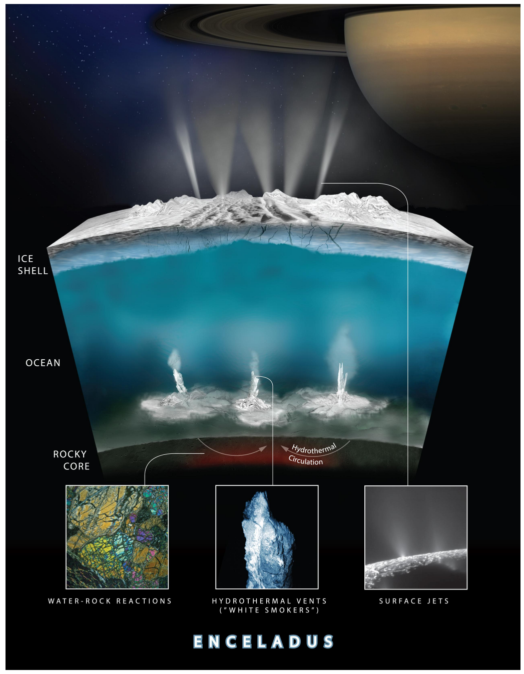

Figure 1.2: Artist rendering of Enceladus' internal structure. Credit: NASA/JPL-Caltech

Mars' northern and souther polar environments are composed by residual ice caps on which seasonsal $CO2$ ice accumulates and then, after a sintering phase, sublimates from the bottom-up creating gayser-like plumes. The residual ice caps are several kilometers thick and are shaped like domes; the frozen layers are made up of sandy-ice deposited over the span of 10^5-10^9 years [13].
Asides from seasonal and residual ice, the Martian southern polar region is characterized by the presence of large subsurface $CO2$ ice deposits beneath water ice layers [14].

Simlarly to Earth's ice caps, the Mars' polar layered deposits contain a historic record of the planet's climate which can be derived by measuring D/H and $^{18}O/^{16}O$ ratios for each layer [15] [16]. Understanding Mars' climactic record might provide insight in the future evolution of Earth's cryosphere and could also clarify the connection between climate and the variation of Mars' orbital parameters. Furthermore, considering that there is evidence pointing at an early environment favourable to life on Mars[17], a better understanding of the planet's climactic history might also contribute to astrobiological research by providing a better understanding on past periods of habitability.

In addition to scientific questions, Mars is also a candidate for future human colonization [18] [19]. Therefore, gaining historical and present knowledge on the planet's cryosphere could help the colonization effort by enriching climate predictive models and provide a better understanding on how to utilize the Mars' polar resources for in-situ resource utilization.

Figure 1.3: Image of the Mars' North Polar Layered Deposits (NPLD) as seen by the HiRISE instrument on board of the Mars Reconnaissance Orbiter. Credit NASA

1.2 Accessing planetary ice

Accessing glacial and sub-glacial environments poses significant technological challenges. Classic mechanical drilling methods such as ice core are complex, heavy and require bulky support infrastructure, maintenance and drilling fluids which makes them poorly suited to reach great depths on remote planetary bodies. [20]
Other examples of drilling techniques used succesfully for glacial exploration on Earth that do not translate well for planetary exploration are Hot Water Drilling and Coil Tube Drilling [21]. Hot Water Drilling consists in creating a bore hole by pumping hot water (80-90C) directly in the ice and require vast amounts of power to achieve a sufficient flow rate (in the order of several MW); asides from being impractical from a power generation standpoint, Hot Water Drilling would also be complicated by a vacuum environment such as that on Europa's surface. Coil Tube Drilling is a mechanical drilling technique used in niche aspects of petroleum extraction and while being slightly more promising than the other techniques (a fully functional, 46 ton system has been proposed in [21]), is still highly impractical to integrate in an interplanetary probe. [22]

An innovative ice penetration technique was proposed in 1962 by Philberth [23] to further glaciological understanding by capturing the vertical temperature gradient of an ice sheet. This technology consists in using a tethered hot-point which melts a cavity in the ice to achieve penetration rate. The fundamentals of self-contained, hot-point drills have remained substantially the same with only minor improvements over the past decades.

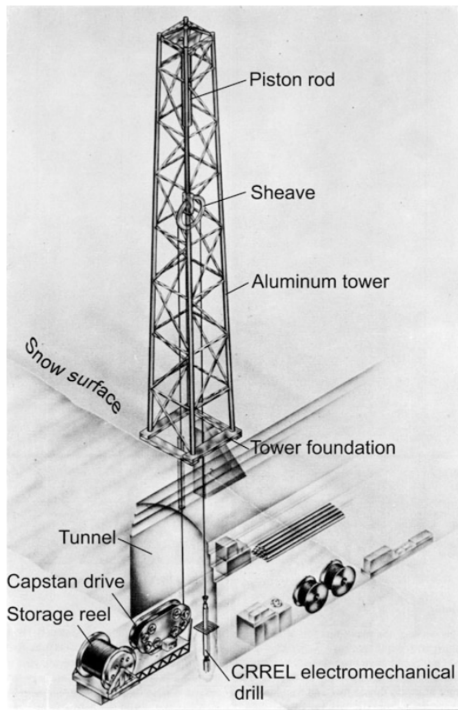

Figure 1.4: Complexity of the coring support system deployed at the Byrd station in Antartica to penetrate with an electromechanical drill 7100 ft of ice as described in [24]. Figure is adapted from [20]

Applying thermal drilling to space exploration requires to address a number of key problematics such as operation in ambient pressures extremes, communication with Earth, power generation and transmission, low gravitational force, ice contaminations, sidewall refreezing *etc.* [22]
Firstly, a melt probe's descent rate is dependent on gravity [25]. For small moons such as Enceladus, the relatively low gravitational force will significantly decrease the maximum descent velocity at a given power.
If, on the other hand, there are sediments in the ice - such as is the case for Mars' Polar Layered Deposits - melt water will concentrate contaminants in proximity to the probe's tip, locally reducing thermal conductivity and both diminishing descent rate and possibly also creating dangerous hot-spots within the tip heaters which could lead to failure of var-

ious internal components if not properly monitored by temperature sensors.

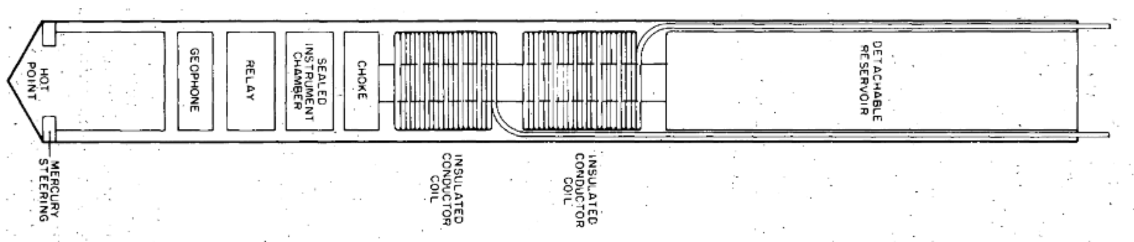

Figure 1.5: Schematic of a Philberth probe. Adapted from [26]

While High ambient pressures pose structural challenges, low ambient pressures can be just as problematic for the initial penetration phases on planetary bodies, where surface pressure is too low for the stability of water's liquid phase; in this case, melting is substituted directly by sublimation which is both an order of magnitude more energy intensive due to the latent heat of evaporation and might lead to tip overheating due to insufficient conductive heat transfer. Reference [27] shows the results of experiments simulating thermal probe penetration under Mars' polar regions pressure (615 Pa) which yielded encouraging evidence pointing at the existence of a temporary water layer in proximity of the tip. When ice accumulates on an ice cap, the superficial layers are not compacted by pressure and therefore are characterized by a porous structure (”firm” ice). Thermal probe performance is drastically impaired by firm ice as the water layer which is crucial to heat transfer can seep into the pores therefore leaving voids around the probe. In severe cases, the probe might stall and major hot-spots might arise, potentially leading to hardware-damage.
The success of the first phases of a melt probe's descent in a vacuum environment depends on the porosity of the superficial ice. If the ice sufficiently permeable and water vapor is allowed to exit, melting could never set-in due to a build up of partial water vapour pressure.[28]
The magnitude of the challenges relating to melt-probe performance justifies the tendency to include multiple drilling technologies in a single system for space applications.

The most mature Ocean access technology is the ”Cryobot” concept, developed at JPL to investigate the Europa's subterranean ocean. This concept is an evolution of the regular thermal probe because melting is still the primary mechanism which enables downward motion, but the power source is moved on-board to avoid power transmission losses. Heat and electricity are generated by the decay of Plutonium Oxide ($^{238}PuO_2$) in Radioisotope Thermal Generators (RTGs) which have been widely used in planetary exploration and are under continual development to increase their efficiency and power density [29]. Contrarily to classical Electric power systems, the Cryobot is optimized to produce moslty waste heat which is conducted outward directly to the ice thus eliminating the chance of heater-failure that has plagued thermal drills since the very beginning [30].

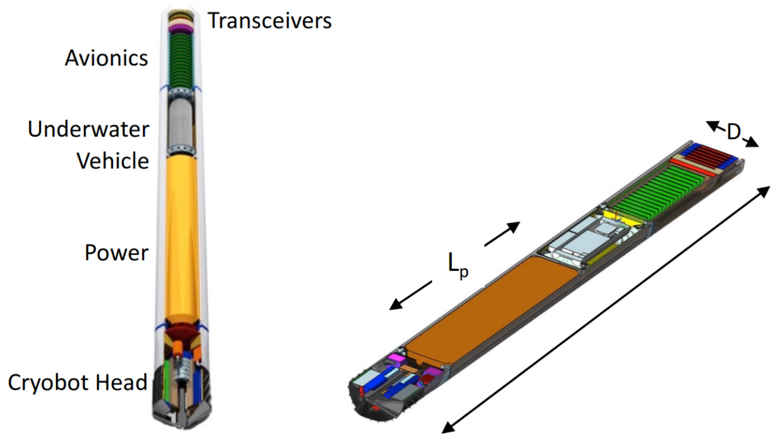

Figure 1.6: Schematic of a nuclear powered Cryobot. Adapted from [31]

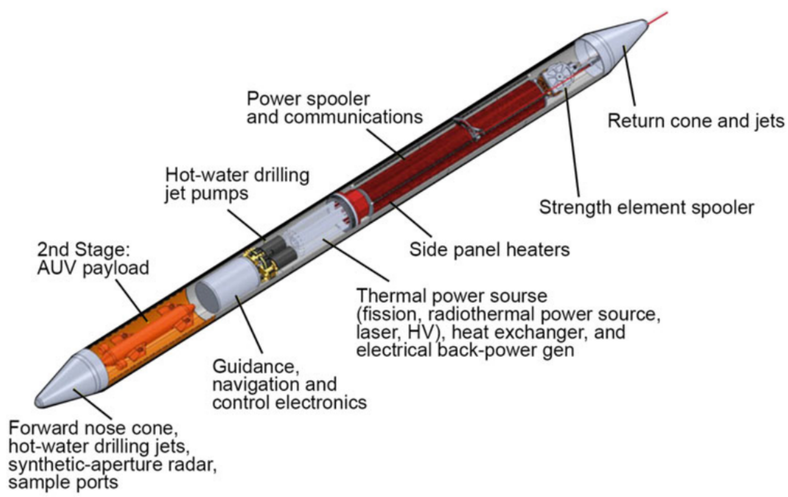

Figure 1.7: Stone Aerospace's two stage, water jetting Cryobot called SPINDLE. Adapted from [32]

While moving through ice, the Cryobot could use an on board Chemical laboratory to

gain understanding on the Europa's ice sheets. Once the Cryobot has reached the subsurface ocean, the idea is to deploy a swimming probe called "Hydrobot" which would rove the ocean analyzing water samples and look for past or present signs of life or hydrothermal vents. The Hydrobot could navigate and look for hydrothermal vents by listening with a hydrophore and imaging via a sonar and the presence of life in the ocean could be addressed by using instruments capable of investigating the backscatter coming from particulate. [33] More recent iterations of the Cryobot concept are improved by adding performance-enhancing features such as a mechanical drill heads or water-jetting [31].
Interstingly, a cryobot specific instrument suite called "Wireline Analysis Tool for Subsurface Observation of Northern ice sheets" or in short WATSON is also under development. WATSON's purpose is to characterise organic material and bacteria embedded in an ice sheet. The instrument can quickly take fluorescence maps of large samples and subsequently focus on intersting regions with a Raman scattering analysis [34].
It is useful to look at this instrument suite as it gives an idea of the degree of miniaturization achievable for a self-contained sub-glacial access mission. The diameter of WATSON is in fact in the order of 10 cm.

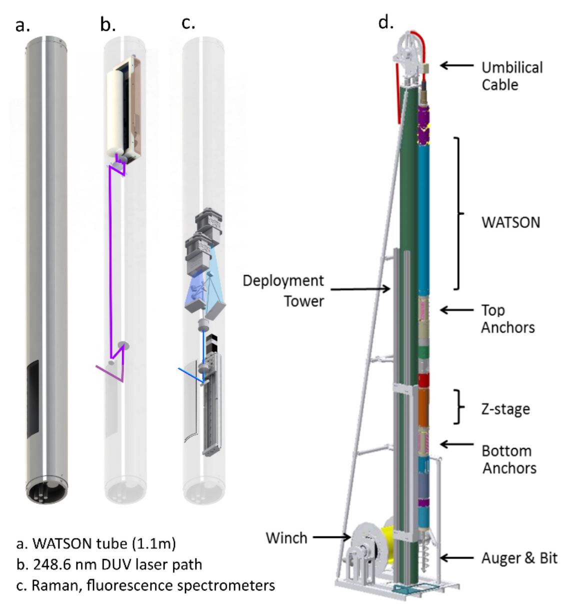

Figure 1.8: Schematic of the WATSON instument suite. Adapted from [34]

WATSON might be integrated in a hybrid drilling technology developed at Honeybee robotics called SLUSH (Search for Life Using a Submersible Heated drill) [34]. This

concept consists in a tethered thermo-mechanical drill which uses mechanical drilling to fracture and remove the ice beneath and around the probe. Thermal power partially melts the chips creating a slushy liquid that refreezes behind the probe. The mechanical drill is highly desirable to penetrate cryogenic ice (50-110K) as it increases the efficiency of ice-removal [35].
Electrical and Thermal Power are provided by an on-board kilowatt-class self-moderating fission reactor whose output can be actively toggled [36].

Figure 1.9: Render of the external and internal model of the honeybee's SLUSH probe. Credit: Honeybee robotics

Another approach to Cryobot technological development has been undertaken by Stone Aerospace in the VALKYRIE project (Very-deep Autonomous Laser-powered Kilowatt-class Yo-yoing Robotic Ice Explorer).
The main difference with previous thermal probes is that the power generated by a lander is delivered to the penetrator in in the form of a continuous wave laser via a fiber optic cable. This energy is subsequently partly directed to a heat exchanger for a water-jetting system and partly transformed in electrical energy through a photo-voltaic cell [37]. Navigation is provided by a forward-looking Synthetic Aperture Radar which uses the thin water layer around the probe as a resonant cavity to improve performace [38].
A hybrid approach to the penetration of Europa's ice sheets is presented in [39]. Mechanical chipping is enabled by a rotating saw blade mounted on a rotating tip assembly which

cuts a hemispherical volume of ice beneath the probe. The ice chips are molten by the heat generated by a Plutonium Oxide brick and the resulting water is pumped behind the probe to refreeze. Water samples are collected in very small canisters and then fed back to the lander via a spooling Alluminum tube for analysis thus reducing the probe's volume and power requirements.

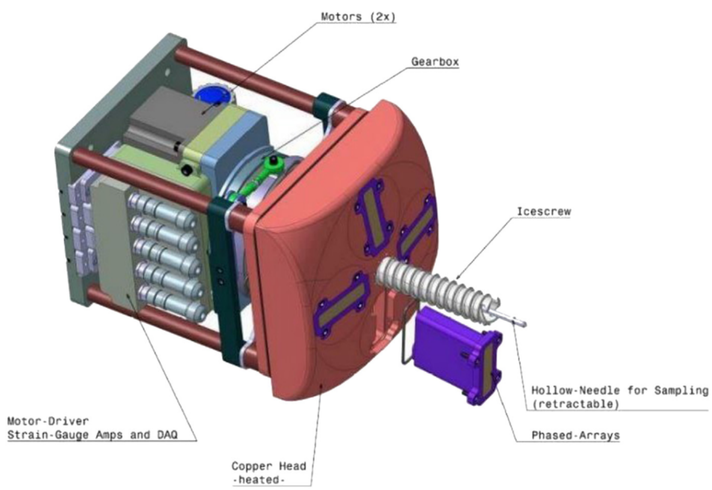

Figure 1.10: Technical drawing of the EnEx-IceMole head. Adapted from [40]

A planetary subglacial mission concept has been developed under "Enceladus Explorer" (EnEx) funding [40] by leveraging the field-tested technology developed for the IceMole project which focuses on contaminant-free glacial access. [41]
The IceMole is based both on thermal drilling and mechanical propulsion achieved via a hollow rotating ice screw mounted on the probe's tip which creates a force that pulls the probe towards the ice thus improving the thermal contact between ice and tip consequently enabling upward motion for sample return.
Steering is achieved by differential head heating and sidewall heaters prevent refreezing and facilitate direction change. Navigation, obstacle avoidance and attitude determination are provided by an Inertial Measuring Unit combined with an ultrasonic phased arrays and surface-mounted acoustic sensors [42].
Smaller scale missions which leverage pure hot-point thermal drill technology and trade maximum depth for a mission cost reduction have also been proposed. Refernce [43] describes a small instrumented probe driven by battery power capable of achieving 3 meters of penetration on Europa's surface.
Reference [44] proposes an even smaller thermal drill capable of penetrating the first 10

cm of Europa's ice.
In conclusion, it should be clear that planetary glacial and sub-glacial environments pose significant technical challenges and that any technology that may increase thermal probe performance is greatly desirable.

1.3 The plasma drilling concept

Plasma drilling consists in inducing an electrostatic discharge in an incompressible medium interposed between two electrodes thus generating a shock-wave which fractures the surrounding material. In practice, when dielectric breakdown occurs, a plasma channel is formed in the material. Ions and electrons are accelerated by the strong electric field and the subsequent avalanche of collisions heats up the plasma causing a large spike in pressure which propagates as a shock-wave.

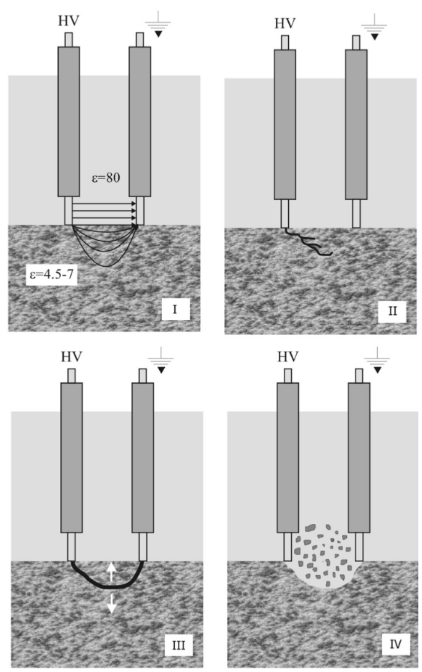

Figure 1.11: Schematic of spark discharge and subsequent material fracturing. Adapted from [45]

Unsurprisingly, the first applications of this concept, starting in the 1950's, are all focused on mineral and petroleum extraction. These first attempts yielded unsatisfactory drilling performance due to the fact that the discharge was being induced in a liquid and ore fracturing would occur when the shock-wave impacted the material [46] [47]. Reference [48] shows that when sparking in an incompressible fluid, a large bubble forms when and subsequently collapses creating jets and shock-waves which in turn can damage a surrounding medium such as ice.

The commercial viability of this drilling technology has been reached by gradually improving the efficiency of material removal by employing shock-wave focusing techniques. [49]
Electrical discharges have not only been used to fracture rocks and sediments, but also to break up ice samples. A practical application plasma drilling to the shipping industry can be seen in references [50] and [51] where the performance of an ice-breaker ship is improved by discharging ahead of the ship's bow.
Reference [45] describes a more recent application of spark discharges to create small channels in a rock sample.
Additionally, a practical example of plasma drilling becoming a commercial technology can be seen in the effort of GA drilling to excavate deep boreholes in rock by employing a high-power plasma discharges [52].

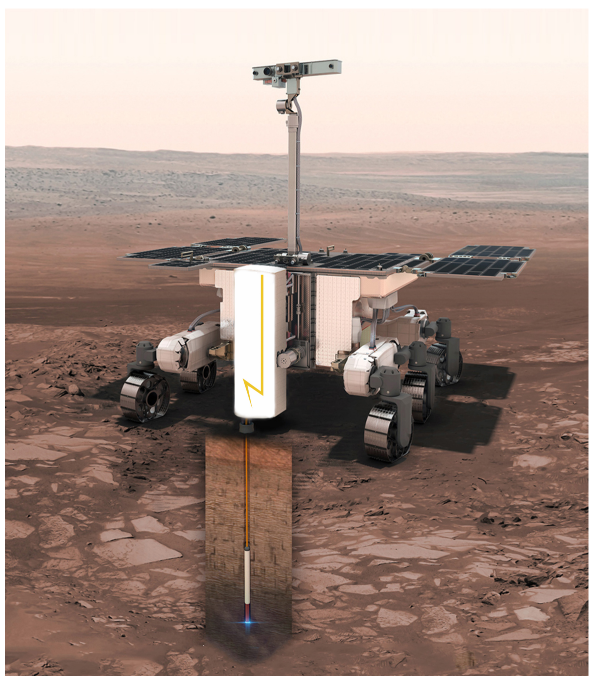

Figure 1.12: Plasma drilling on Mars enabled by Zaptec's technology. Credit: ESA, Zaptec

A US-based corporation called Tetra has been researching and developing electro-hydraulic drilling for the past 20 years. Their concept consists in using pulsed plasma discharges in an incompressible fluid (water or mud) and focusing the resulting shock-wave towards a material in close proximity to the cutting head. [53] [54]
The first proposal to use the plasma drilling technology for subsurface access celestial bodies other than Earth comes from the company Zaptec Inc. [55]. The idea is to use a cutting head or "mole" which uses high energy plasma discharges and is free to advance. The system is tethered to a lander which serves the purpose of power generation. This system's power consumption is in the order of 1-2 kW and would ideally be suited for accessing deep water lakes on the surface of Mars or asteroid and moon mining.

This thesis outlines the first 9 months of JPL's effort to assess the feasibility of applying pulsed plasma discharges to enhance planetary sub-glacial access technologies. As stated in the previous section, any space-born ice penetration mission will probably include multiple technological solutions aimed at overcoming the challenges posed by low surface pressure, firm ice, the hardness of cryogenic ice, sediments *etc.*.
In this framework, plasma discharges are envisioned as a thermal-probe performance enhancer which could reduce overall mission power requirement by severely cracking and potentially reducing to small chips the ice surrounding the probe. In addition, the plasma discharges could be seen as a substitute or complement to the mechanical portion of a hybrid thermo-mechanical system such as SLUSH, EnEx-IceMole or JPL's own Cryobot.
The reference mission concept used throughout this work is a Martian mission aimed at accessing the first 100-150 meters of the Polar Layered Deposits therefore revealing up to 150 kY of the planet's climactic record.
It is important thought to keep in mind that the ultimate scope of this work is to probe the technology itself.

Chapter 2

Model

2.1 Background

A high-level theoretical investigation is here sought out with the intent of identifying the mechanisms which could make a plasma drill more efficient than a regular thermal probe and quantifying the expected savings. The results from this analysis also inform the plasma drill prototype's design and suggest specific physical quantities to monitor during experiments.

Theoretical thermal probe performance estimation is a well developed topic in literature which inherited instruments and theories derived originally to investigate contact melting and heat conduction; the first thermal-probe specific performance comes from Aamot's work in 1967 [56]. This is the base of most thermal probe models and it identifies minimum power components that a probe must expend to penetrate an ice sheet at velocity v. Firstly, there is the heat flux which goes to melting the ice column directly beneath the system itself.

$$P_{min} = \rho v A[h_f + c_p(\Delta T)]$$

Where ρ is the ice density, c_p is the ice's specific heat at constant pressure and ΔT is the difference between undisturbed ice temperature and 273.15 K (melting point at a pressure of 1 atmosphere).
The second power consumption component is the heat lost through the sidewalls and can be quantified using Charslaw's and Jaeger's work [57] in which the heat conduction of a circular cylinder at fixed temperature T, immersed in an infinite region with thermal conductivity k and diffusivity K is given by:

$$q_L = \frac{4kT}{a\pi} \int_0^\infty e^{-Ku^2 t} \frac{\mathrm{d}u}{u[J_0^2(au) + Y_0^2(au)]}$$

The numerical solution to this complicated integral is a heat flux profile which is large in proximity of the probe's tip and gradually decreases while approaching the tail section.

In practice, the minimum power consumption is given by the sum of tip and sidewall powers. It has been demonstrated that Aamot's model underestimates the power required to penetrate cryogenic ice sheets (at a temperature of $100K$) due to increased conductive losses towards the sides [58].

Thermal probes are inherently multi-physics phenomena in which there is interaction between a heat-source under gravity's action, an ice-water mixture and an ice bulk which is in itself a complicated material to model accurately.

Subsequent modelling efforts have expanded on this initial work both by adding to the physical phenomena captured by the model and/or using other modelling methods. An example of physical model nuancing can be seen in reference [25], in which the close contact melting theory is applied to model thermal probe performance while also investigating the role of gravity and hydrodynamic effects in the water layer separating tip from ice-bulk in addition to an energy balance.
Multi-physics Finite element analysis methods have also been used to study the interaction between ice and probe. Reference [59] for instance uses elasto-plastic theory in conjunction with a standard heat conduction problem to derive temperature fields and stress-strain distributions around a probe and subsequently find an optimal tip head shape [60].
References [61] and [62] model the presence of a growing ice-water region laying in close proximity to the probe's surface and investigates temperature fields with varying probe geometry and initial temperature.
It is unlikely that a pure-thermal probe will be employed in planetary exploration, as the risk of having sediment accumulate and thermally insulate the tip from the rest of the ice causing complete probe stall warrants the use of additional technological solutions. Reference [58] for instance describes JPL's use of START CCM to perform a CFD multi-physics analysis and compute descent rates of a cryobot with a water jetting tip.

If regular-thermal probe performance is not simple to estimate, the addition of in-ice discharging further complicates the physical phenomena involved. The pressure pulse that is generated by current flowing in the plasma channel formed between electrodes is a highly instationary phenomenon that results in a difficultly predictable fracture pattern. In addition, ice could break up in small particles ("ice chipping") which could start moving in the water layer between probe and ice. Simulating the discharges' effects would be in itself a very difficult and time consuming task and any theoretical results would likely be highly debatable. On the other hand, if the each discharge's outcome is assumed as given information, the performance estimation can be greatly simplified, as the problem's structure is reduced to a regular thermal probe model in a modified ice domain. Im this way a ”system level” approach can be used which takes as an input the ”cracked region” characteristics and estimates the overall probe power requirements as a function of descent velocity.

2.2 Thermal probe model

In order to spare resources and time, a pre-existing finite element analysis simulation pipeline written using MATLAB's pde toolbox and developed by JPL to estimate thermal probe performance was adapted to mimic a plasma drill.

The simulation consists in solving the steady state thermal conduction / advection equation around a pore using the finite element method. The main objective of the simulation is to compute the temperature field around a thermal probe surrounded by a thin water layer, moving at a specific velocity and using wall temperature gradients to compute the power input required to maintain this condition.

2.2.1 Assumptions

The simulation looks at the icy region around a cylindrically shaped ”pore”, not the probe itself. In fact, the pore contains both the probe and a thin surrounding water layer that enables movement. This means that the complexity of the probe-water-ice interface is substituted by a geometric assumption on the probe + water system.

As a further simplification, the water layer is considered to be of negligible dimensions with respect to the probe's own radius; the temperature of this layer is kept at 273.15 K by efficient heater use. If the power distribution along the probe's heaters is optimized, neglecting the water layer is fair as in this way, the channel needs to be just a few millimeters thick in order to enable probe movement.

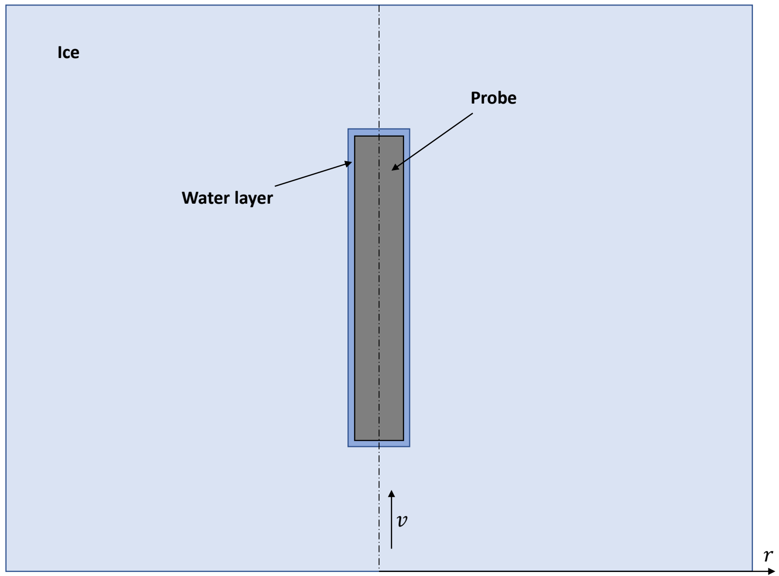

Figure 2.1: Finite element analysis schematic

2.2.2 Geomtery

As the pore is characterized by axial symmetry, the computational domain can be restricted to a 2-D surface delimited radially (along the coordinate r) on one side by the symmetry axis and on the other side by an arbitrary R_{inf} and by a lower and upper bound in the vertical (z) direction.

Along the z axis, the two bounds are determined as a multiple of the probe's radius that allows to capture as much of the "disturbed" temperature-field as possible, while avoiding to waste computational resources in capturing too much of the undisturbed temperature field upstream with respect to the probe or any wake-like structure downstream. R_{inf} is computed from a function of probe length and velocity which ensures that the temperature at R_{inf} can be safely assumed as undisturbed by the probe's presence. Specifically, if the probe's length increases and velocity decreases, R_{inf} increases.

The simulation also allows for a tapered nose and tail probe geometry in order to take advantage of the warm wake's presence by adding probe volume for "free". Tapered geometries are not considered in this work to reduce geometric parameters at a minimum.

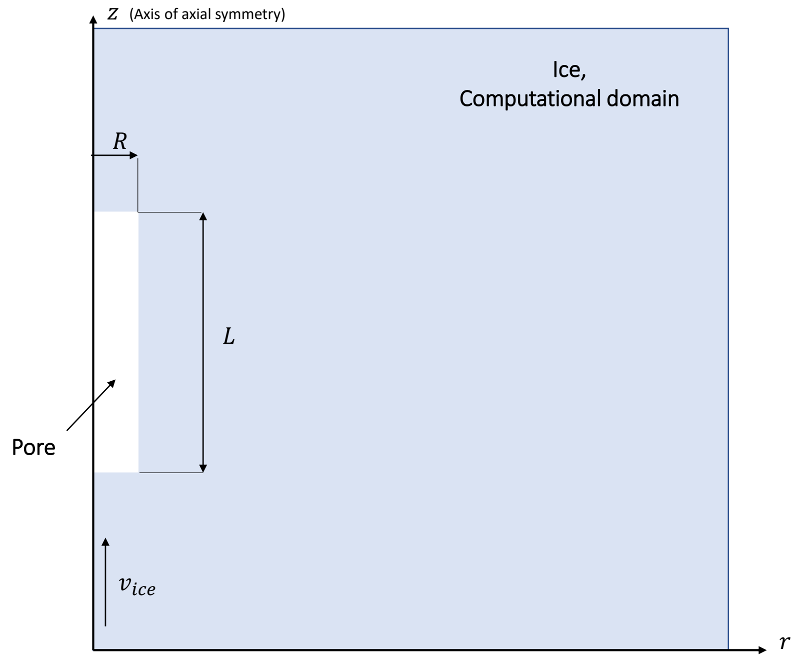

Figure 2.2: Computational domain

2.2.3 Meshing

MATLAB's pde toolbox has very limited built-in meshing capabilities and, with this geometry, can only construct a uniformly distributed mesh with the variable element size. It has to be noted that the accuracy of the simulation's results is dependent on the mesh being fine enough to fully capture temperature gradients where they are present. A uniformly distributed fine mesh would certainly do the job if sufficiently fine, but at an unacceptably high computational cost.
Consequently, to obtain accurate results while still maintaining acceptable performance, computational nodes are placed more densely in the pore's proximity, where the largest temperature gradients are expected to be. This occurs by using an open-source mesh generator called "DistMesh", developed by Per-Olof Persson and Gilbert Strang at MIT.
The mesh generator uses a fictitious force which depends on the desired type of mesh and computes iteratively the truss structure spanning the whole domain that satisfies equilibrium conditions under that force. The mesh nodes are then placed in the truss structure nodes [63].

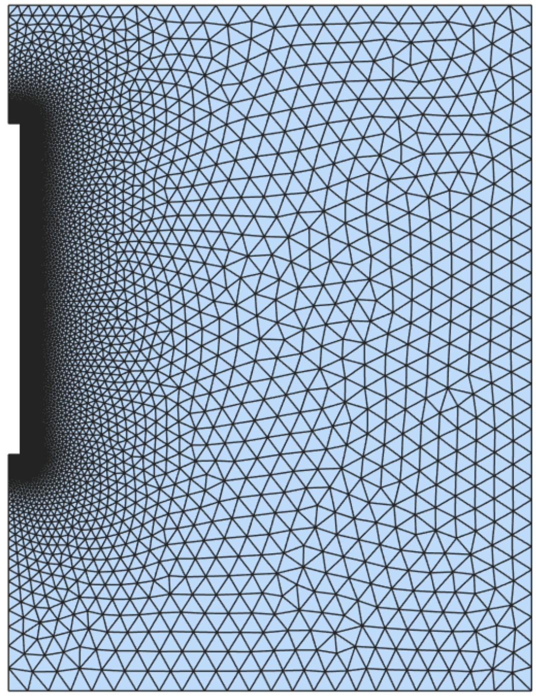

Figure 2.3: Mesh

2.2.4 Governing Equations

Physically, the situation can be seen as a heat conduction problem in a moving reference frame; this can be modelled with the advection-diffusion equation:

$$\frac{1}{r}\frac{\partial}{\partial r}\left(-kr\frac{\partial T}{\partial r}\right)+\frac{\partial}{\partial z}\left(-k\frac{\partial T}{\partial z}\right)+c_p\rho v\frac{\partial T}{\partial z}=0 \tag{2.1}$$

Where:

- T is ice temperature
- $k = k(T)$ is thermal conductivity W/mK and is a function of temperature.
- $c_p = c_p(T)$ is the specific heat at constant pressure of ice and is a function of temperature.
- $\rho = \rho(T)$ is the density of ice and is a function of temperature.

- $\mathcal{V}$ is the probe's velocity along the z axis.
- The temperature-dependent properties of cryogenic ice are taken from Ulamec et. al. [2007] [22].

The strong non-linearity of this partial differential equation is clearly visible in the temperature-dependence of k, c_p and ρ.

2.2.5 Boundary Conditions

The pore's edges are kept at a constant temperature of $273.15K$. As stated earlier, this condition stems from the assumption of optimal heater power distribution.
The ice boundary at R_{inf} is kept at the constant, undisturbed Temperature of the ice sheet. Depending on what celestial body or what depth is under investigation, this value can be easily modified. It must be noted that there can be significant vertical temperature gradients in large ice sheets. Usually, temperature is at its minimum close to the surface where it is actively cooled by the atmosphere and as depth increases, the increased pressure causes also a temperature increase; this is so dramatic that the cryogenic ice on the Jovian moon Europa can reach temperatures of up to 270 K at depths of 10-15 km. [64]. A full mission analysis would have to introduce a depth-dependent temperature profile. In this project there is no need to add depth-dependent ice temperature, as the focus is on probing plasma drilling under every ambient condition, not tied to any specific mission profile. As a reference, this analysis uses an in penetrating Martian polar layered ice deposit up to a depth of 100 meters, which is not sufficient to drive any significant temperature gradient. Along the z-axis and through the symmetry axis, there is zero normal heat-flux boundary condition (Homogeneous Neumann BC), which simulates inflow and outflow conditions.

2.2.6 Power consumption estimation

The finite element analysis solution to the conduction-advection heat equation returns a temperature field. The power necessary to keep the probe moving in ice has to be computed as the heat lost to maintain the steady-state temperature gradients along the pore's boundaries over time. This heat loss is easily computed starting from the temperature field and using Fourier's conduction law. The pde toolbox allows to easily evaluate and interpolate the heat flux anywhere in the computational region, without having to implement Fourier's law.

$$q = -k\nabla T = \left[\frac{W}{m^2}\right] \tag{2.2}$$

Heating power requirement = q*Area

the local heat flux q is sampled along the pore's boundary to get a point-by-point description of the heat loss. Integrating this value over the pore's surface results in the overall power consumption.

2.3 Plasma drill model

A plasma-enhanced thermal drill is considered to behave similarly to a thermal probe; the main assumption being that cracking creates a region of reduced thermal conductivity (k) around the pore, which abruptly transitions back to the un-cracked value of k at a radial distance of R_{cracked} from the probe's sidewalls following a near-discontinuity as can be seen in figure 2.4 by looking at the $k(r)$ curve.

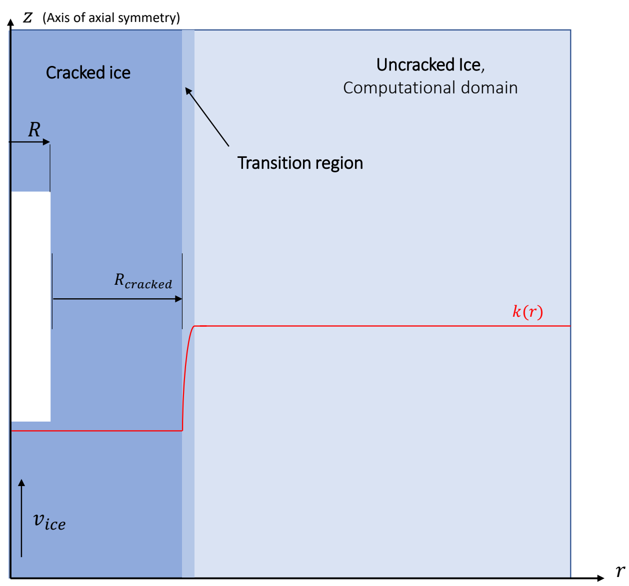

Figure 2.4: Cracked ice model

2.3.1 Parameter Definition

Two non-dimensional parameters are introduced to keep notation clean. They are the reduction factor K^* and the cracked region extent R^* which are defined as:

$$R^* = \frac{R_{\text{cracked}}}{R}$$

$$K^* = \frac{K_{\text{cracked}}}{K_{\text{uncracked}}}$$

The reduction factor indicates what proportion of the un-cracked ice's thermal conductivity is present in the cracked region; R^* represents, in terms of multiples of the probe's radius, the cracked region's extent from the probe's sidewalls.

2.3.2 Modifications to the thermal probe model

The reduction in thermal conductivity is introduced in the model by multiplying the scalar field $k(T)$ by a function of the radial coordinate $f(r)$ with the following properties:

- $f(r)$ is constant and equal to the reduction factor for $r < R_{\text{cracked}} - \text{transition length}$
- $f(r)$ is constant and equal to 1 for $r > R_{\text{cracked}} + \text{transition length}$
- $f \neq f(z)$, where z is the "vertical" coordinate following the probe's length. This means that the cracked region extends both above and below the probe.

The effect of this function is therefore to reduce the thermal conductivity by a fixed amount in the "cracked ice buffer" region and to keep unaltered the regular $k(T)$ in the unaffected region.
MATLAB does not allow for pde coefficient functions to be defined in a piece-wise continuous fashion; in fact, the non-linear, stationary solver requires second order continuity in all coefficients to converge. Consequently, a sigmoid function is used to mimic a piece-wise continuous function while not giving up second order continuity. This sigmoid is defined as:

$$f(r) = K^* - (1 - K^*)\,\frac{e^{m(r-R_{\text{crack}})}}{e^{m(r-R_{\text{cracked}})} + R_{\text{crack}}} \tag{2.3}$$

Where:

- K^* is the "reduction factor". For example, $K^* = 0.5$ means that within the cracked ice buffer, thermal conductivity will be 50% of the un-cracked value.
- m controls the transition length between K^* and 1 and has a numerical value which is fine-tuned to achieve the smallest possible transition region while still avoiding the solver misinterpreting it as a discontinuity. For a 5 cm radius probe with 0.5 m length, a sufficient value of m is 500, while much larger probes require a decrease of this value. For example, a probe with $10cm$ radius and 1.2 meters length) requires an m-value of 150.
- $R_{\text{cracked}} = R^* R$ is defined as a fraction (or multiple) of the probe's radius R.

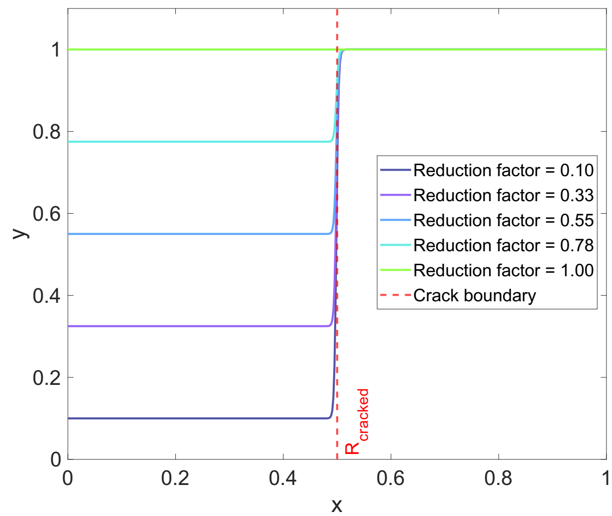

Figure 2.5: Thermal conductivity reduction function testing with various reduction factors and same cracked region extent

Figure 2.5 shows several sigmoid functions with fixed transition point and length and varying $K*$. In the figure, the near-discontinuous behaviour is particularly evident.

Ultimately, the thermal conductivity's full expression is given by the product of three components:

1. A temperature dependant thermal conductivity expression, taken from Ulamec *et. al.* 2007 [22]

$$K(T) = \frac{619.2}{T} + \frac{58646}{T^3} + 3.237e(-3) \cdot T - 1.382e(-5) \cdot T^2$$

2. A corrective term that accounts for the difference between planar and cylindrical coordinates (r).

3. A scaling function that simulates a cracked ice buffer all around the probe. $f(r)$

$$K(x,T) = K(T) \cdot r \cdot (f(r))$$

2.3.3 Standard Conditions

A set of default conditions is described to avoid having to specify simulation parameters for every result.

- Tapered tail = False
- Tapered nose = False
- Probe radius = 2.5 cm
- Probe length = 0.5 m
- Velocity = 0.1 m/h
- Tapering = False
- Ice temperature = 170 K
- K^* (if applicable) = 0.75
- R^* (if applicable) = 2

Probe geometry is chosen as the simplest shape possible (non-tapered cylinder) while probe dimensions reflect what a lightly instrumented polar ice diver might look like. Temperature is consistent with Martian polar ice temperatures and probe velocity is chosen to enable comfortably a 100 m penetration mission over the period of a Martian summer ($\sim$ 12 earth months) with spare time to perform scientific observations. Cracked region extent is somewhat of a placeholder, as reliable data on the cracking extent is not available yet. Reduction factor on the other hand is compatible with experimental measurements in the most cracked region.

2.4 Results and discussion

Some initial observations can be made by looking at the temperature fields in the computational domain (Figures 2.6a and 2.6b). Firstly, the downward motion causes the isothermal lines to be denser in proximity to the probe's frontal section. Temperature reaches an almost undisturbed state at a distance of just 4-5 times the probe's radius downwards with respect to the tip at a descent rate of 0.1 m/h. This suggests that the characteristic time of conduction is comparable to the descent velocities in analysis. As probe velocity increases, isothermal lines grow denser in front of the probe and the equations become progressively dominated by the transport term; this isothermal line structure almost resembles a thermal shock layer. Conversely, as velocity decreases, the physics become diffusion-dominated and the area influenced by the probe's presence increases.

A consequence of the outflow boundary condition is that the isothermal lines are forced to be normal to the upper surface; this causes some isothermal lines to bend unnaturally in proximity to the upper domain boundary.

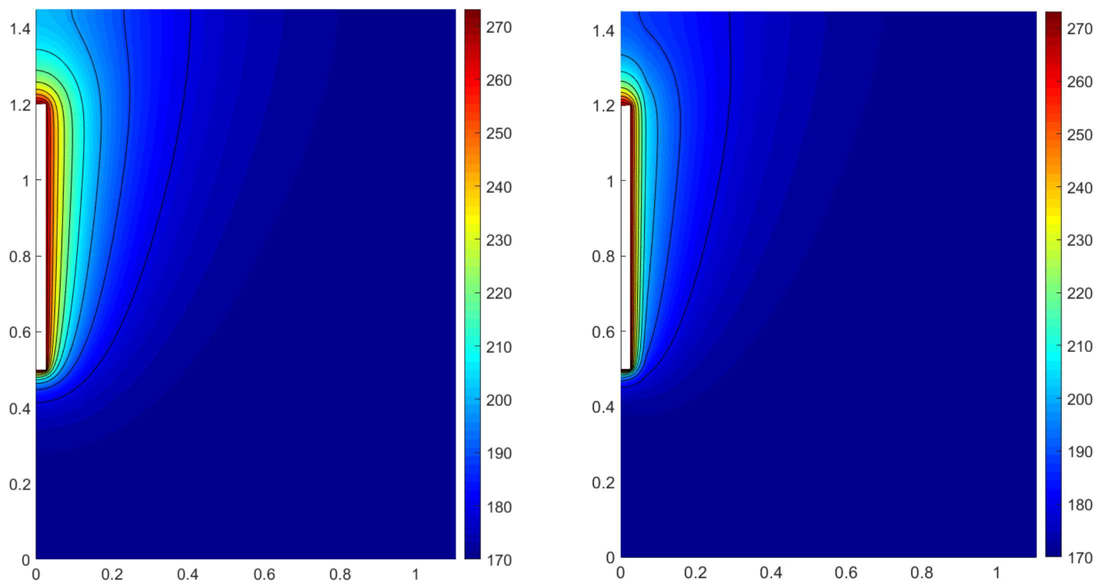

(a) Un-cracked ice

(b) Cracked ice; $K^* = 0.5$

Figure 2.6: Temperature field around the probe in standard conditions

Comparing cracked and un-cracked temperature fields shows how cracking reduces the extent at which the probe's presence is influencing the temperature field. In other words, the region of reduced thermal conductivity causes less heat dispersion, thus acting like a layer of insulating material. The cracked ice layer's thickness can be identified in figure 2.6b by noting that the isothermal lines suddenly change slope. In the figure, this behaviour is clearly visible in the area closest to the probe's tip and the non-discontinuous nature of the transition is also evident and clearly governed by the sigmoid function's "transition length" parameter. If this region were infinitesimal, the change in derivative would happen in a single point acting as a second order discontinuity.

A significant result comes from investigating the variation of power-savings as a function of both the adimensional parameters R^* and K^* as can be seen in figures 2.7a, 2.7b and 2.8. This provides intuitive understanding on the parameter's relative importance, on where to focus when trying to fine-tune the discharge's topology (if possible) and when to expect diminishing returns. Additionally, these tables can function as a reference to quickly judge expected savings form experimental data without running specific simulations.
From these figures it can be firstly noted that there are diminishing returns when the cracked region's extent gets pushed beyond 2-3 times the probe's radius. Additionally -

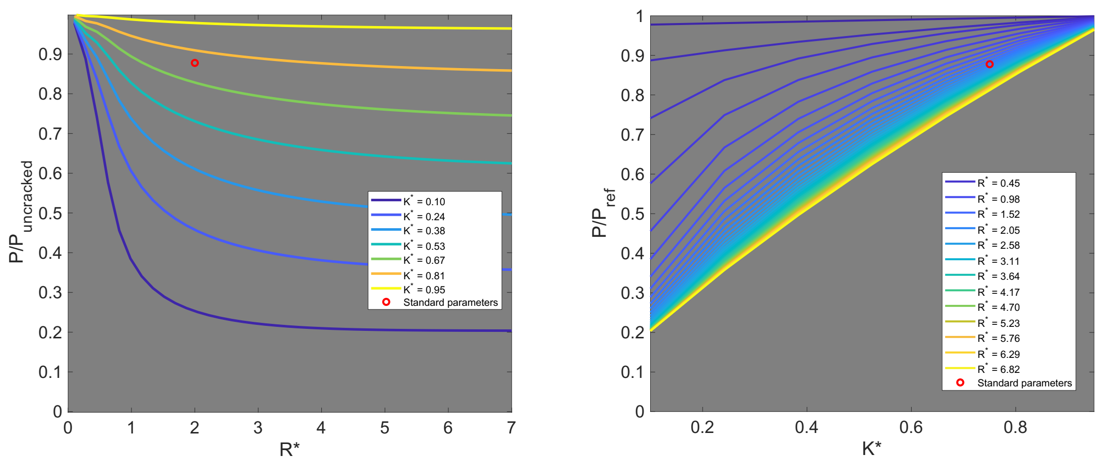

(a) (b)

Figure 2.7: Plasma drill power savings with varying R^* and K^*

as can be seen in figure 2.7a - power savings are limited when the cracked region's extend approaches infinity and reduction factor remains fixed. At fixed cracked region extent (larger than 1), it is always convenient to focus on ways to reduce the ice's thermal conductivity as much as possible (figure 2.7b).

Figure 2.8 is a synthesis of what has been described in the previous paragraphs as it depicts the possible power gains with varying $K*$ and $R*$ through a coloured contour map. It can be seen that the resulting surface resembles a quarter bowl. This means that there is an infinite number of combinations of $K*$ and $R*$ that lead to the same power gain. In addition, it can be noted that not all power savings can be reached for a a fixed K^* or R^*. Small R^* are in fact just as bad as unitary K^* at reducing overall power consumption; thus it emerges again that some effort must be placed on creating discharges which both reach out to large swaths of ice and cause significant decreases in thermal conductivity.
Diminishing returns with $R^* > 4$ are clearly visible by observing that the power ratio surface takes an inclined quasi-planar shape.

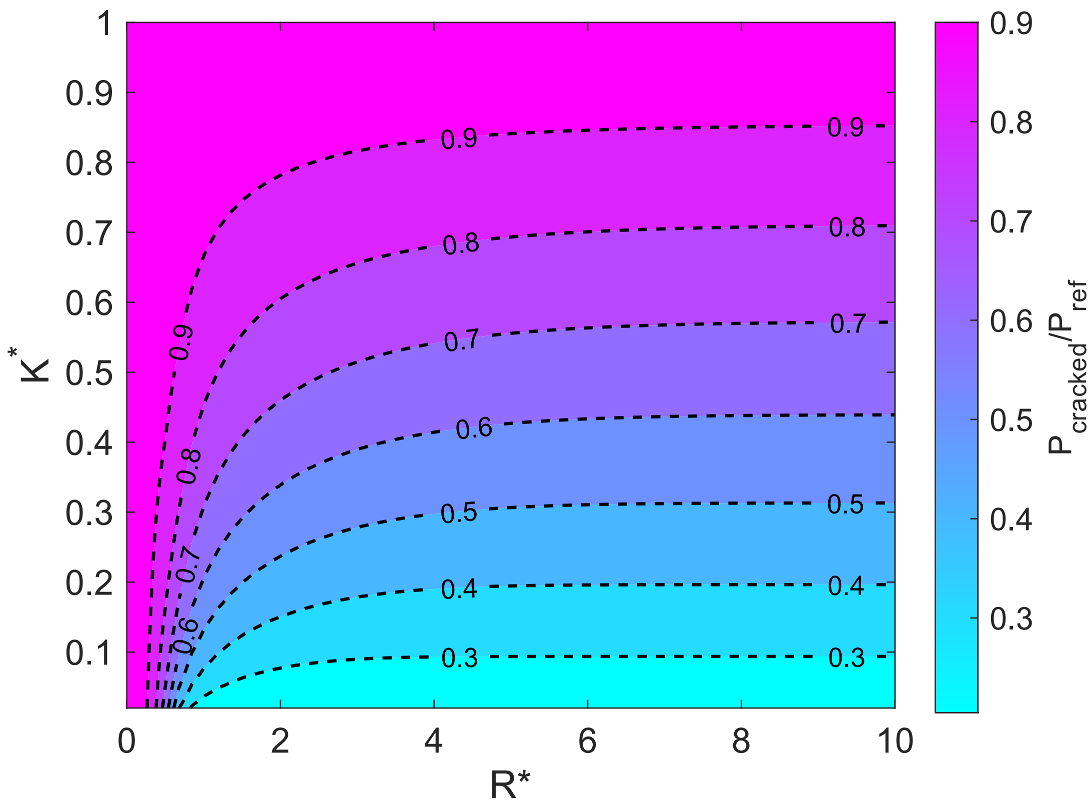

Figure 2.8: Relationship between K*, R* and power gains for a thermal probe submersed in ice at 170K

In summary, these results inform the type of discharge topology to strive for and allow an impromptu evaluation of expected power gains.

- If fine-tuning the discharge aftermath parameters is possible, the main focus should be put on achieving the lowest possible thermal conductivity region surrounding the probe. A part of the energy must also be devoted to having a cracked region extent in excess of 1-2 times the probe's radius.
- If cracking were to extend radially significantly beyond a value of $2-4R$, there would be diminishing returns on power savings and therefore some of the energy that goes into cracked region extent should be placed into thermal conductivity reduction.

- As thermal-conductivity is key to the potential advantages of a plasma drill; an effort to experimentally determine thermal conductivity variations is desirable.

Varying the ice field's undisturbed temperature (figure 2.9) shows a rapid increase in power requirements as ice temperature decreases, starting from a zero-power condition when ice Temperature approaches $273.15K$. Even the relatively small reference system would spend $1-2kW$ purely to produce enough heat to keep moving in the upper layer of Europa's ice sheets. The figure also shows that the power gap between a plasma drill and a thermal probe increases in magnitude as temperature decreases.

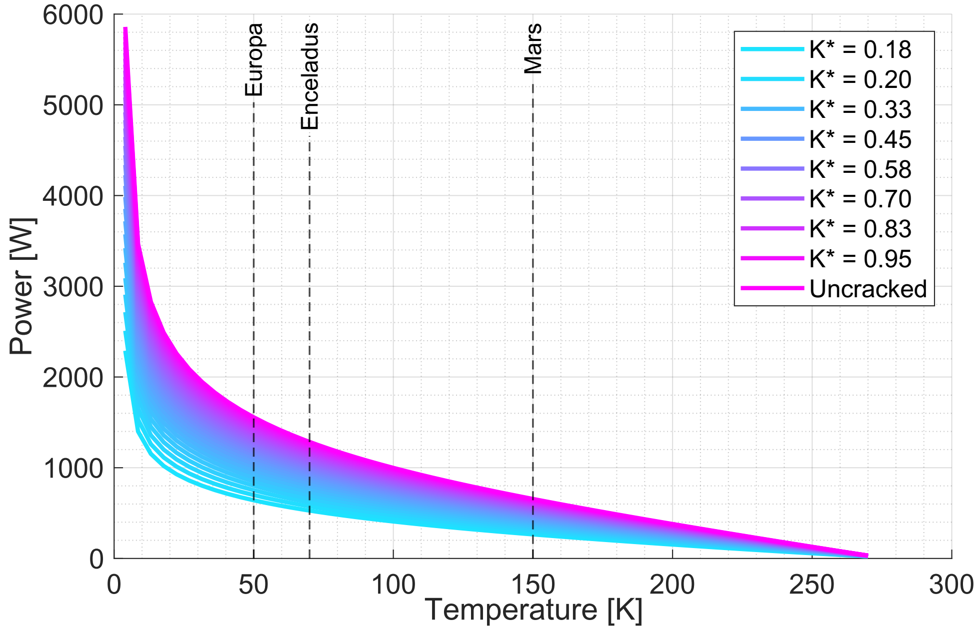

Figure 2.9: Power requirement with varying ice temperature and thermal conductivity reduction factor

The fraction of total power flowing to both tip and sidewalls is plotted in figure 2.10 and, as expected, sidewall losses rapidly become the predominant factor when ice temperature decreases. For planetary ices, such as those on Europa or Mars, sidewall heating accounts for more than 90% the total power budget.

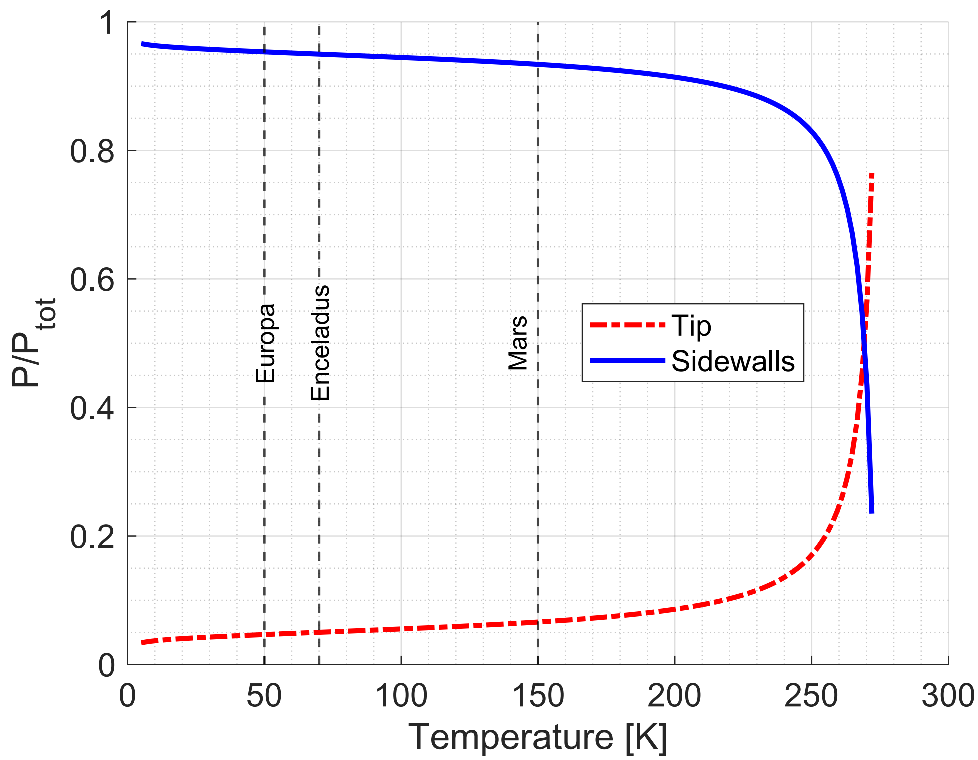

Figure 2.10: Relative importance of tip versus sidewall heating as ice temperature varies.

Figure 2.11 shows that with a fixed geometry, the plasma drill's normalized power savings have very little sensitivity to ambient conditions. Hence, plasma drilling provides the same order of advantages regardless of ice temperature and if proven to be effective could be considered for application on all ice deposits. This weak sensitivity to ambient conditions probably relates to the heat conduction equation's form, where heat flux is directly proportional to thermal conductivity.

In fact, if the physics of the problem are diffusion-dominated (which is the case for low descent velocities), the ratio between cracked and untracked heat fluxes depends almost entirely on the ratio between thermal conductivities. In other words, when external factors change, the whole temperature field is modified accordingly, but the fractional decrease in power consumption is given by the scaling effect of thermal conductivity changes, which are not sensitive to external conditions. For example, a probe's velocity increase is reflected as a greater heat flux in the cracked region, but the scaling factor $K*$ reduces by $\propto K*$ the heat-flux. These considerations can be made when the disturbing effect due to the presence of a "cracked region" boundary is neglectable ($R^* >> 2$). Descent velocity seems to influence the power gains. Specifically, at high descent velocities, cracking does little to change power consumption due to the domination of the convective term in the heat equation. Cracking in fact has the most effect on the heat diffused outward and so it becomes more and more effective as probe velocity descends and reaches a minimum at $0.5 m/h$.

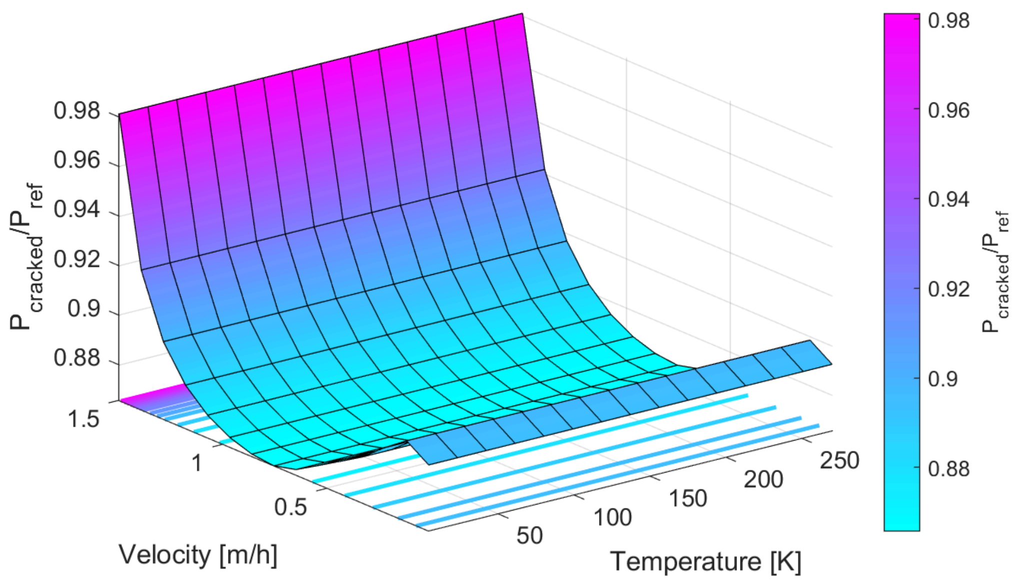

Figure 2.11: Effect of temperature and velocity variations on the cracking gains with standard parameters ($K^* = 0.75$, $R^* = 2$)

Descent velocity has an interesting effect on power consumption and the energy used to penetrate each meter of ice. This can be seen in figure 2.12 where it is evident that low velocities, power consumption is accordingly low; under these conditions, most of this power is diffused outwards without providing much of a benefit in terms of descent velocity. The limit example is a probe fixed in space ($v = 0$); under these conditions, the probe would be continuously drawing the power required to keep the necessary wall temperature gradients all the while not moving anywhere. Consequently, the energy to move any distance would be infinite.

On the other hand, as velocity increases, power consumption grows with a radical shape and energy per meter sharply decreases before reaching an asymptotic behaviour. As velocity increases, wall temperature gradients increase and less power is "wasted" in not producing descent velocity.

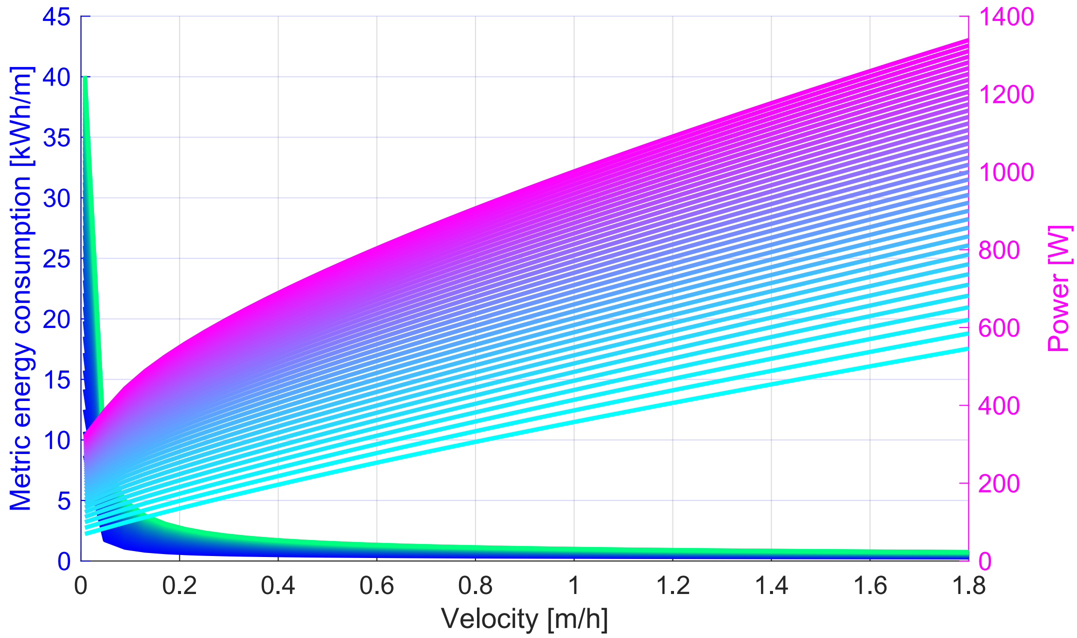

Figure 2.12: Effects of velocity on Power consumption and energy expended per meter of ice penetration. K^4* is also made vary and lies in the range 0.08 (light and dark blue), to 1 (magenta and green). Recall that $K^* = 1$ stands for un-cracked, reference conditions.

An investigation on probe aspect ratio was also conducted. The starting assumption is that the system's volume is constant and the only parameter that is allowed to change is Surface Area; additionally, as the geometry under investigation is a cylinder, Surface Area is changed by modifying Radius R and Length L. These two parameters can be combined to define aspect ratio as length divided by probe diameter $AR = L/D = L/2R$.
Surface area presents has a decreasing-increasing trend with a minimum for an aspect ratio slightly lower than 5. Power consumption follows a similar behaviour. If the probe were to be fixed in space, power consumption minimum point would coincide with the surface area's lowest value as this would minimize outwards heat flux. When descent rate is introduced in the system, the transport term tends to create a heat "wake" structure in which some of the heater's power is lost; this wake is very clearly seen in figure 2.15.

For this reason, the power consumption's minimum is pushed to progressively higher aspect ratios when velocity increases. The minimum position is determined by balancing conductive losses which increase with surface area and "transport" losses which decrease as the aspect ratio increases.

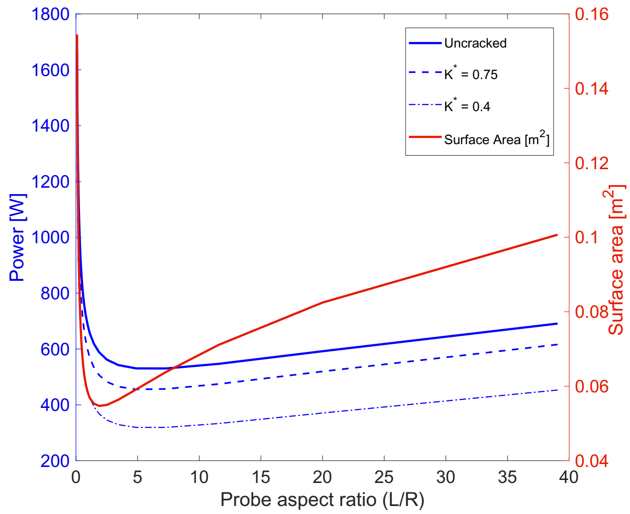

Figure 2.13: Effect of aspect ratio on power consumption.

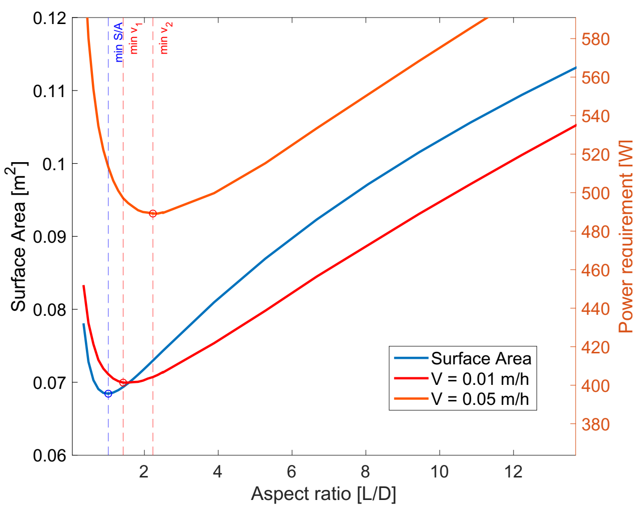

Figure 2.14: Effect of Aspect ratio [L/d] on Surface area and power consumption.

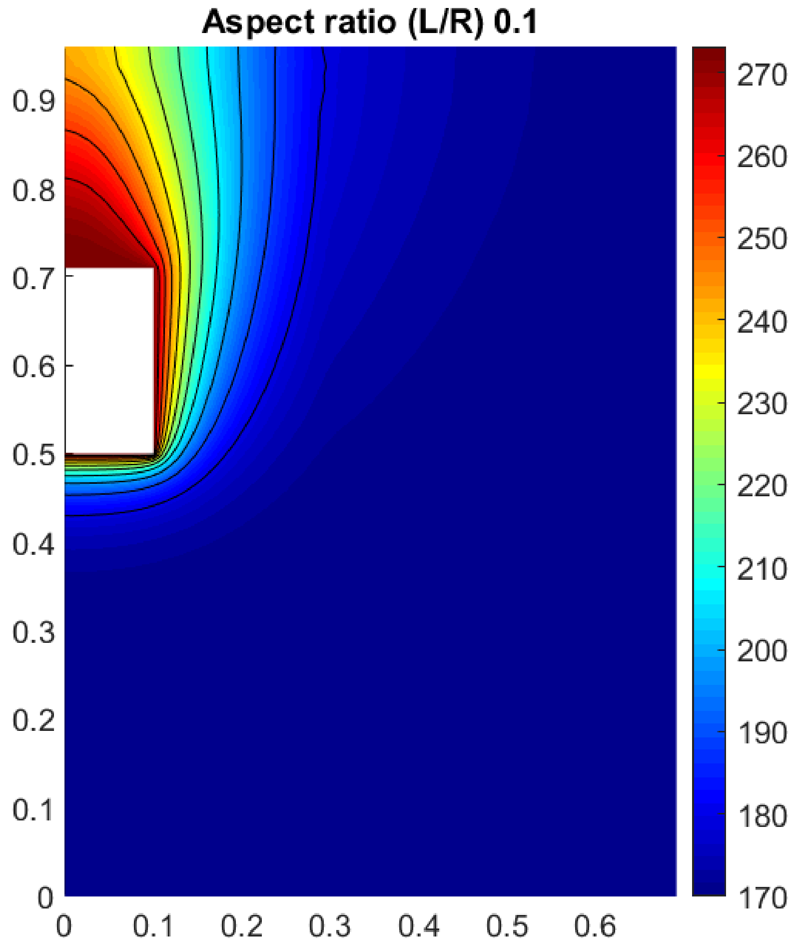

Figure 2.15: Low aspect ratio Temperature field

Figure 2.16 shows the sidewall power density profile and it can be noted that it has a similar shape as the theoretical one predicted by Aamot 67 [56]. The tail section ($y/L = 1$) has the minimum power requirement and the heat flux increases non-linearly while descending towards the tip. There are two main differences between this simulation's results and Aamot's theoretical predictions and they lie in close proximity to the edges. Towards the tip, there is a very steep rise in heat flux, while towards the tail the converse occurs. These effects can be visually identified in figure 2.15 by focusing on isothermal lines and noting how they are particularly dense towards the edges (similar to a thermal shock layer), while almost dispersing toward the end section (similar to an expansion wave).
Figure 2.17 depicts the power density profile on the tip. Note that latent heat of fusion

is neglected and therefore the "real" tip power profile is translated upwards by a constant term equal to $vh_f\rho_0$ where v is the probe's velocity, h_f is the latent fusion heat and ρ_0 is ice's density at $273.15K$. The conductive losses instead are minimum along the symmetry axis and steadily increase towards the edge. Where the sidewall and tip power profiles join up, there is a sharp decrease in heat flux.

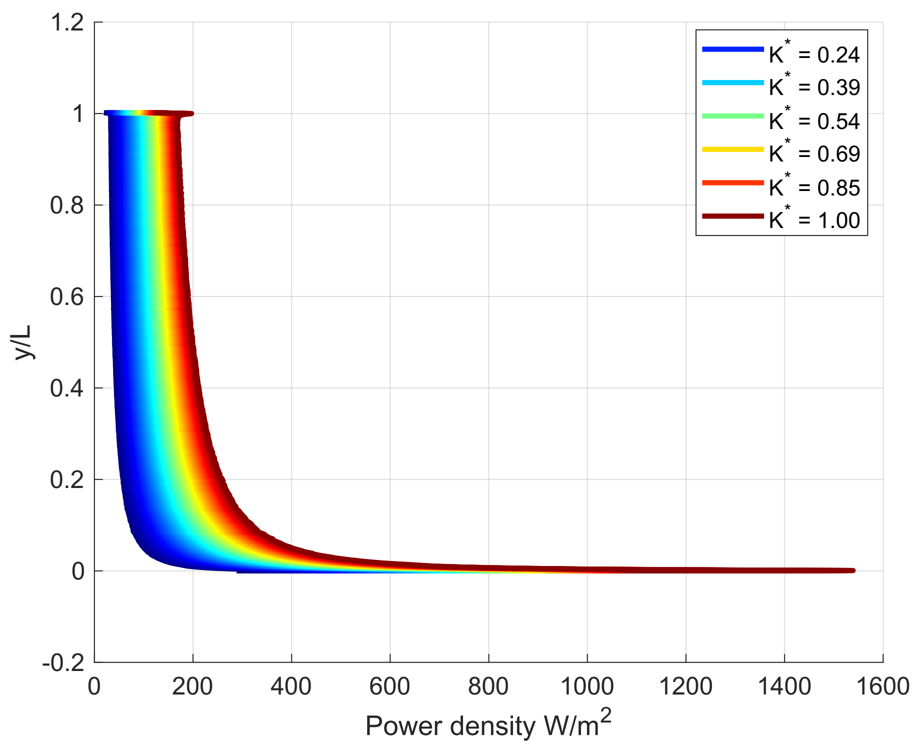

Figure 2.16: Power density profile along the probe sidewalls. $y = 0$ stands for the probe's tip and $y = L$ corresponds to the tail.

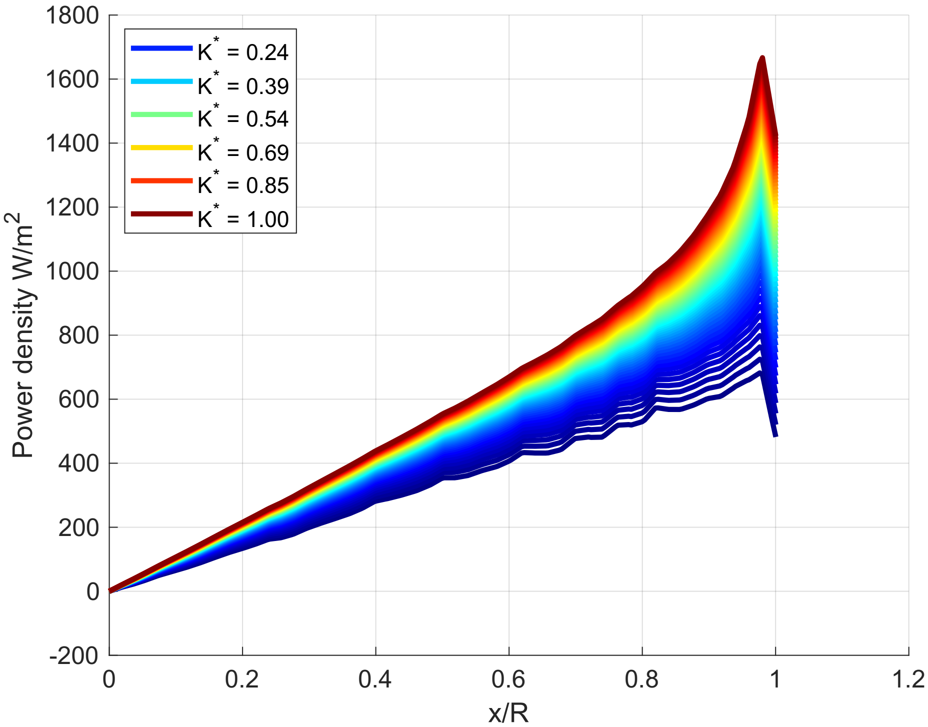

Figure 2.17: Power density profile along the probe's tip. $x/R = 0$ corresponds to the symmetry axis while $x = R$ is the probe's radius

The temperature gradients which drive heat transfer can be observed in figure 2.18. These gradients are closely related to the power profile, as the temperature gradient is the heat flux's slope.

When cracking is introduced ($K^* < 1$), the temperature gradients have a negative increase as it becomes progressively harder to transfer heat outwards. Even if temperature gradients increase, the overall heat flux is decreased as the decrease in thermal conductivity is larger than the increase in temperature gradients (heat flux is the product of the two). Hence as expected, the cracked ice layer behaves as an insulating layer.

2.4.1 Thermal probe sprinting

This subsection presents an observation that stems from the power-velocity curve and could lead to a decrease in average power requirements for a given ice penetration mission.

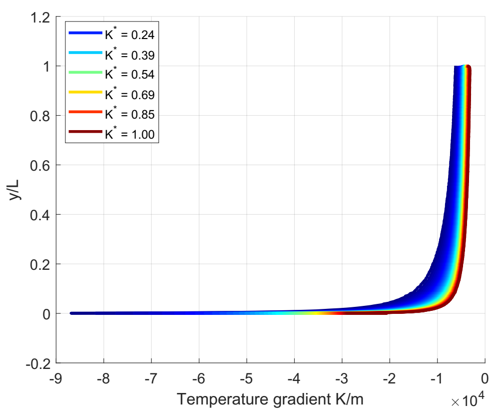

(a) Sidewalls

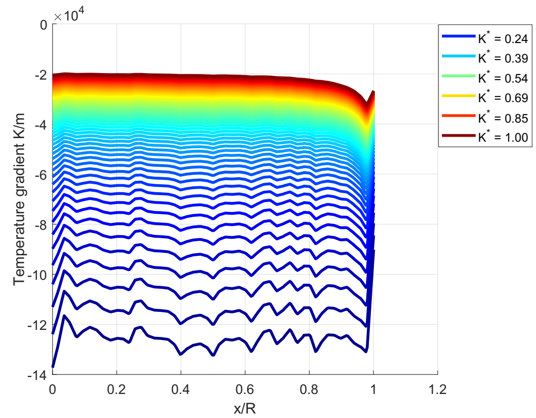

(b) Tip

Figure 2.18: Surface Temperature gradient profiles

Note first that power consumption requirements do not scale linearly with descent velocity, but tend to grow in a root-like fashion. The idea is to take advantage of this non-linearity by alternating periods of high power operation with periods of zero velocity during which the probe can be recharged.
The result of this method of operation could be to reduce the average power requirement at a fixed mission time, or to increase descent velocity at a fixed average power input.

The simplifying assumption is to neglect initiation and cooldown transients. In other words, as soon as electrical power is fed to the heaters, the probe begins to descend at its steady state velocity; and when the heaters are turned off, the probe immediately stops. In this way also the power necessary to "unfreeze" the probe is neglected together with any power savings that may occur when the heaters are turned off (probe keeps descending due to residual heat). This assumption is likely fair if cycle time and energy are large enough to make any transient losses negligible. A "high frequency", "pulsed" probe operation could be another research topic, but the assumptions made above would not be sound.
The easiest way to explain this phenomenon is by using an example derived from a small thermal probe (reference geometry) simulated under Mars polar conditions. We start by choosing arbitrarily a descent velocity of $0.4m/h$ which requires a continuous power of $850W$ to be maintained. If, on the other hand, the thermal probe were to have a means to store energy and spend one half of the mission time descending and the other half recharging, the average velocity would be the duty cycle times the peak descent velocity. Assuming that the mission time constraints remain unchanged, the peak velocity necessary to complete a mission with 50% duty cycle in the same time as a continuous-descent mission would be of $0.8m/h$ (twice the continuous velocity in fact). In order to generate this higher

descent speed, the power will have to draw $1100W$ of power. But, as the descent condition lasts only for 50% of the time, the continuous power requirement for this configuration will be given by the duty cycle times the peak power ($DC \cdot P = 0.5 \cdot 1100W = 550W$) which gives a significant power savings.
Note that at a systems level, the mission would spare 35% of the continuous power requirement by using a sprinting architecture. This would translate in significant mass savings in the power generation system (Solar panel area, RTG weight etc.), and conversely, the power storage system would become more critical. The volume of the batteries could well be excessive and outweigh any savings in the power generation system.

This descent concept is valid for all thermal probes and additionally, if proven effective, it could be applied to further increase a plasma drill's efficiency. This topic is not developed further but it is recommended for further research.

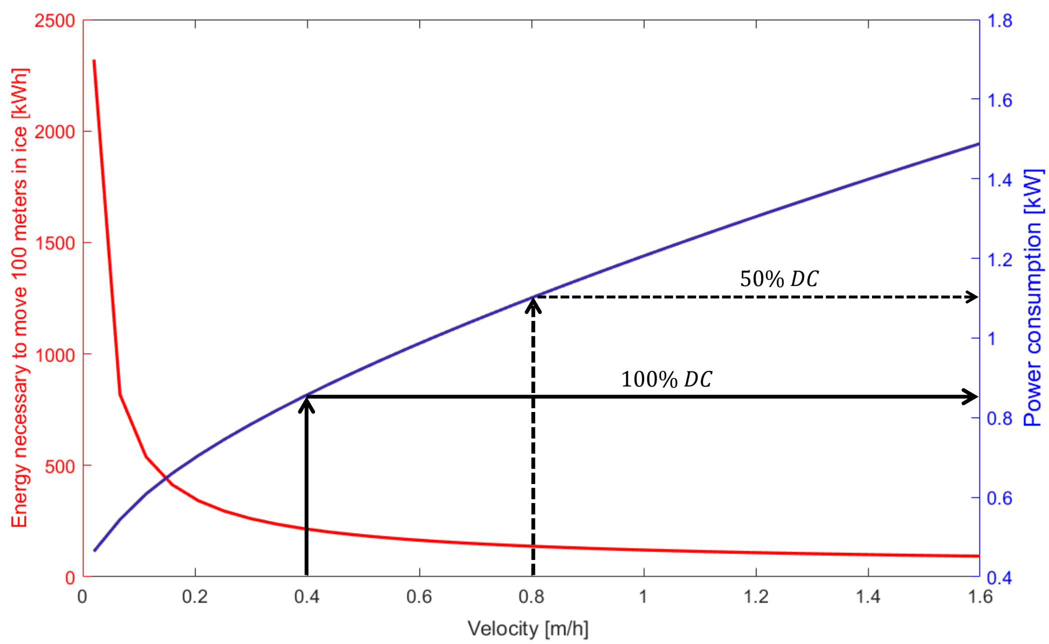

Figure 2.19: Power-Velocity lines at 2 different duty cycles with the same average descent rate

Chapter 3

High Voltage setup

3.1 General overview

The experimental setup's main function is to allow in-ice discharge experiments by managing the storage and release of electrical energy without the complexity that would come with constructing a field deployable plasma drill. This chapter will describe the setup and its changes over time.

There are a number of preliminary considerations that precede design. The starting point is the discharge phenomenon itself. In fact, the aim is to achieve ice breakdown and releasing an energy E in tens of microseconds. This information alone suggests a baseline to start designing from.
The central component of this system will necessarily be a pulse-capacitor which in substance is a standard capacitor, optimized for very rapid release of energy. This component stores a specific amount of energy given by the product of:

$$E = \frac{1}{2}CV^2$$

Where C is the capacitor's capacitance and V is the operating voltage. In theory, both quantities could be changed to achieve any energy, but some considerations fix the operating voltage: For maximum experimental flexibility, it is desirable to be able to achieve breakdown between electrodes separated by at least $1 - 2$ cm of ice. Breakdown distance is a function of voltage [65] [66]; therefore, it is clear that the highest possible operating Voltage should be sought out. Experimentation with different in-ice gaps is possible only by lowering the maximum voltage, while increasing levels above the limit requires system-level redesigns and component acquisitions.

An operating voltage of 40 kV was adopted following two additional considerations:

- High Voltage COTS components such as cabling, power supply, capacitor, voltage probes *etc.* become very expensive above 40 kV
- Corona discharges - which are the phenomenon by which the a high potential surface transfers charge to an otherwise insulating fluid by means of ionization [67] - become fairly likely above 40 kV, unless mitigated with design choices aimed at limiting electric field intensification points (sharp edges). As observed during the test campaign, already at 30-35 kV electrical connectors with sharp features (crocodiles) can reliably cause corona discharges.

Having constrained the operating voltage, capacitance is maximised while keeping cost and component availability under control.
In conclusion, the pulse capacitor enables the storage of $80J$ with an operating voltage of $40kV$ and a capacitance of $0.1\mu F$.

Given the means to store energy at a high voltage, another necessary component is a Power Processing Unit which converts one form of electrical energy ($115V\ AC$ coming from the power grid) to another usable by the capacitor ($40kV\ DC$).
Finally, there must be a switch that keeps the capacitor disconnected from the experiment during the charging phase. This is necessary to avoid a continual electrical leak between electrodes through thin water layers or the ice itself from interrupting the charging phase and converting what should be a highly non-equilibrium process into stationary resistive heating.

Another important design driver is related to electrical safety.
The High Voltage power supply alone does not constitute a substantial safety hazard, as the maximum current output of most high voltage power supplies is very low (a few milliamps). Thus, the result of accidentally coming in contact with the HV output would be a painful, non-lethal discharge (similar to an incapacitating electrical weapon).
As soon as the 0.1 μF capacitor is connected to the system, the consequences of accidental contact become much more serious. In fact, the capacitor itself can sustain a very large current when discharging, and if human body were to be the discharge's path to ground, the resulting current pulse would be enough to cause significant harm.

The capacitor circuit clearly poses a safety hazard and the resulting risk requires a degree of control before being deemed acceptable. Due to the very high consequences of any accident, the mitigation strategy which is adopted in the experimental setup is the most drastic and effective one (image 3.1) - physically eliminating the risk of accidental human contact by constructing an enclosure. Furthermore, any access to the system is preceded by a readout of a multimeter connected to the capacitor via a high-voltage probe in order to verify the absence of energy in the system.

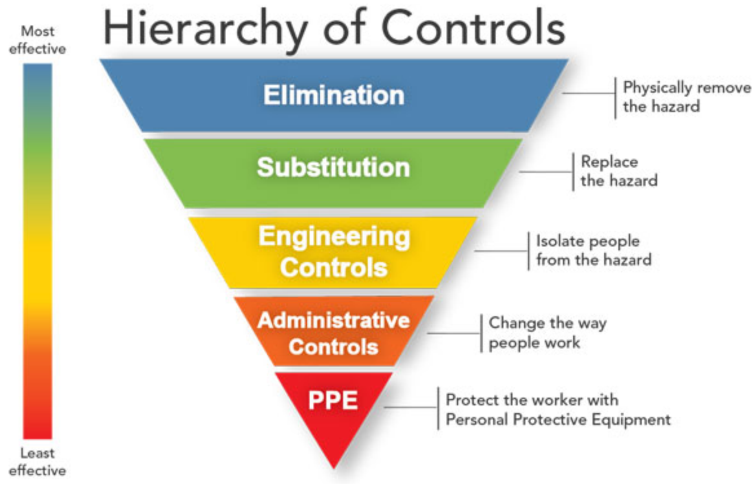

Figure 3.1: Hierarchy of hazard control strategies

3.2 Servo setup

In the previous section, the commonalities between all the architectures of the experimental setup are described. The differences lay in the method by which the pulse capacitor is connected to the experiment, control and telemetry strategies and ultimately, the grounding scheme.

The first design approach to the system's realization aims at giving the maximum control over discharge voltage and timing by employing two servo-actuated High-Voltage switches, each with three possible positions. The transition between various system states is actuated by these two switches.
As can be seen in figure 3.2, the two servo-mechanisms control respectively position of the power supply's output and the capacitor's positive terminal.
The "High Voltage" arm can be connected to the capacitor for charging purposes; in addition, as the power supply can be easily damaged if directly connected to the discharge RLC circuit during the current pulse, the second arm position can fully isolate the power supply's output from all electrical connections. The last High-Voltage switch position connects the power supply directly to the experiment in order to drive a high-voltage resistive heat dissipation (using the ice as a resistor).
Similarly, the arm connected to the capacitor's positive terminal, can move to a grounded path, to the ice sample or to a fully isolated position.

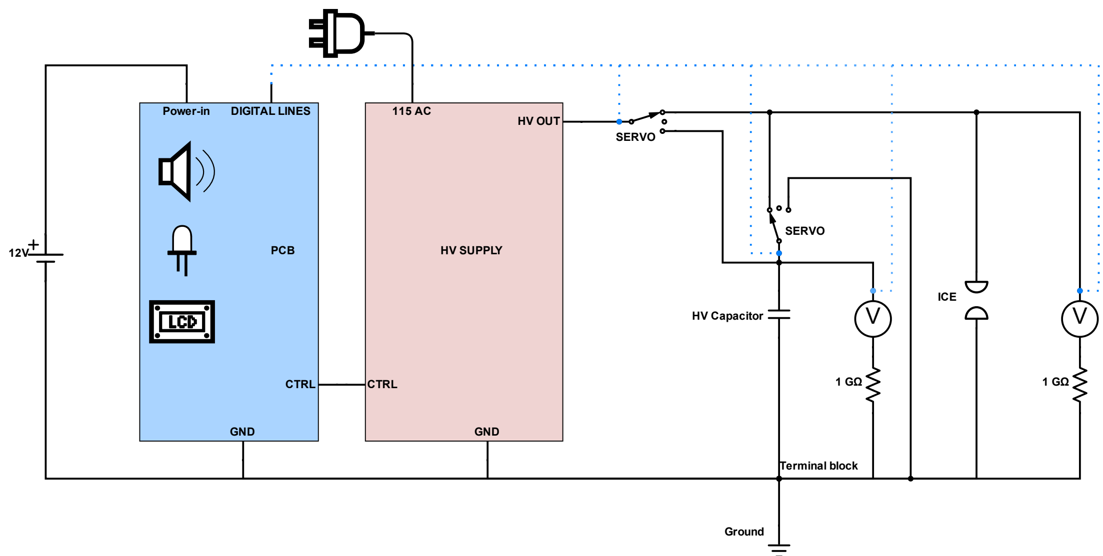

Figure 3.2: Electrical schematic of the servo setup. The blue dashed lines signify that there is low-voltage cabling connected to a component (not the circuit itself). For instance, the servo motors move around high voltage cables while needing to be powered by a 5V, connected to ground and receive a logical PWM signal.

Two High-Voltage probes transform the capacitor's and experiment's voltage levels into something that can be read by a multimeter without frying. Each probe essentially divides the real voltage by a factor of 1000. This division is obtained by using two resistors, one of which is grounded and values $1G\Omega$. This detail is important as it introduces an additional layer of safety to the system. In case of a servo failure when the capacitor is fully charged, the system will act as a RC circuit, discharging following an exponential decay in a little more than 10 minutes instead of being potentially lethal for hours.

$$I = \frac{dq}{dt}; \quad V = \frac{I}{R}; \quad q = CV; \rightarrow V = -CR\frac{dV}{dt} \rightarrow V = V_0 e^{-\frac{t}{RC}}$$

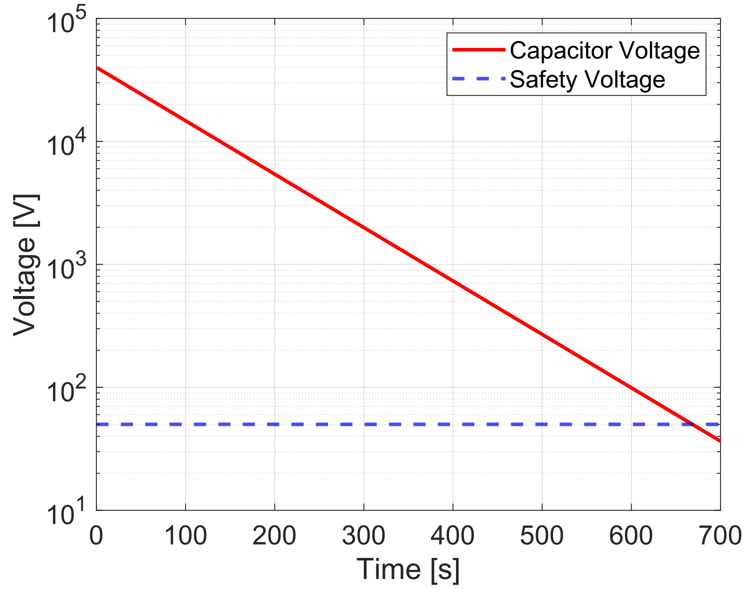

Figure 3.3: RC circuit discharge (R = $1G\Omega$; C = $0.1\mu F$; $V_0 = 40kV$). Time to reach a "safe" voltage of $50V$ is 669 seconds.

Before proceeding with further details on the construction and control of the system, it can be useful to summarize the concept of operations via a finite state diagram (figure 3.4). This diagram shows the different operating states that the system can find itself in.

After power-up, the system transitions immediately to a "safe" state by grounding the capacitor, disconnecting the power supply from all loads and disabling the power supply's output. This state can also be manually triggered at any moment. In order to discharge in-ice, the capacitor must first be charged in a "charging" state which is reached by placing the capacitor switch in an isolated position and connecting the power supply to the capacitor's positive terminal.
Once the system is charged, it waits for a command to initiate a discharge and when it is received, the power supply is isolated and the capacitor is connected to the experiment; after this, the system can be charged again. The "bypass" consists in connecting the power supply directly to the experiment, all the while grounding the capacitor to avoid unintentional charging. A faulted state can be triggered at any moment if the Emergency

STOP button is toggled or some internal logic is violated. This last step was not fully implemented, but the idea was to have an autonomous safeguard against anomalies with a set of logic statements such as "trigger faulted state if capacitor voltage is decreasing when in charge mode". This safety aspect is not necessary for a bench-top system, but might become object of study when a field-deployable prototype is constructed.

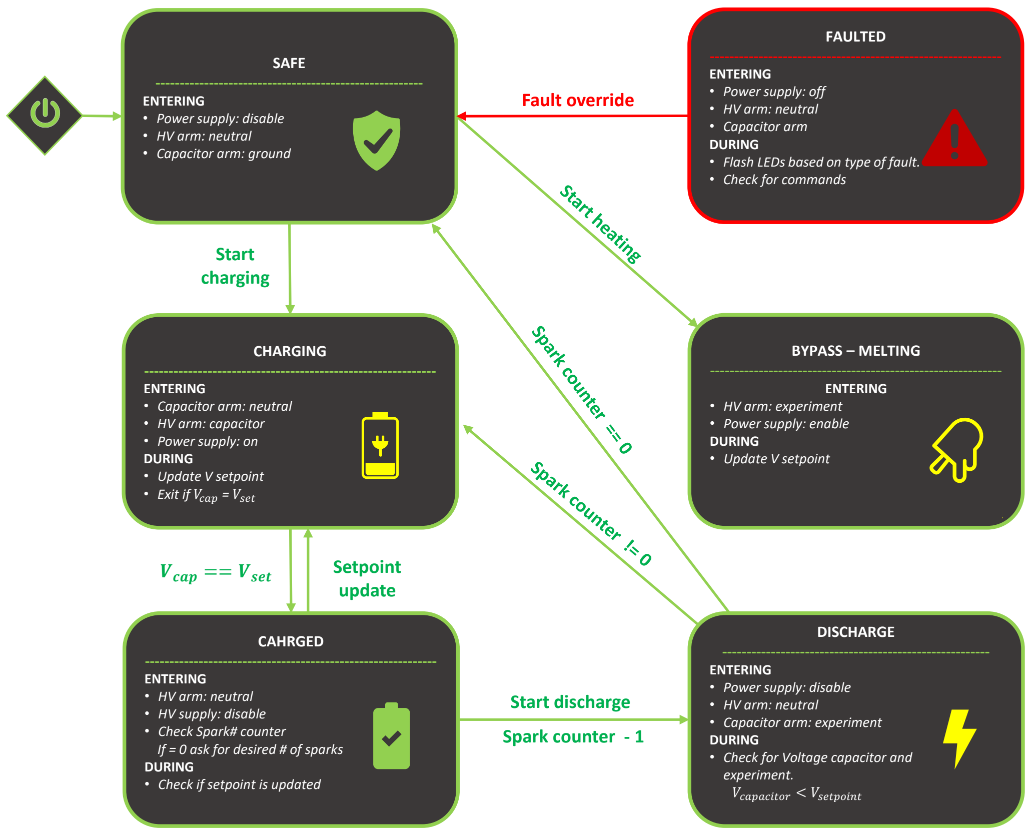

Figure 3.4: Finite state diagram of the servo setup. To avoid encumbering the diagram, all the lines pointing to the faulted state are omitted.

Figure 3.5 shows a block diagram of the real system. All controls and telemetry gathering are routed via an Arduino microcontroller which is installed on a PCB containing the circuitry necessary to drive sensors, power low-voltage electronics *etc.* The microcontroller uses serial communication to talk with a PC on which controls state switching and telemetry displaying / logging via a custom Graphic User Interface. As can be seen in figure 3.2, the PCB is directly connected to the High-Voltage power supply via low voltage logical lines. A radio link between two XBee modules is used to avoid the risk of frying the control laptop and maybe harming its user as a consequence of high voltage potentially leaking from the power supply to the PCB, or excessive noise being picked up in the cabling. In this way control and system are physically separated and any unforeseen transient voltages would have no way of reaching the human operator.

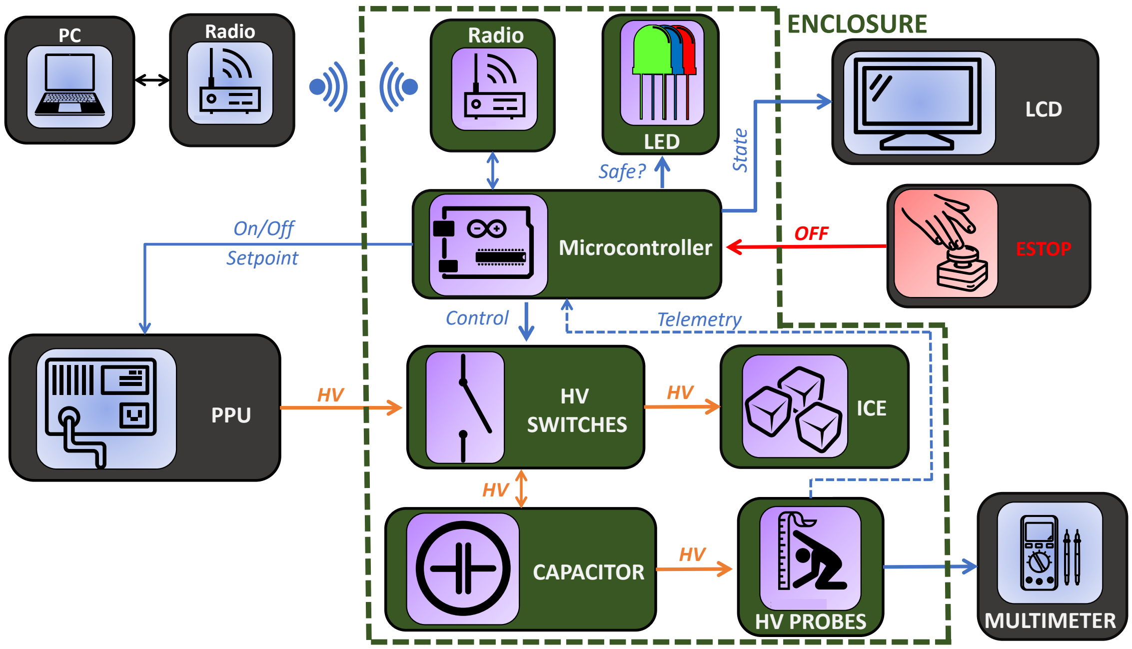

Figure 3.5: Servo driven setup block diagram

An additional layer of safety is provided by RGB LEDs which are colour-coded to display the different states of the system; this serves the purpose of having an easily identifiable visual reference signalling the presence of charge in the system. A latching ESTOP button quickly turns the power supply output off and triggers a faulted state which must be addressed by unlatching the button before any control can be sent through the software.

Furthermore, the absence of charge can be determined in two different ways. Firstly, the capacitor Voltage is read by the microcontroller and subsequently displayed in the GUI. The High Voltage probe's output is also directed to a multimeter, positioned inside of the enclosure and always left into DC Voltage reading mode.

The system's state can also be read on an LCD screen. The High-Voltage probe connected to the ice, which can be seen in figure 3.2, was almost immediately removed from the setup as its temporal resolution is not sufficient to read any useful data. In fact, the experiment's Voltage level is zero except for the 30 μs during which the discharge is occurring. A high temporal resolution probe would enable to compute the total discharge energy efficiency of the switch. High resolution voltage probes were not used due to the excessive cost and relatively small benefit.

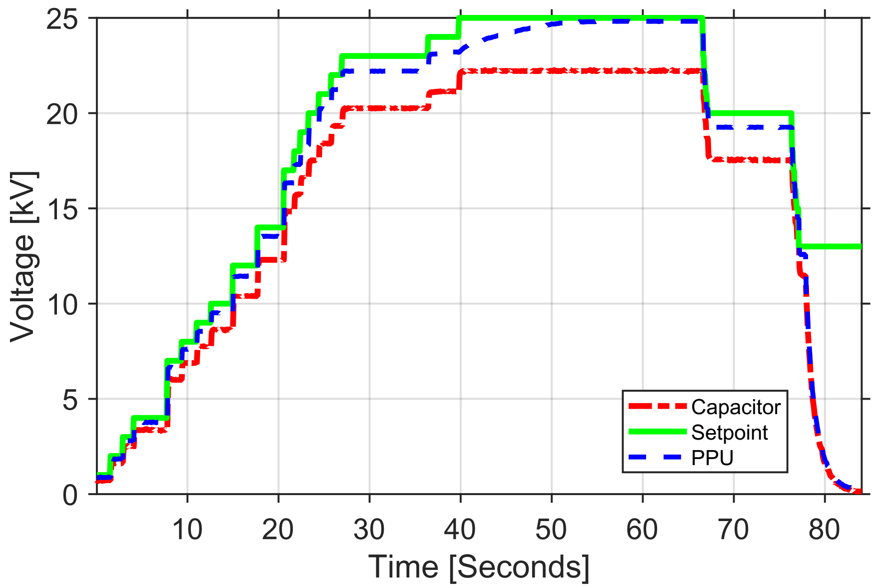

Figure 3.6: Telemetry from the servo setup. This chart shows a gradual increase of the voltage set-point up to 25kV and at 76 seconds the state is transitioned to the safe state which grounds the capacitor

Mechanically, the whole system can be observed in figure 3.9. The two High Voltage switches are custom and made out of a servo motor to which an arm and two fixed terminals are connected. The assembly is mounted on an Aluminium pylon which is shrouded in insulating plastic. The three switch positions are at 0, 90 and 180 degrees going upwards from the lower terminal.

The custom high voltage switches present several advantages over a COTS solution. Firstly, the custom solution has finer control over discharge voltage and timing with respect to a commercial spark gap. Additionally, the system's cost is contained by the use of hobby grade servo mechanisms and 3D printed components. If both the switches were 40kV-rated COTS, the cost and lead times would have likely been order of magnitudes greater.

Protection from unintentional discharges is provided by ensuring that every in-air gaps between high potential and grounded conductors is above 6 cm - this value is derived by using a conservative breakdown voltage of air at atmospheric pressure 1 kV/mm and multiplying the gap by a 1.5 precautionary factor.

Furthermore, insulating materials, such as 3D printed PLA and laser-cut clear acrylic, are used in most of the structure. A Material thickness of at least .25 inches is used all around to ensure that no arcing may occur through the insulating materials [68]. Nylon screws are also used to avoid creating an unintentional grounding path. The switch's terminals are made out of capped nuts which are characterized by a radius of curvature that creates an electric field intensification sufficient to ensure that the discharge occurs along a predicable path, while still avoiding corona discharges. A spring based shock absorber is used in the arm-mounted terminal to avoid mechanical damage when caps collide - this feature is entirely precautionary as the most of the arm's rotational kinetic energy is dampened by elastic deformation in the arm itself.

The two High Voltage probes (figure 3.8)are placed on 3D printed stands that ensure sufficient separation from the floor. Analogously, the capacitor is kept in a vertical position by an extruded Aluminium frame.

The outer enclosure is a large parallelepiped made out of an 8020 Aluminium frame and clear-acrylic panels that allow observations of the system's state and visual inspection of the experiment without having to open the enclosure. The conductive framing is grounded and the acrylic panel's thickness (1/4 inch) is sufficient to avoid arcing outside. Quick access to the system is enabled by two acrylic panels which are mounted on hinges and are kept upright by two latches. The enclosure's dimensions ($45x24x20$ inches) are chosen to allow ample clearance between components and to easily accommodate future setup modifications such as additional capacitors. The system's dimensions are also small enough that they remain compatible with a bench-top setting. A temporary testing compartment was obtained from the surplus space in the enclosure's interior; an acrylic panel serves as a separator which confines shrapnel in the testing chamber thus protecting the rest of the system.
Protection from unintended shifting around or tipping over of internal components is ensured by an acrylic pavement in which a threaded hole pattern has been laser-cut and manually threaded. The power processing unit is mounted on top of the enclosure; a single High-Voltage wire starts form the power supply and enters the enclosure through a circular hole in one of the top-mounted acrylic panels. As the wire is rated to withstand 40 kV, this does not constitute a safety hazard. The microcontroller and PCB are both mounted on M3 standoffs in a corner of the enclosure.

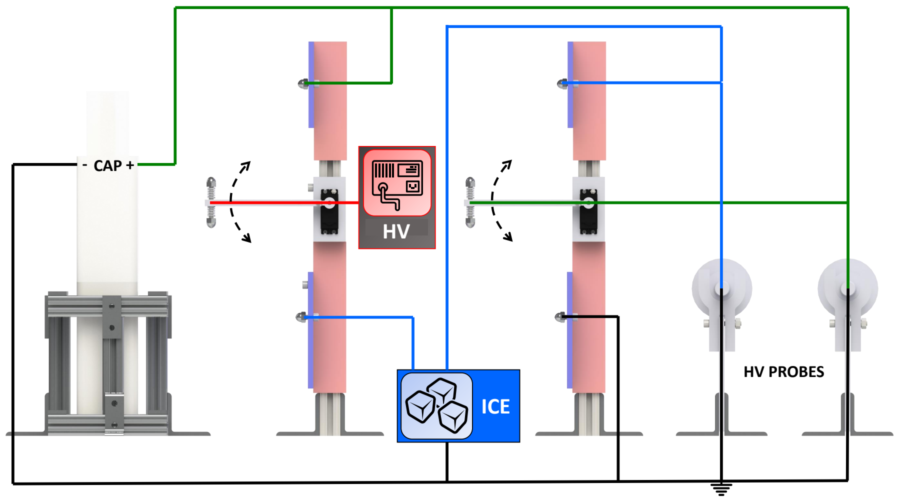

Figure 3.7: Hybrid block diagram

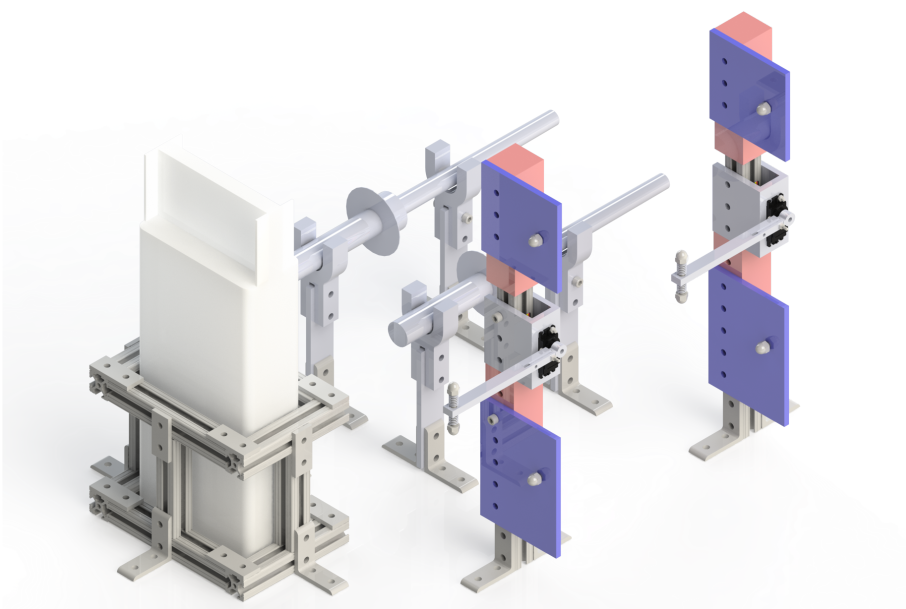

Figure 3.8: Render of components inside of the enclosure

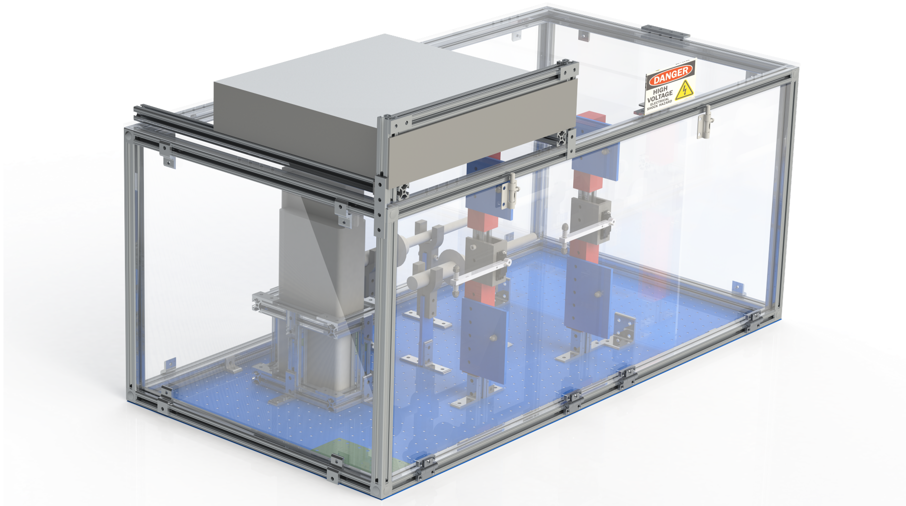

Figure 3.9: Render of the servo setup with enclosure

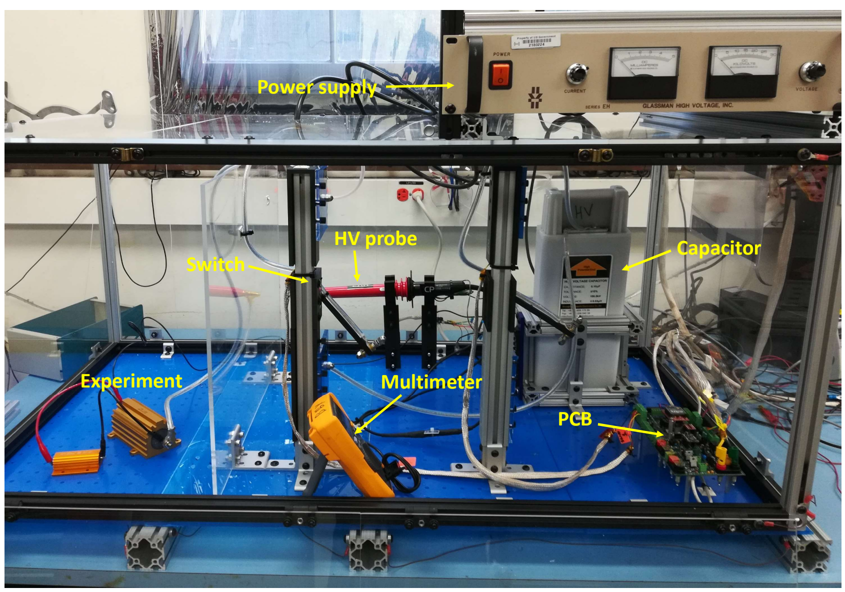

Figure 3.10: Picture of the servo setup with internal components.

3.3 Anomaly and noise reduction efforts

The Servo actuated system suffered an anomaly at a discharge voltage of $20\ kV$ which resulted in transient over-voltages that fried most of the low-voltage electronics on the PCB and a $10V$ reference integrated circuit on the power supply.
This type of anomaly can not be attributed to high voltage unexpectedly leaking to unwanted sections of the circuit, as the probable causes all relate to the current pulse's aggressiveness.
There are two possible mechanisms that might be responsible for the anomaly.

Firstly, it is likely that the grounding scheme observable in figure 3.2 is sensitive to "ground loops". This phenomenon occurs when voltage differences between ground and parts of the circuit are induced by current flowing in the grounding cabling.
The initial version of the servo setup might be subject to two different types of ground loops. In fact, there are both different paths to ground and multiple circuits grounded via a common impedance. Multiple paths to ground arise from the presence of a neutral cable in the power chords of both high voltage and PCB power supplies; transient voltage might be induced in these lines when the current is flowing to the copper bar via the terminal block.

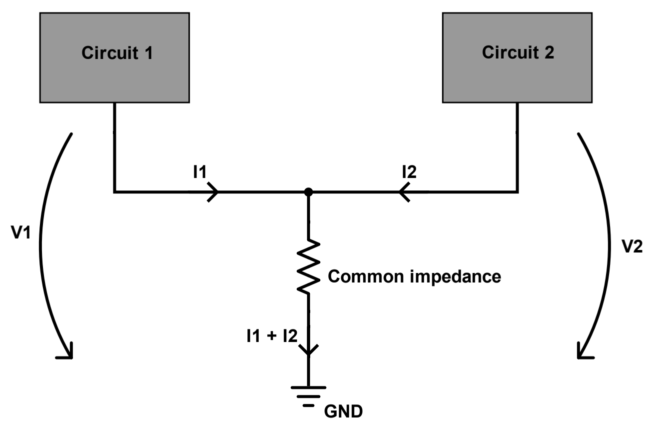

Figure 3.11: Common grounding impedance noise coupling (adapted from [69])

On the other hand, conductively coupled noise through a common impedance is the phenomenon that occurs when two or more circuits share a common ground, which causes the voltage of each circuit to have mutual influence [69]. A similar situation is clearly observable in figure 3.2, where the high voltage, PCB and Capacitor grounds are all connected to a single terminal block from which a single cable goes to the copper bar. Both of these noise sources can be tackled by modifying the grounding scheme.

The second source of noise and also the hardest to protect from is EMI (electromagnetic interference).
The discharge phenomenon, characterized by a current pulse which reaches peak values in excess of 5000 Amperes (Figure 3.12), creates a very aggressive electromagnetic environment for conductive materials. Current transients induce time-varying magnetic fields which in turn generate a varying electric field. This coupling between current ($\boldsymbol{J}$), Magnetic ($\boldsymbol{B}$) and electric fields ($\boldsymbol{E}$) is described in the final two Maxwell's equations (respectively known as Faraday's 3.1 and Ampere's 3.2 laws).

$$\nabla \times \boldsymbol{E} = -\frac{\partial \boldsymbol{B}}{\partial t} \tag{3.1}$$

$$\nabla \times \boldsymbol{B} = \frac{\boldsymbol{J}}{\epsilon_0 c^2} + \frac{1}{c^2}\frac{\partial \boldsymbol{E}}{\partial t} \tag{3.2}$$

Where c is the speed of light and ϵ_0 is the permittivity of free space.
The large discharge current transient therefore generates a correspondingly large electromagnetic pulse which propagates in space and is felt around the system as a rapid variation in the flux of magnetic field which in turn is transformed into electromotive force in the cabling. Therefore, the voltage in these cables suffers rapid changes during the discharge phenomenon. This aspect can be easily seen by rewriting Faraday's law of induction 3.1 and applying Stokes theorem.

$$\oint \mathbf{E} \cdot d\mathbf{r} = -\frac{d}{dt} \int_S \mathbf{B} \cdot d\mathbf{S} \tag{3.3}$$

This equation implies that a variation of the magnetic flux across a circuit is followed by an induced electromotive force (or electric field's closed path integral).

The discharge's circuit capability of generating electromagnetic fields is exemplified in the current waveform (figure 3.12).
At $t = 0\ \mu s$ - when the oscilloscope is triggered - there is a small current pulse probably relating to the plasma channel's formation in the ice. When this channel has fully developed 30 μs later, the main discharge can occur and charge starts flowing from the capacitor's positive terminal, through the ice and towards ground. While this is happening, the current flowing in the circuit stores energy in magnetic fields and opposing current changes in the system. This in turn causes more charge to flow from the capacitor's positive terminal than would be necessary to neutralize the voltage difference between positive and ground

sides of the capacitors. Hence, the capacitor starts charging with a negative voltage and the current rapidly decreases and reaches a negative peak value. This oscillating pattern occurs repeatedly and the current peaks are progressively dampened due to system's resistance.

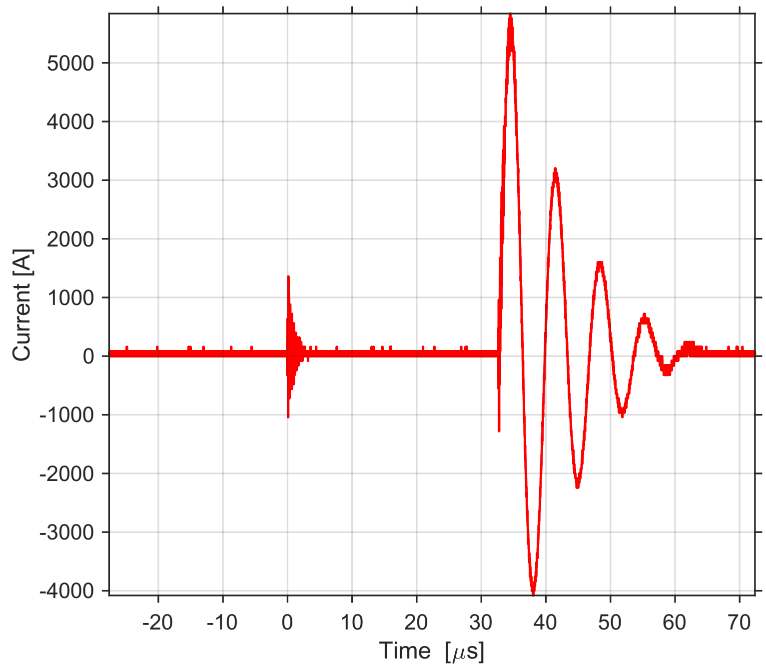

Figure 3.12: Discharge waveform

The initial mitigation step consisted in isolating the low-voltage ground from the high voltage "discharge circuit". The two grounds were separated by a resistor to avoid ground loops via a common impedance. In addition, all cables are shielded with a grounded conductive material and the PCB is placed in a simple metal enclosure to reduce electromagnetic interference.
Reference signal monitoring with a high bandwidth oscilloscope showed that these mitigation strategies are not sufficient to allow for safe system operation of the servo setup at nominal discharge voltage. Consequently, in order to avoid a lengthy noise-reduction investigation, the problem was tackled from another angle. The main suspect was that the majority of the noise generated by the discharge was being picked up by low voltage cabling and following these lines to the PCB and Power supply. Therefore, a system-level

simplification effort was conducted based on the following considerations:

- Minimize system inductance by keeping cable length to a minimum, increasing cable cross sectional area and eliminating wire spires that may act as antennas.
- Keep low voltage ground separated form discharge.

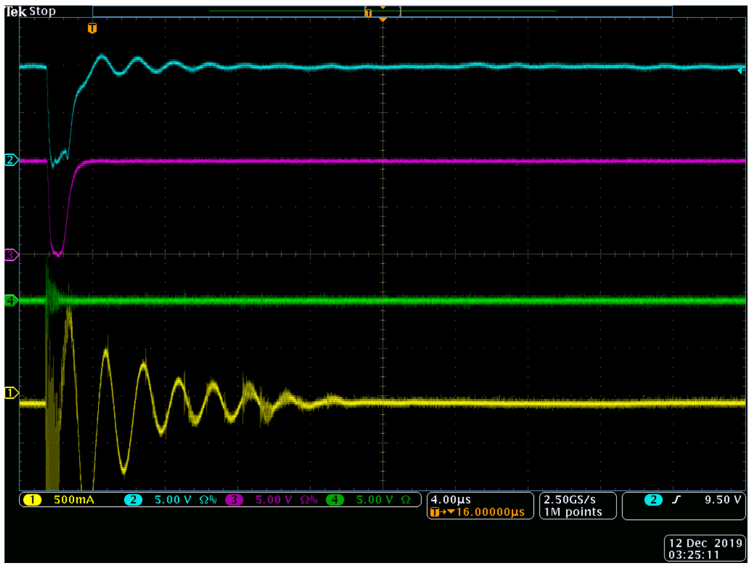

Figure 3.13: Signals being disrupted as a consequence of the discharge. (4) and (5) are ground signals and can be seen ringing, while (1) and (2) are reference signals in the microcontroller and power supply and can be seen reaching $0V$

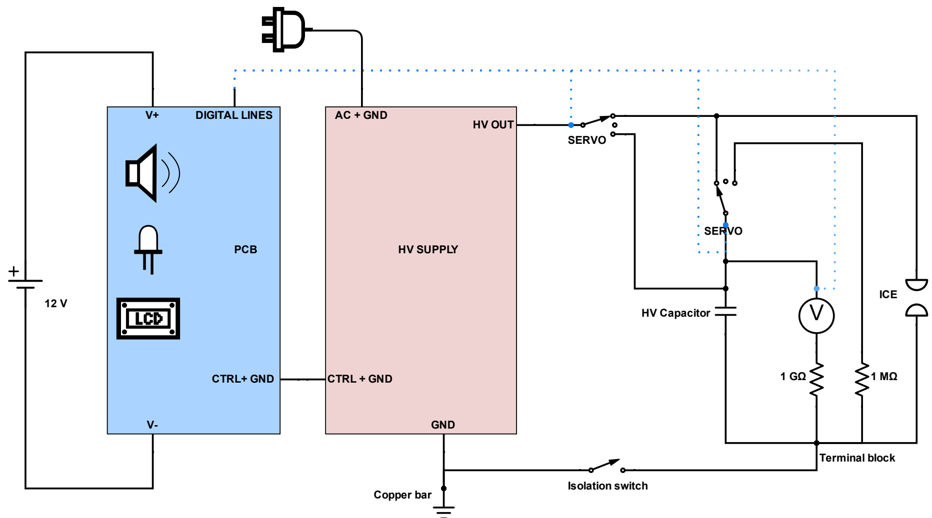

Figure 3.14: Discharge isolation attempt

3.4 Fixed Spark-Gap, GUI controlled setup

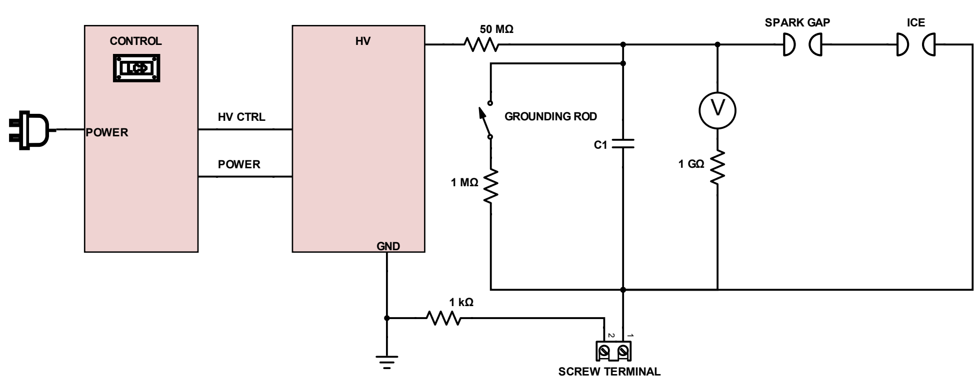

Figure 3.15: Smart spark-gap circuit

Considering that isolation and shielding efforts were not sufficient at mitigating discharge-noise and protecting low voltage electronics inside of the PPU and controller from frying, the system was significantly modified with the aim of reducing circuit inductance.

There are several ways to reduce inductance in a system. The first two are suggested when observing the expression for self inductance in a linear conductor derived by Rosa in 1908 [70].

$$L = 2l[log\frac{2l}{R} - 1]; \quad [H] \tag{3.4}$$

Where:

- L signifies inductance
- l is the conductor's length
- R is the conductor's radius.

In practical terms, this expression suggests using thick - short wires in high current areas. Therefore, the capacitor's grounding wire was decreased in gauge and the discharge path was shortened as much as possible.
Furthermore, a consideration regarding circuit geometry can be made by combining Ampere's law with the definition of Inductance for a circuit with Cross sectional area A and depth d, through which a current J is flowing:

$$L = \frac{\Phi_m}{J} = \frac{\int B \cdot \boldsymbol{n} ds}{J} = \frac{BA}{J}$$

$$\oint Bdl = \mu J \rightarrow Bd = \mu J$$

Considering unit circuit depth:

$$L = \frac{\mu A}{d} = \mu A$$

Where μ is the electrical permeability of the medium.
The main observation deriving from this relation is that circuit cross sectional area is directly responsible for inductance; therefore, in order to minimize cross sectional area, all cables are twisted and zip-tied together wherever possible - especially positive and ground discharge cables.
The proper use of shielding and inductance reduction could solve the noise issue if executed perfectly. Nevertheless, in an imperfect system, the more wires are present, the higher the likelihood that one specific mitigation strategy might be inefficient or poorly executed. In these circumstances, troubleshooting can easily become a nightmare thus taking a lot of time and decreasing system flexibility.

This is why, it proved beneficial to enact a number of complexity-shedding measures which consisted primarily in modifying the circuit to reduce the number of low-voltage cables.

As can be seen in figure 3.2, a large number of cables go from the PCB out to the servo switches and the high voltage probes. Firstly, the high-voltage bypass channel envisioned to perform resistive heating with the PPU is taken away by eliminating the High-Voltage servo switch. Current pulse protection, which was provided to the power processing unit by placing the servo arm in an isolated position, is now granted by the use of a ballast resistor with resistance of $50M\Omega$ placed just after the High Voltage output. This resistor modulates the maximum current that can flow out of the power supply, but also provides discharge protection.

The servo actuated switch which governs the capacitor's positive output is also eliminated in favour of a spark-gap. Capacitor grounding is now achieved with a manually actuated plastic rod. One end of the rod is hand-held and the other end has a ring terminal which connects to ground via a small ballast resistor used to decrease the grounding-discharge's current peak (and therefore also emitted sound and light levels). In order permanently ground the capacitor when performing maintenance on the system, a threaded rod is partially screwed into the capacitor's positive terminal leaving a quick way to latch the grounding rod in position.

Additionally, the digital lines going from the capacitor's HV probe are eliminated and all voltage read-outs are performed by the multimeter directly connected to the probe. This means that voltage telemetry is reduced to set-point and supply output level. The grounding scheme is slightly altered from the "discharge isolated" system (figure 3.14). In fact, the controller is grounded via the power cable and one of the control lines places the controller's and supply's grounds in communication. The capacitor's ground is connected to the HV power supply via a $1k\Omega$ which acts like a small ballast resistor and protects the power supply.

The spark-gap is custom built and provides some control over discharge voltage at a very low cost. As can be seen in figure 3.16, the bottom nut is fixed and connected to the Capacitor, while the top nut resides on a threaded rod which can translate in one dimension when turned and remains fixed in position due to friction when left alone. Decreasing or increasing the spark gap length modifies breakdown voltage accordingly. The main drawback that comes with a semi-fixed spark-gap is the difficulty in predicting breakdown voltages due to atmospheric variations in pressure and humidity (The test-bed room is not climate controlled).

Another EMI reduction step consisted enclosing both power supply and control electronics in two metal boxes (figure 3.18); this step serves the purpose of blocking the strong

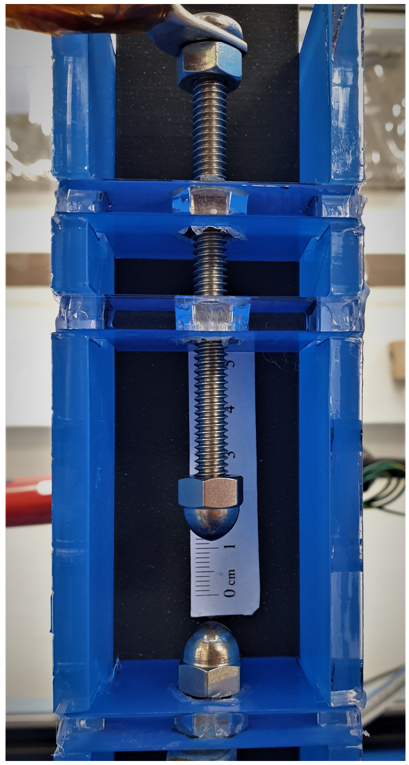

Figure 3.16: Custom spark-gap. The lower nut is connected to the positive terminal of the capacitor, so that an any spark-gap modification does not require the user to interact with the potentially hazardous part of the system.

electric field that is generated by the discharge event. These two enclosures are then mounted outside of the setup thus also increasing their physical distance from the discharge event (electromagnetic waves decay as $1/r^2$). BNC and shielded DSUB cables are used to reduce noise intrusion into the enclosures.
Fitting everything in two metal boxes also required the lab-grade power processing unit to be substituted with a substantially smaller unit.

This setup has a few important downsides when compared to the servo actuated setup. Firstly, it requires a closer contact between operator and system by forcing manual intervention every time a discharge voltage change is desired and to ground the capacitor. This makes the system slightly less safe with respect to the servo-actuated setup. The hazard posed by accessing the enclosure is controlled by having a clear procedure that obliges the user to ground the capacitor as soon as the acrylic panel is opened. Additionally, a high voltage probe is still connected to the capacitor and can steadily draw current in the event of an anomaly which impedes manual grounding (such as mechanical damage to the rod).

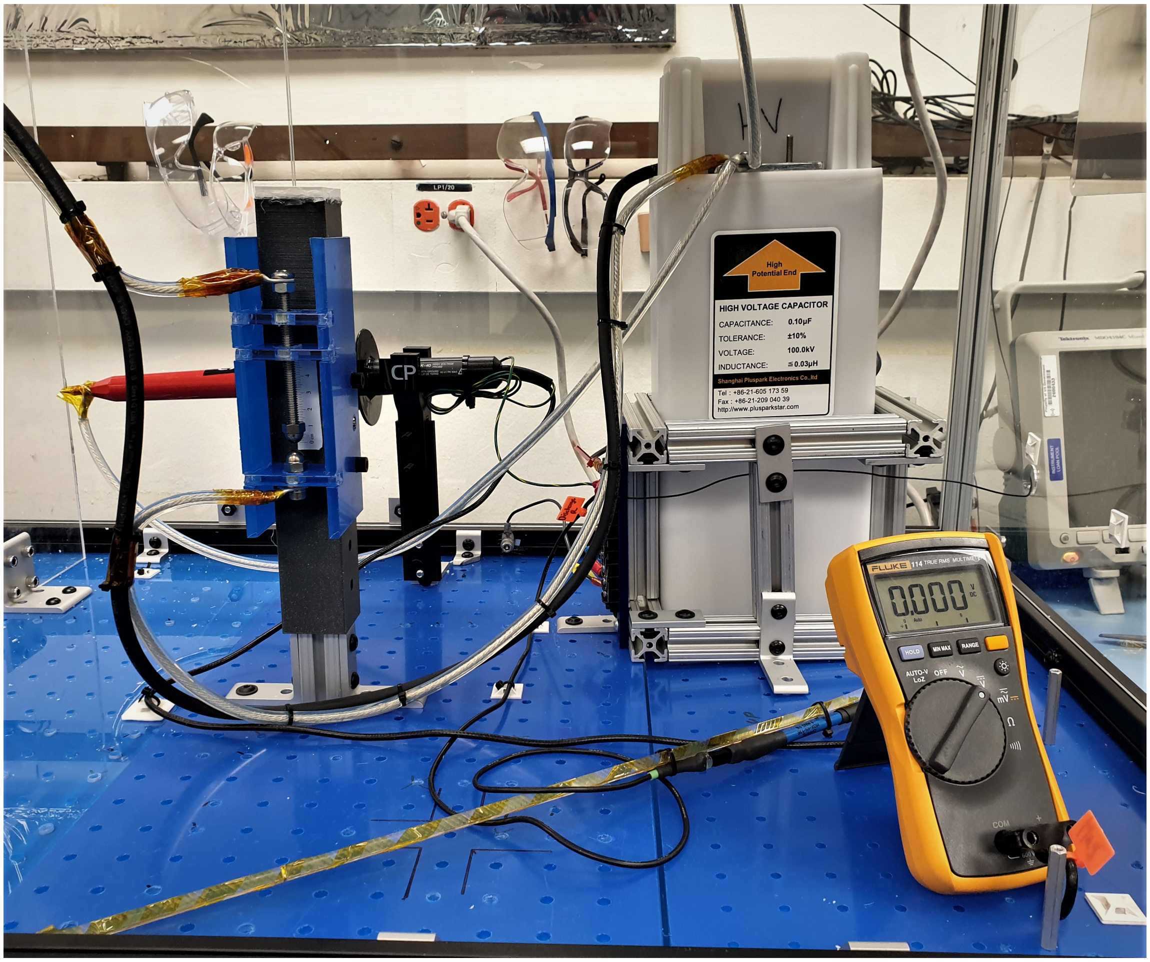

Figure 3.17: Fixed spark-gap architecture.

All power supply controls are still operated remotely through a GUI on a laptop and an LED screen still displays telemetry such as power supply voltage.
This setup is much more resistant to EMI than the servo setup and discharges up to 40 kV are tolerated - although reference signals are seen to drop to an almost $0V$ during the discharge.

Even with all of these simplifications, the setup eventually suffered an anomaly which damaged once again the power supply's $10V$ reference.

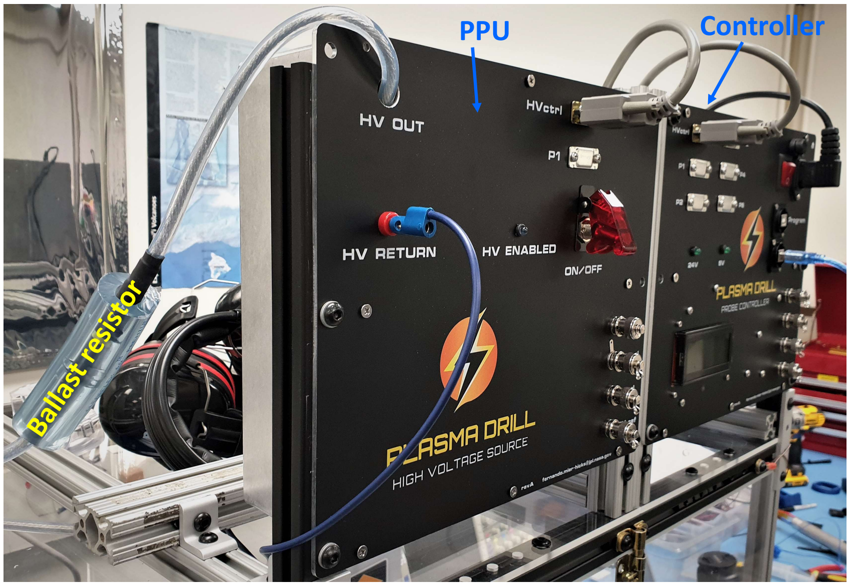

Figure 3.18: Spark gap setup, controller and power supply enclosures.

It is still unknown if the anomaly occurred due to an excessively inductive load in the experiment chamber which caused an unusually large EMI pulse, or if the system gradually degraded by the action of voltage dips which were observable after every discharge.
One aspect that substantially increased the severity of this anomaly is that the small form factor power supply is protected from internal arcing by potting the whole assembly in epoxy. This makes maintenance and component substitution impossible. So even though only a cheap integrated circuit was damaged in the anomaly, the whole PPU is rendered all but useless.

3.5 Fully manual setup

The degree of un uncertainty surrounding the previous anomaly's exact cause in conjunction with the cost and lead time of the "small factor" power supply warranted a further reconsideration of the system's complexity.
As can be seen in 3.19, the digital control and telemetry system is completely eliminated while the discharge circuit is maintained unaltered as it already is in the simplest possible configuration. The Power supply is also substituted by a "hobby grade" solution capable of reaching 40kV (figure 3.20). Controlling the power supply's state (on/off/set-point) is

conducted through a rotating-knob potentiometer which activates the power supply when unlatched and controls the voltage set point proportionally to the angular position. Power supply output voltage can be read on a dial on the power supply while capacitor voltage is read on a multimeter inside of the enclosure as for the previous setup.

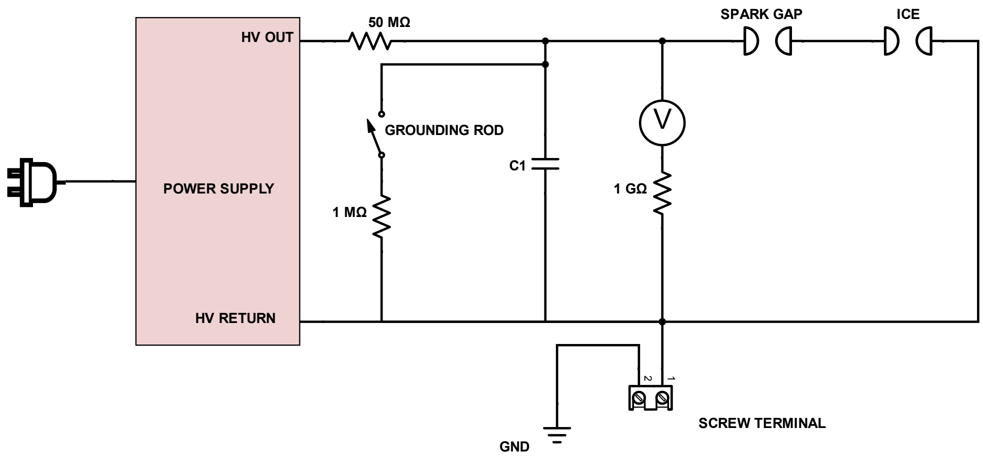

Figure 3.19: Fully manual experimental setup circuit

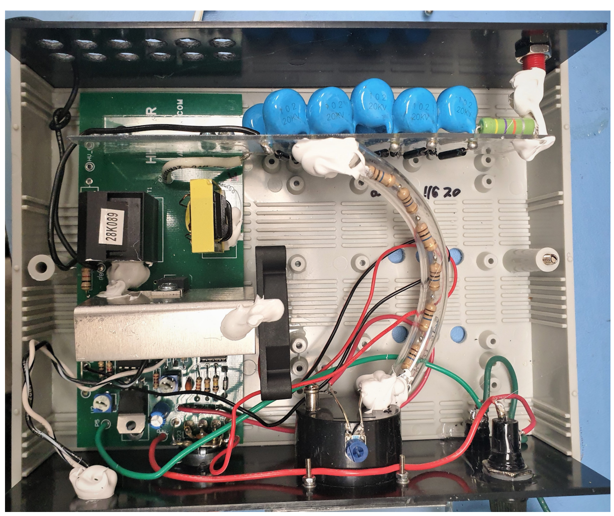

Figure 3.20: Fully manual power supply internal components

Chapter 4

Thermal conductivity experiments and ice making

4.1 Introduction

Quantifying thermal conductivity reduction in the cracked-ice region is key to predicting energy savings that a plasma drill might manifest when compared to a regular thermal probe by using the model described in Chapter 2. The high voltage setup described in Chapter 3 is used to answer this specific question.
In this chapter, there will be described the ice sample's preparation process, sensor mount, experimental procedure and results.

4.2 Ice sample preparation

Ideally, an accurate sample of planetary ice would be prepared and maintained in conditions which are as close to the real environment as possible, especially considering that both thermal and mechanical ice properties change with temperature and freezing profile [71]. An experimental chamber capable of simulating planetary conditions is a very complex and expensive system and budget-related constraints resulted in much less fine-control over ambient parameters. The ambient-controlled part of the setup in fact consists of a commercial-grade freezer with operating temperatures contained between -20 to $-24\ C$; Ambient pressure is also non-controlled and therefore is always equal to atmospheric values.
Consequently, the crystalline structure achievable by freezing in these ambient conditions is limited to Ice I_h (hexagonal lattice) and samples will differ depending on the type and number of imperfections in the crystalline lattice [72] [73].
Interestingly, ice I_h is also the stable crystalline structure at Mars' atmospheric conditions ($< 600Pa,\ \ 170 - 200K$) [74].

Even considering the mechanical and thermal properties variations that occur within the stability range of ice I_h, all the ice manufacturing limitations with the setup were deemed acceptable for a preliminary technological proof of concept. Further work will be necessary to investigate discharges in cryogenic, hyperbaric and firm ice.
Initially, small, 3D printed containers were frozen in bulk to identify problems linked to sample preparation and sensor embedding. A number of issues were identified with the procedure of filling up a sample and directly placing it in the freezer:

- Risk of container deformation / failure due to ice expansion. Even compliant containers made out of plastic materials have the tendency of bulging to the point at which maintaining an upright position is problematic.
- Lack of visual clarity due to impurities being trapped in the freezing sample. This "cloudiness" degrades the sample's visual appeal, but can be accepted for tests which aim at measuring thermal conductivity as it was found that it did not modify excessively control readings.
- Significant in-ice cracking generated by the freezing process. This is especially troublesome as the experiment's aim is to determine the thermal properties of cracked ice and a damaged control sample introduces unacceptable errors.

All of these problems are related to the way that ice freezes in a container placed in a uniform temperature field (Figure 4.1) which will be shortly described in a qualitative manner. After nucleation, ice sheets start growing inward from all of the water mass' external surfaces. A thin sheet slowly increases in depth and traps a water pocket in the central region of the container. This water cavity takes is thermally insulated from the external ambient by the ice sheets and thus the freezing rate slows progressively down. When the water pocket freezes, there is no place left to accommodate the volume increase that accompanies water to ice I_h transition; consequently, as chamber volume decreases, water pressure increases and eventually enough strain gets transferred back to the ice so that large stress-induced cracks form and the container bulges outward. The formation of a surface ice sheet also contributes to the trapping impurities in the water pocket, which then lead to "cloudy" ice sample.

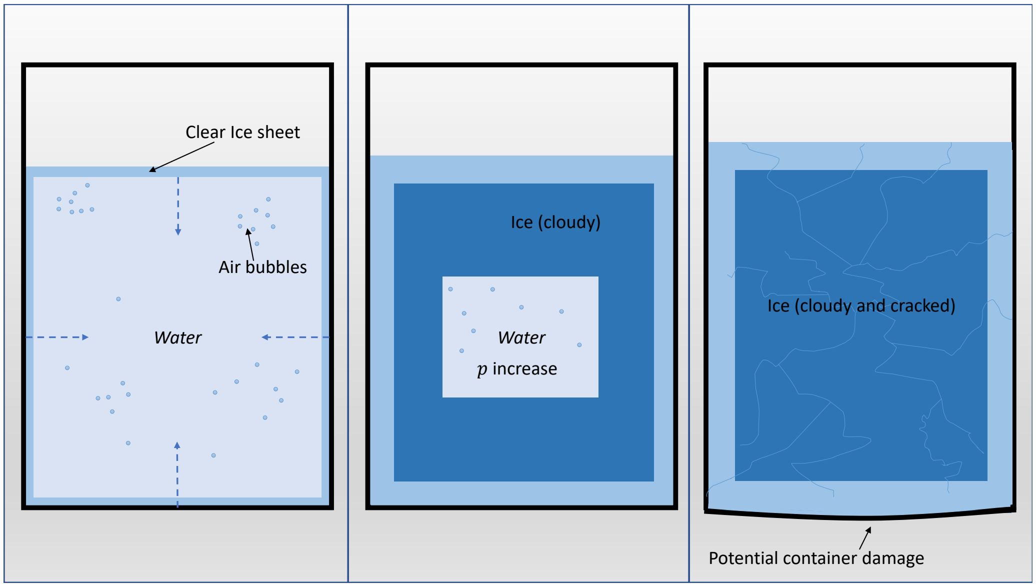

Figure 4.1: Ice sample preparation, bulk freezing.

Directional freezing can be leveraged to solve all of the aforementioned problems. As depicted in figure 4.1, there is always an outer clear-ice sheet when freezing a sample. Therefore, a clear slab can be extracted by forcing the initial ice sheet to grow directionally from only one of the water sample's external surfaces. This can be achieved in two different ways:

- Leaving a cooler with an open lid inside of a freezer (figure 4.2). In this way, a top-down layer of ice starts developing and the freezing process must be interrupted before the whole sample freezes over, as that would create the same "water pocket" effect in the lower part of the container, thus risking to damage the cooler and crack the clear-ice slab above. Additionally, it has to be considered that when insulation provided by the ice slab matches that of the cooler's walls, mono directional freezing will cease and an ice layer will start to grow from the cooler's walls.
  The downsides relating to this ice sample creation technique are numerous. Firstly, the ice-slab removal process is complicated and often results in damaged, uneven slabs. Secondly, inserting sensors and mounting structures is difficult and might interfere with the slab's growth. And finally, experiments requiring significant sample depth (more than 5 inches) are almost impossible as the maximum slab depth is limited by the cooler's sidewalls thermal conductivity and thickness and when omni-directional freezing eventually kicks-in the whole sample is ruined.

- A cooling plate, placed beneath the water sample, can be employed to achieve bottom-up freezing. This process must occur at room temperature to maintain upward-directionality. This is clearly the optimal solution to clear-ice creation as it can lead to thick clear-ice samples. Additionally, sensor embedding is simpler, as it does not require a hanging frame like for the "cooler" approach. Unfortunately, this solution also requires the most space and specialized equipment and was therefore discarded.

An unsuccessful attempt at achieving bottom-up ice sheet growth inside of a freezer was made by removing a cooler's lower insulating layer all the while keeping the insulating lid closed. Unexpected Omni-directional freezing occurred and the clear-ice requirement was discarded in favour of developing an automated, uncracked sample creations system.

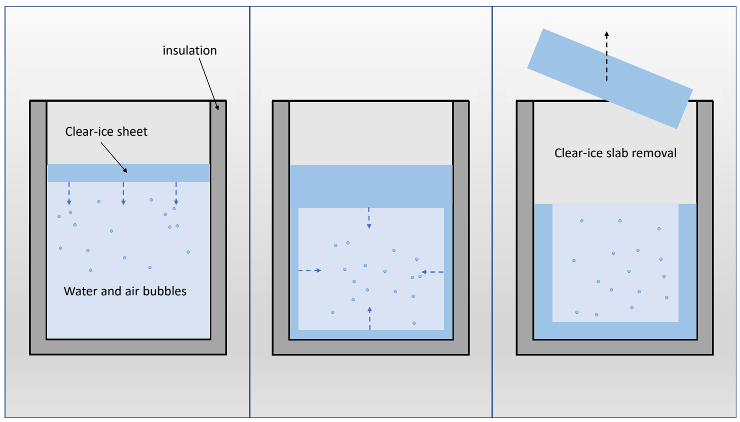

Figure 4.2: "Cooler approach" to clear ice making

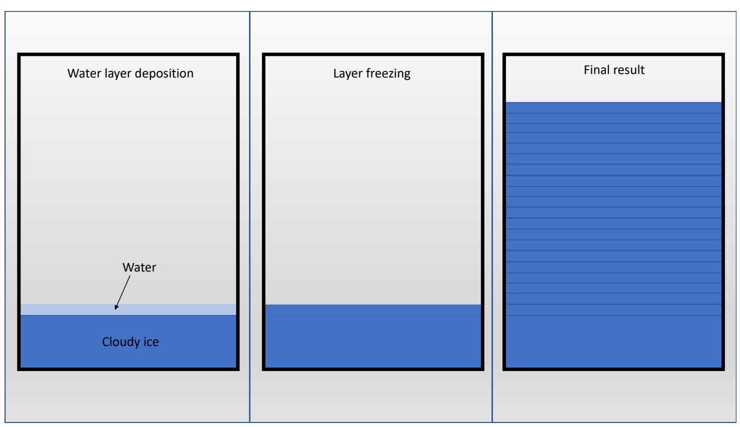

Figure 4.3: "Layer by layer" approach

4.2.1 Layer by layer approach

Once the requirement of having a clear ice sample is removed, all attention can be devoted to avoiding cracking and container-deformation and to reducing as much as possible work-load on the system operator. This can be achieved by depositing very small layers of water and waiting for each layer to be fully frozen before proceeding with the next layer (Hence the name "layer by layer" approach - figure 4.3). In this way, each layer does not trap a large pocket of water in its midst while freezing and thus avoids strain on the container and cracks in the sample itself. Additionally, embedding sensors and mounts becomes trivially easy as care has to be devoted solely to using a structure to fix the sensor's location. The main drawback of this approach is the cloudiness of resulting ice and the potential cracks induced by thermal shock when warm water is deposited on an ice layer that has reached temperature equilibrium with a freezer at $-20C$. The last drawback can be solved by adding water when the previous layer has just frozen-in and has not reached equilibrium temperature with the freezer.

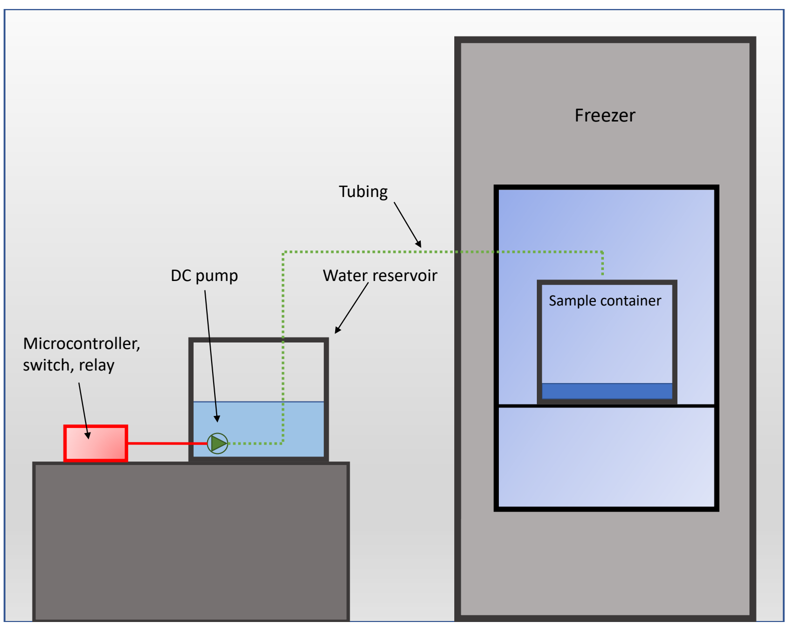

Figure 4.4: Ice sample creation system

The system's schematic can be observed in figure 4.4. Two reservoirs, one full of water and another empty are placed respectively outside and inside of the freezer and are put in communication via a tube. Water can be pumped from the outer to inner reservoir thanks

to a brushless DC pump which is controlled by an Arduino microcontroller that keeps track of time and alternates between a deposition and a freezing state.
In the interest of design flexibility, the system accounts for the possibility of operating 3 pumps concurrently, each with separate layer deposition and freeze times.
As can be seen in figure 4.5, the pumps are toggled via a relay and although this feature is not strictly necessary (The pump could be potentially driven by the current coming from a 5V digital pin), it was placed envisioning the possible use of higher current pumps in conjunction with an external power supply. All electronics are operated by three switches and a small OLED screen displaying relevant information such as pump status ("ON/RUNNING/OFF"), number of layers that have been deposited and time to the next layer. Controller and circuitry are enclosed in a simple 3D printed box (figure 4.6).
An important obstacle to automation that was quickly identified is the tendency of some water to freeze in the tube with each layer deposition, eventually causing a blockage; this required adding a heater driven by an external power supply on the tube's tip.
Ultimately, the effectiveness of this system comes into play only if layer deposition and freezing times are fine-tuned for different container geometry.

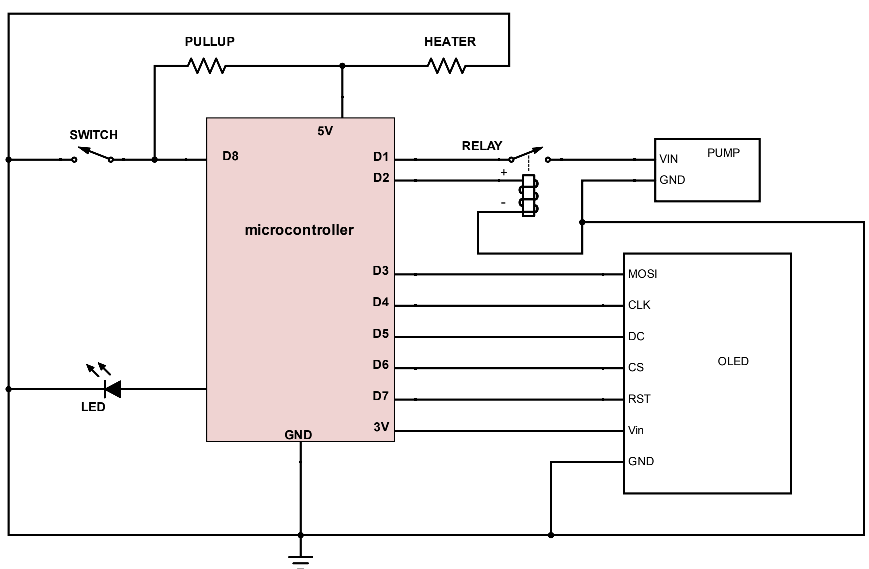

Figure 4.5: Electrical schematic of layer by layer system. Microcontroller here is treated as a voltage source.

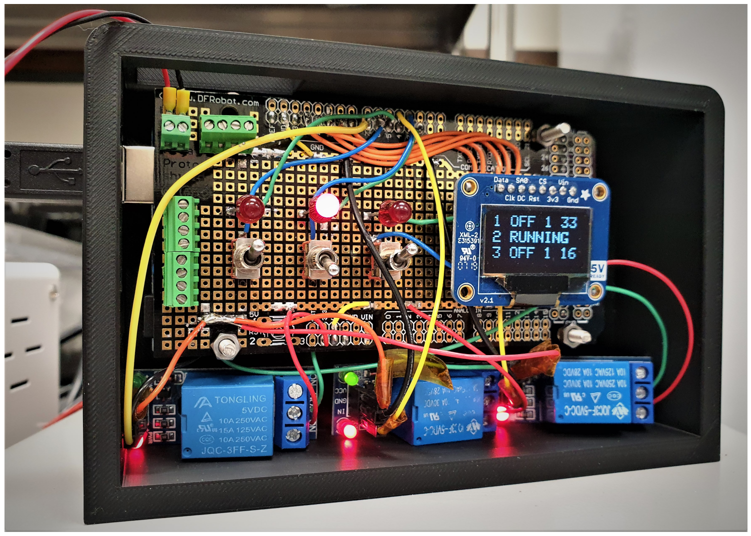

Figure 4.6: Pump controller

Thermal conductivity values for an ice sample depend on a number of factors such as aeration, freezing time and external temperature [75]. Layer by layer samples seem to be heavily aerated which results in a slightly lower thermal conductivity than clear ice.

4.3 Thermal conductivity experiments and results

Thermal conductivity k is defined as ability of a material to transmit energy via diffusive processes and it is measured in Watts per square metre of surface area induced by a temperature gradient of one Kelvin per meter [76]. The relation between heat flux, temperature gradient and thermal conductivity lies in Fourier's law of conduction:

$$q = -k\nabla T$$

Thermal conductivity measurement techniques consist in generating a heat gradient and recording the resulting temperature field once it has reached a stationary condition or processing a time-varying signal deriving from non-stationary temperature variations.

Regarding the choice of measuring method, instationarity proves to be the most time-efficient solution, as it does not require the system to reach equilibrium, which can be a lengthy process - especially in low thermal conductivity mediums. Additionally, methods that require to place the sample in a specific measuring apparatus such as the "guarded hot plate" method are impractical to measure the aftermath of a discharge as they require

a large homogeneous sample and the removal of all sparking electrodes.
A method which is particularly apt at measuring local thermal conductivity changes and which also facilitates sensor embedding is the "hot wire" method. This technique consists in passing a current through a heater embedded in the sample and subsequently monitoring the cooling rate.

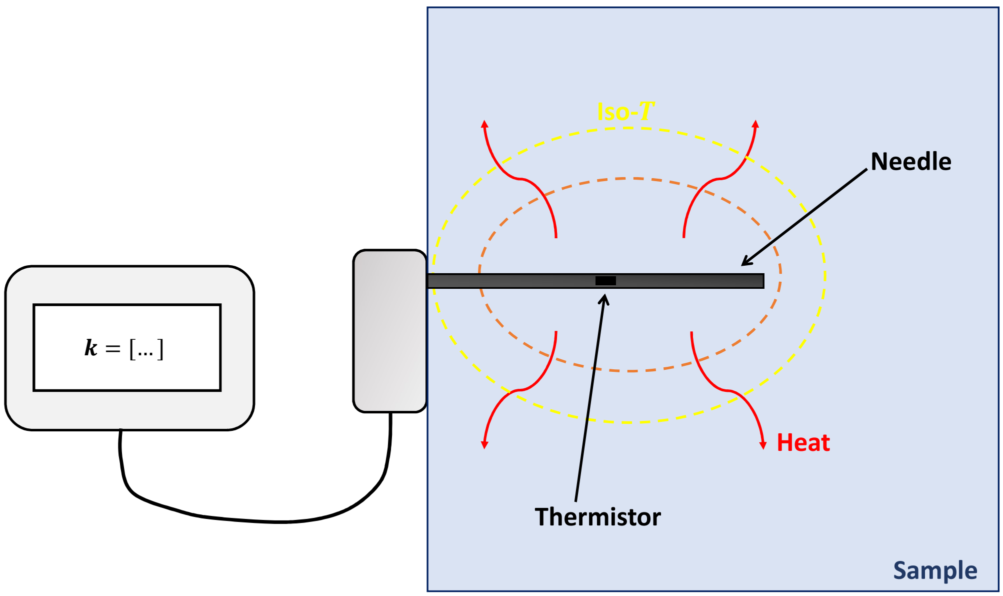

Figure 4.7: KD2-pro thermal properties analyser schematic of operation.

A commercially available thermal properties analyser (K2D pro) is employed thus avoiding having to develop a reading apparatus with annexed signal analysis.
The instrument uses the transient hot wire method and is composed by a processing computer and an interchangeable measuring needle which is internally composed by heater wires and a thermistor (seen in figure 4.7).
There are a number of aspects that have to be kept under control in order to minimise measuring errors in the thermal conductivity readings. These aspects have driven both sensor mounting philosophy, power settings and experimental procedure.

- Good thermal contact between sample and needle is important to avoid lowering fictitiously thermal conductivity readings. This consideration leads to the decision of freezing-in the thermal conductivity probe with the sample instead of drilling a hole in an already frozen ice block.

- In the presence of convection in the sample, energy removal would occur at a higher rate than with diffusion alone; thus, the thermal conductivity reading becomes fictitiously high. Convection in an ice sample can occur when there is phase-change at the interface between ice and needle; therefore, all thermal conductivity measurements are performed in a freezer and the minimum current setting is chosen.

In order to have the most accurate results possible, the measuring needle is fully embedded in ice and is kept in position by a 3D printed guide, which also serves as a mounting pillar for an electrode holder (a plastic parallelepiped with a hole pattern).
Electrodes are COTS components and their insertion depth is controlled by a stopping feature made out of plastic; their lateral distance is kept to $1.5 - 2.5$ cm as it is close to the maximum breakdown distance achievable with 40 kV in ice. Once the assembly is constructed, it is laid down in the testing reservoir and left in the freezer to fill up with ice using the layer-by-layer system.

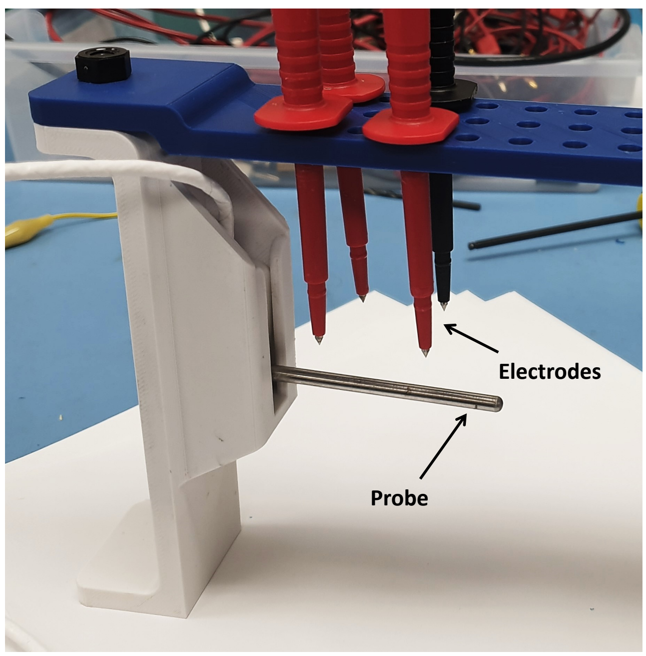

Figure 4.8: Mount for electrodes and measuring needle.

It is worth spending a few words on the cracked region's topology as it can help interpret some of the differences in thermal conductivity readings.
In the electrode's close proximity, there is a region of extremely cracked ice - almost at the

point of resembling a powder of ice shards. This region is expected to have the highest thermal conductivity reduction factor as crystalline structure disruption is at a maximum. Immediately surrounding, there is a larger region of densely cracked ice. Radial crack planes here are the predominant feature, although they are occasionally accompanied by tangential fractures. This leads to expect a thermal conductivity which is somewhere in between undisturbed ice and powder; especially considering that the thermal path to the ice bulk is mainly disturbed by tangential cracks which are not the predominant feature.
In the sample's remainder, there are only few large cracks which likely occur along planes already weakened by stress concentrated during the freezing process. This region should has an almost unaltered thermal conductivity.
After each test and prior to preparing a new sample, the experimental procedure requires a visual inspection of the previous sample to determine in which region the probe had fallen in. The majority of experimental results come from samples looking like figure 4.9, with the needle entirely submersed in the dense fracture pattern.
Two tests in total were conducted with the needle partially embedded in the Pulverized region and resulted in the lowest thermal conductivity readings. Unfortunately, the electrical environment in the electrode's close proximity is extremely aggressive and accidental arcing through the needle can cause irreparable damage to the thermistor or wiring. This aspect limited the number of total thermal conductivity measurements in the most cracked region. Further testing is advised specifically in quantifying with more accuracy the difference between densely cracked, pulverized and normal ice. Additionally, geometrical aspects such as the volume or radial extent of each region should be investigated and fed back to the finite element analysis.

Data from all experiments was collected using the automatic sampling technique available in the KD2-pro thermal properties probe. Each measurement is followed by a 15 minute cool down interval in which any temperature disequilibrium generated by the measuring heat pulse is nullified.

Once the sample, probe and electrodes are frozen in place, the testing procedure consists in collecting control data, discharging in ice and measuring once again cracked ice properties.
This first testing phase aims at providing a rough estimate of thermal conductivity reduction values for the various cracked regions and does not look at any dependence on the number of discharges or sparking energy - these last aspects are left for further work.
Consequently, each test is performed with a sufficient number of discharges that ensure full development of the cracking pattern. Initial observations suggests that $2-3$ discharges are sufficient to reach a point of diminishing returns in thermal conductivity reduction and a topological lack of change in the cracked region.

Results are sorted in three files depending on the outcome of the visual inspection made after each test is concluded.

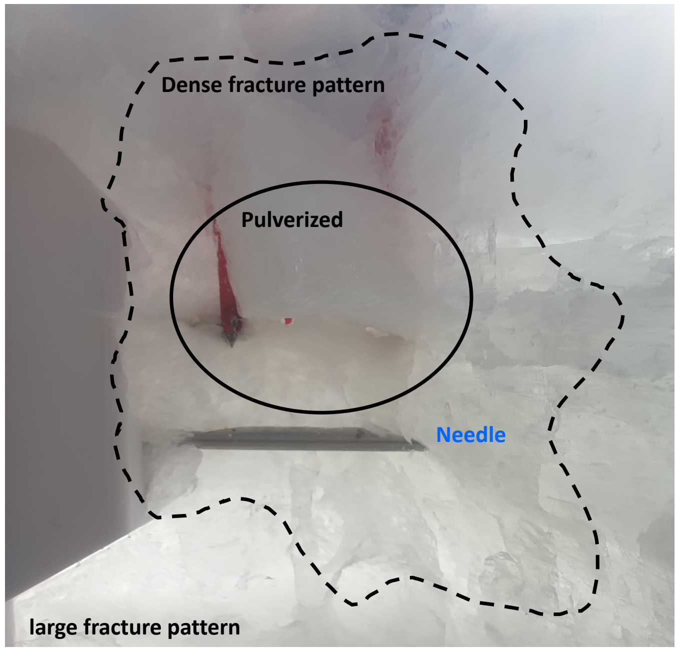

Figure 4.9: In ice fracture pattern.

Firstly, there is the control group. Then, there is the cracked data for tests in which the thermal conductivity probe ended up in the densely cracked region (figure 4.9) and ultimately, there is the telemetry from two tests in which the probe ended up in the "Pulverized" region (figure 4.10).

Errors due to imperfections in the measuring system are random in nature and thus lead to normal distributions in thermal conductivity readings.
The freezer is itself an imperfect system and each test is characterized by an oscillating temperature profile with a median value that changes slightly in-between tests and is distributed in a non-normal fashion as can be seen in figure 4.11 by looking at the cumulative probability function's shape.

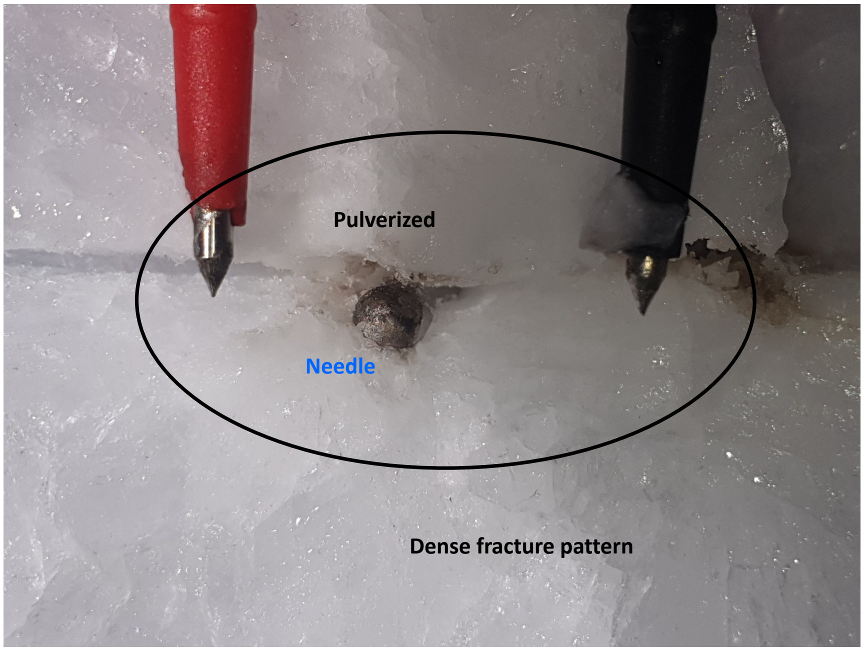

Figure 4.10: In ice fracture pattern part 2.

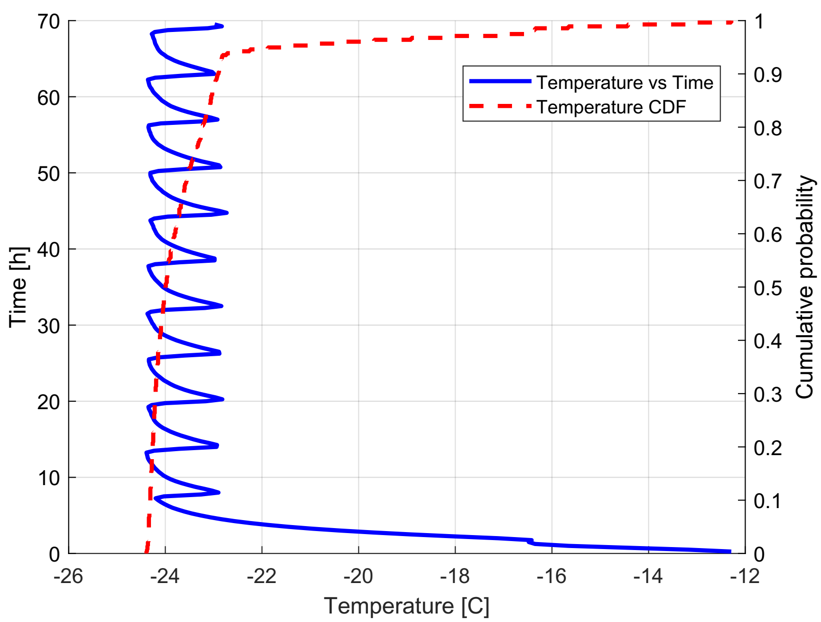

Figure 4.11: Ice temperature profile as a function of time together with cumulative.

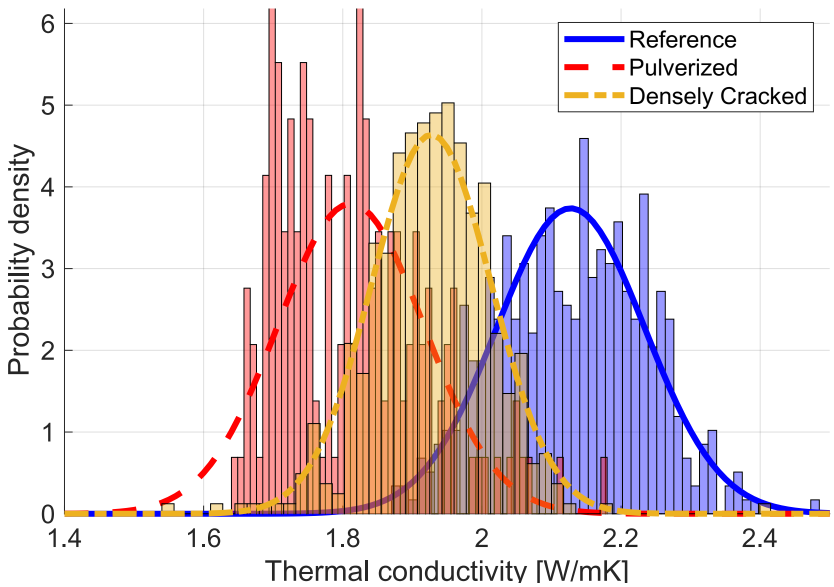

Figure 4.12: Probability density distribution of thermal conductivity measurements in various regions of the cracked sample.

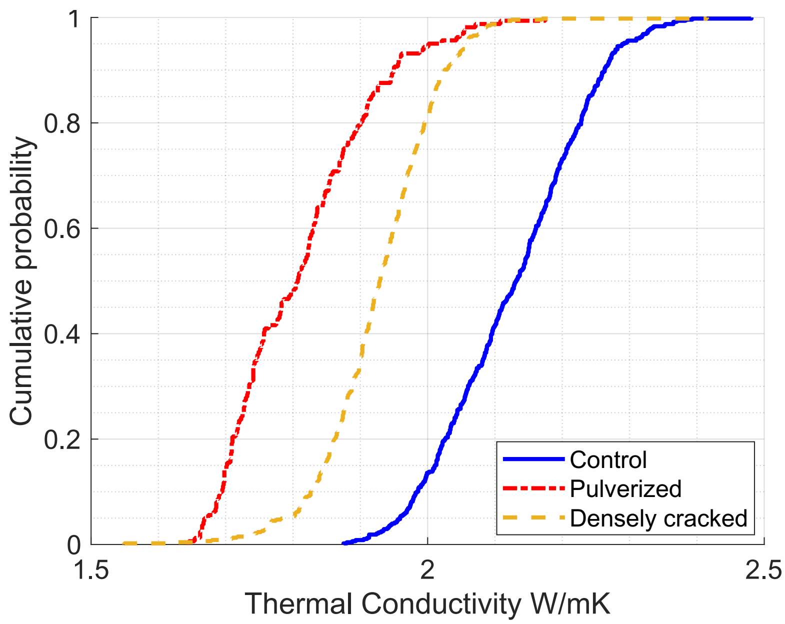

Figure 4.13: Thermal conductivity cumulative probability.

Probability distributions are fitted using MATLAB's statistics and machine learning toolbox and relevant parameters are computed.
As expected, the thermal conductivity readings show a progressive decrease depending on cracked region topology (figures 4.12 and 4.14). The "Pulverized" data set suffers from having the least number of tests to draw from; this results in the largest standard deviation as can be seen in table 4.1. Another systematic error, which causes an unusually large number of sub-2W/mK readings to appear in the control data, stems from an experiment in which the sample's starting temperature was -2C; in fact, ice's thermal conductivity decreases as temperature approaches $0C$.
95% confidence intervals (or 2 standard deviations) are depicted in the red error bars in figure 4.14; the densely cracked region readings seem to be the most accurate, while both control and pulverised readings display more variance.

The results from one of the most promising tests are depicted in figure 4.15. This is the only test in which the thermal conductivity probe was fully enveloped by the pulverized region for the whole duration of the test (the second time in which the probe ended up in the pulverized region resulted in a damaging anomaly when cross-sparking). This test here shows on average a 25% reduction in thermal conductivity.

An additional aspect to note is that the electrode stand was perfected over time by gradually decreasing separation between needle and electrodes up to the point at which arcing through the needle becomes unavoidable. Some tests in which not enough ice was present in the sample resulted in higher-than expected thermal conductivity reduction readings because of an excavation phenomenon that resulted in material removal instead of fracturing.

Ultimately, the error bars in figure 4.14 hint at the necessity of further investigation with a more accurate measuring technique in order to state with higher confidence thermal conductivity reduction values for the various cracked regions.

It is also worth remembering that the sample creation technique is a further source of potential errors as it skews control samples towards lower thermal conductivities due primarily to high gaseous intrusions. At this point it remains unclear if using perfectly clear ice will maintain relative gains from cracking constant or if cracked thermal conductivity values remain unchanged, thus increasing relative gains or if there are other phenomena that might cause further variations.

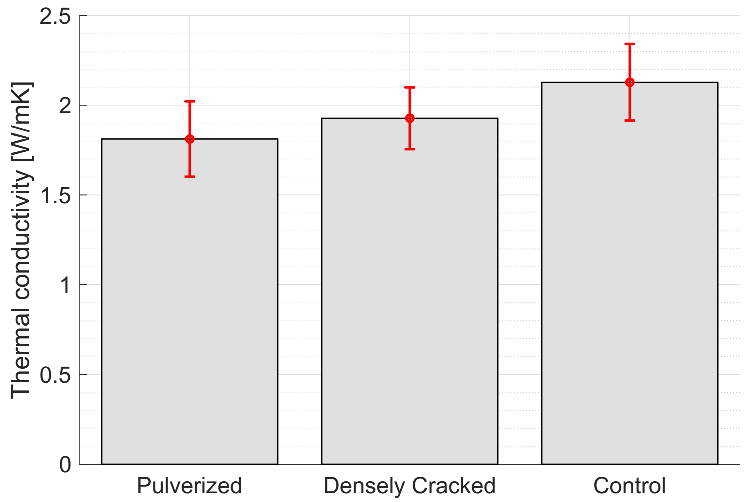

Figure 4.14: Median thermal conductivity measurements.

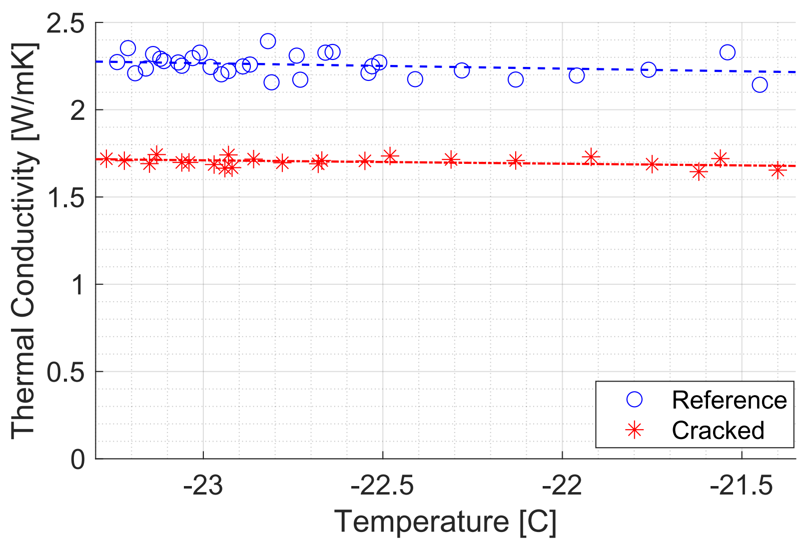

Figure 4.15: Thermal conductivity readings reference and cracked ice in pulverized region.

In conclusion, plasma induced thermal conductivity reduction of up to 25% has been demonstrated. Nevertheless, there are a number of open questions persisting around planetary plasma drilling.

Firstly, ice's mechanical and thermal properties are subject to large variations with ambient temperature and formation process. This work has only investigated ice at $-20 - 24C$ formed with a layer by layer methodology. Further work is surely going to be necessary to investigate different ambient and formation conditions tailored specifically for a planetary body.
In second place, it remains unclear whether the thin melt water film around the plasma drill, which is necessary to enable downward motion, would "seep in" the cracks thus nullifying any thermal conductivity reduction and creating dangerous hotspots on the probe's sidewalls. It is also poorly understood if there is the possibility of downward motion enabled solely by repeated cracking.
Ultimately, a thorough investigation on the effects of discharge energy, distance between electrodes and number of sparks is also missing.

Region	Control	Densely cracked	Pulverized
TC median [W/mK]	2.13	1.93	1.81
Standard deviation	0.107	0.086	0.105

Table 4.1

Data set	Control	Densely Cracked	Pulverized
Number of measurments	480	467	162

Table 4.2

Chapter 5

Probe design and testing

The primary purpose of this project is to work towards an experimental comparison between a plasma drill against a regular thermal probe's performance. Real-world results can be far more convincing than small scale experiments in conjunction with modelling when trying to prove a point; this is particularly true for complex systems governed by multi-physics phenomena that are always subject to the risk of over-simplification in the process of making assumptions.
This chapter will describe the efforts relating to the design and construction of a working thermal probe and the modifications that transform it into a plasma-drill. Additionally, the experimental setup designed to enable a direct comparison between the two systems is also described.

5.1 Thermal probes

Thermal drilling is a widely investigated technology [30], but the need to build a low-cost system compatible with the setup's dimensions led to re-learn a number of lessons.
A large effort was placed on using almost entirely Commercial Off The Shelf components with the exception of 3D printed plastics and some minor machine shop modifications to existing components.
Additionally, the thermal probe was designed with the requirement of supporting an easy conversion to plasma drill with only minor alterations.

The most important components in a thermal probe are the heaters that transform electrical energy into heat via the Joule effect. Power in a cable is dissipated proportionally to the current's square times the wire's resistance.

$$P = RI^2$$

Hence, in order to dissipate as much heat in the desired region as possible, heaters are made out of materials which have higher resistivity than the copper wire that connects them to a power source. Nichrome is the most common heater-material and it is a Nickel-Chromium alloy and has sufficiently high resistivity (between $100 - 150 * 10^-8\Omega m$), a high melting point ($1400C$) and forms a protective oxide layer analogously as Aluminium. The main difference between heaters is often how the wire is packaged. Thermal probes are ideally suited for two types of heaters:

- Cartridge (or tubular) heaters consist in two helical coils - one that goes to the positive end of the power supply and one that goes to ground - that lie within an electrically insulating compressed powder that separates the wires from an external metal casing. These heaters are easily integrated in cylindrical geometries.
- Flexible heaters are a planar circuit of heater-wire that is insulted electrically from the external environment by being encompassed between two surfaces of plastic or rubber such as Kapton tape. As the name suggests, flexible heaters can be easily deformed and can be wrapped around any shape.

Both of these types of heaters find use in the thermal probe designs described in the following pages.

5.1.1 Thermal probe V1

The first thermal probe iteration has a single large flexible heater that is wrapped around the 1.25 inches of an Aluminium tube's internal diameter. The heater does not wrap fully around, but leaves just enough gap to feed through three thermocouples and two power cables. An internal clear plastic tube serves to press the heater against the external Aluminium tube and creates a cavity in which tip-related cabling can pass unobstructed. There is no tail section as this iteration is not designed to be fully submerged in ice. The internal plastic tube extend far beyond the external tube's end and is fed through a simple guiding mechanism to maintain orientation when testing.

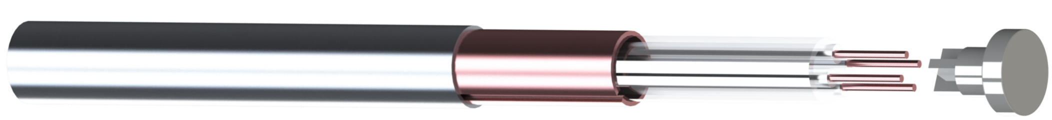

Figure 5.1: Thermal Probe first version render

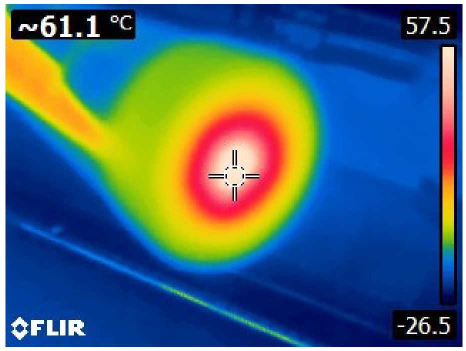

Figure 5.2: FLIR image of the thermal probe's tip section with heaters turned on.

The tip assembly is made out of two components. Power is provided to a number of cartridge heaters which are kept in place by a holding plate.
This structure is initially designed to hold four custom soldering iron heaters which have a small diameter ($< 5mm$) and come all pre-equipped with a thermocouple for temperature control.
The use of so many cartridge heaters comes from the though of using the heater's external metal casing as an electrode for the high voltage discharge. Early testing showed that the heater's internal thermocouples were malfunctioning, which lead to a slight modification to the tip assembly by introducing a single, centrally mounted cartridge heater ($8mm$ diameter) and two independent thermocouples embedded in the structure at different radial distances. This modification also increases heater ease of acquisition in case of malfunction, as the custom cartridge heaters are difficult to replace.

Waterproofing the probe's interior is necessary to avoid internal shot-circuits. There are many different ways to achieve water-tightness and in this first probe configuration that is not designed for operation under any significant pressure, assembly mates are only press-fitted. The tip structure is 3D printed using Stereolithography which results in less porous components than Fused Deposition Moulding and thus exhibits better water-tightness characteristics.
This holding structure has an external sleeve which can be deformed to wrap around the Aluminium tube's external diameter. Water tightness along the sleeve-tube interface is ensured by applying a semi-permanent sealing epoxy that can be removed by heating the tip at $80C$.
All wires are routed in and around the plastic guide tube and end up in a controller which governs heaters and measures temperatures.
An Arduino microcontroller is used to read the thermocouples, compare temperatures with a desired set-point and adjust power flowing to the heaters using a PID controller. As the

cartridge heater's operating voltage is $115V$ (reduced to $< 60V$ to avoid significant safety hazards), the microcontroller can not be in direct contact with the High voltage heater circuitry. A current switch based on the use of MOSFET transistors is therefore used to modulate heater power with using logical signals from the microcontroller.

Initial tests of this configuration showed a disappointing thermal performance of the tip-structure assembly (figure 5.2) that lead to an impossibility of penetrating any ice at $-24C$. In fact, the thermal conductivity of the SLA printed resin is so low, that even with heater temperatures in excess of $90C$ (figure 5.3), there was no penetration. With these conditions in fact, the temperature gradient does not heat up the probe's outer diameter to above freezing temperatures, while in proximity to the axis of symmetry the temperature reached peaks of $60C$. Additionally, even if the whole structure were to be heated up above freezing temperatures by imposing a very high temperature set-point to the central heater, the inefficiencies in heat transfer characteristics would have resulted in low penetration rates.
This problem was expected during the design phase, but not with this magnitude of consequences as no thorough thermal analysis was conducted before the prototyping phase. Additionally, the flexibility given by having a 3D printed tip section was deemed to be worth trying out.

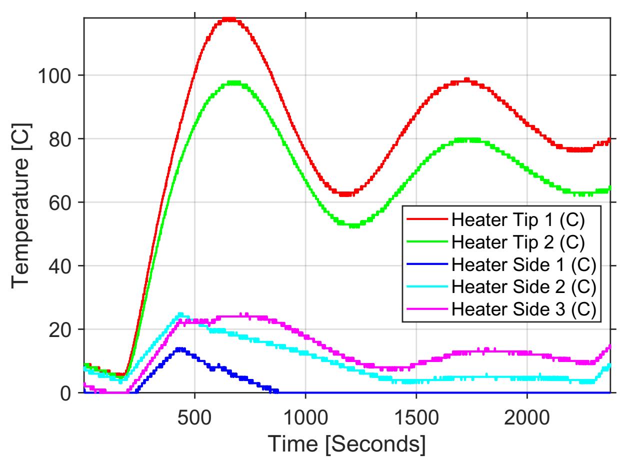

Figure 5.3: Large overshoot, high temperature, sidewall heaters are turned off after $500s$

5.1.2 Thermal probe V2

The second iteration of the thermal probe solves the problems intrinsic to the tip structure by substituting it with an all-metal alternative.
An Aluminium solid rod with the same outer diameter as the sidewall tube is lathed to have a feature with outer diameter slightly smaller than the plastic tube's internal diameter. A cavity for the heater is also lathed along the part's symmetry axis. Two holes are drill pressed at different radial displacements and depths to house thermocouple which are secured in position by the use of Kapton tape. A metal sleeve designed to cover up the tip-tube interface and facilitate water-proofing is lathed out of a larger carbon steel tube. Waterproofing is made more complex by the previous epoxy compound's lack of metal-metal adhesion. In order to avoid more complicated water-proofing techniques, a stronger Silicon adhesive is used. This waterproofing solution results in a permanent seal that can not be broken without damaging the thermal probe itself. This is not seen as a problem, as the system's cost is negligible and can be easily reconstructed in a short period of time.

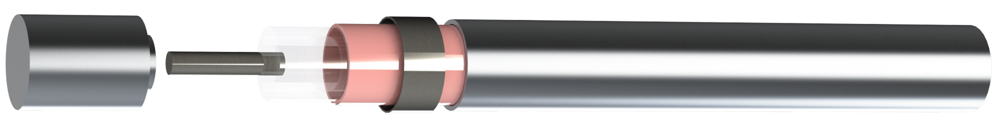

Figure 5.4: Thermal probe V2, render.

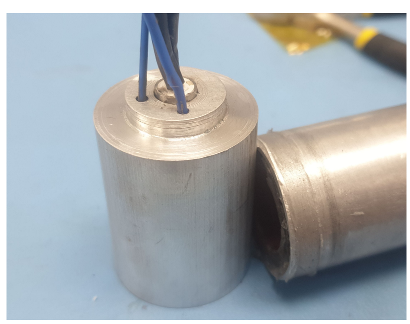

Figure 5.5: Thermal probe V2, lathed tip section with heater and thermocouples inserted in position.

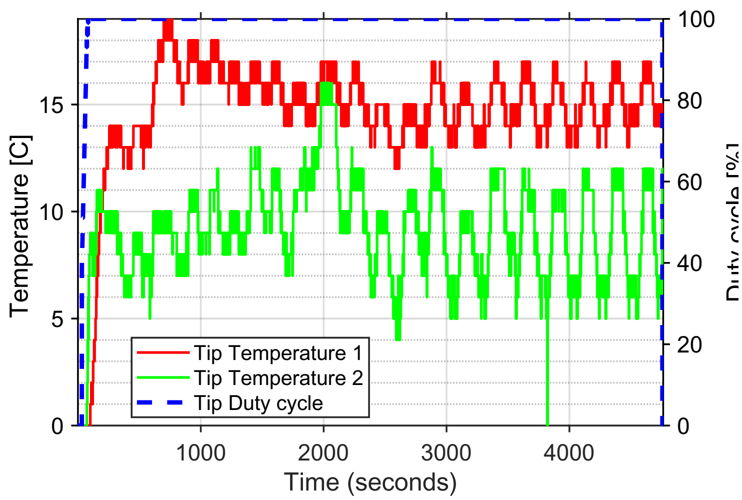

Figure 5.6: Thermal probe V2, telemetry from tip. Note the contained temperature gradient and the fact that the heater is working at 100% duty cycle for the whole test duration.

The controller reads temperature signals from each thermocouple in addition to duty cycle levels for each heater. This data is logged in a *.csv* file for further analysis and debriefing.
Displacement is simply estimated by visually inspecting a graduate meter which is zeroed at the probe's initial position. This thermal probe version is intended as a demonstrator of ice penetration to use as a lesson in thermal probe design and manufacturing; therefore, there is yet no need of accurate displacement telemetry.
Temperature accuracy is within $1C$ and negative temperatures can not be read because of limitations in an integrated circuit part of the first electronics suite prototype. The control software treats sidewalls and tip assemblies as two separate logical entities and does not share thermocouple readings between assemblies. When a temperature set-point is determined for one of the two entities, the software applies temperature control using the highest reading thermocouple within the logical entity as feedback.

The initial set of tests conducted with this second thermal probe prototype were aimed at finding potential usability issues, measuring performance and gaining experience in interpreting telemetry.
The first aspect to note is that the thermal conductivity of the Aluminium tip which is two order of magnitude greater than SLA resins is easily capable of penetrating an ice sample at $-24C$ and the temperature gradient between the two tip-mounted thermocouples is

around $2-3C$ instead of $60-70C$ (figure 5.6).
In addition, the cartridge heater has an electrical resistance of 125Ω which limits the maximum power dissipated through the tip-assembly to $28.8W$, as the power supply erogates a maximum of $60V\ DC$. This electrical power is sufficient to keep the tip temperature well above freezing when submersed in ice ($6-7C$ without, and $17-18C$ with sidewall heaters).
Tip heating alone is not sufficient to stop the sidewalls from freezing in place after having penetrated $4-5$ inches.

An interesting note is that the finite element analysis seems to grossly under-estimate descent rates when compared to experimental results. Even if precise power consumption is difficult to predict without enriching the model with buoyancy forces, probe weight and hydrodynamic effects [25], the order-of-magnitude difference between simulation and real-world in the first $3-4$ inches of ice-penetration might seem puzzling.
In fact, the real system moves at the speed of tens of inches per hour (a precise value is lacking due to the aforementioned experimental setup limitations); conversely, with the same power, geometry and temperature input, the simulation predicts velocities in the order of centimetres per hour. This likely occurs because the simulation considers the probe as a fully submersed body, while the initial phase of each test has only the tip section in contact with the ice surface and thus most of the $28.8W$ of thermal power are concentrated in a small surface which would translate to a much higher overall power if the same power density were to be extended to the whole probe.
Additionally, when most of the probe is out of ice, there is less of a water layer pushing the probe upward due to buoyancy forces. Visual observations seem to suggest that at a constant power, descent rate tends to decrease as the probe becomes further embedded in ice which would confirm the suspicions relating to the discrepancies between simulation and reality.

This rudimentary version of a thermal probe lacks two very important features that are necessary to increase the quality of experimental results. There is in fact no way of plotting an accurate displacement over time curve and the lack of a tail section makes fully submersed operations all but impossible. An improved method to measure displacement is described in the Freezer setup section, while adding a water-proof tail assembly requires substantial changes in the probe's design. In addition, using Silicon epoxy makes it impossible to have a "plug and play" high voltage module which can be easily mounted or unmounted during testing to convert the thermal probe into a plasma-drill and back. This last aspect is more of a nuisance than a real problem, as there would have to be two almost identical probes for the pure thermal - plasma comparison.

5.1.3 Thermal probe V3

For low-pressure applications, threads can be a good way to create an non permanent water seals. This solution would have also been adopted in the V2 thermal probe, but there were no easily acquirable COTS threaded pipes in the same diameter of the previous thermal probe. The flexibility given by threaded end sections - particularly when coupled with the need to have a removable high voltage module - is a sufficiently good argument to redesign the thermal probe with a slightly larger diameter around a COTS threaded pipe and caps.

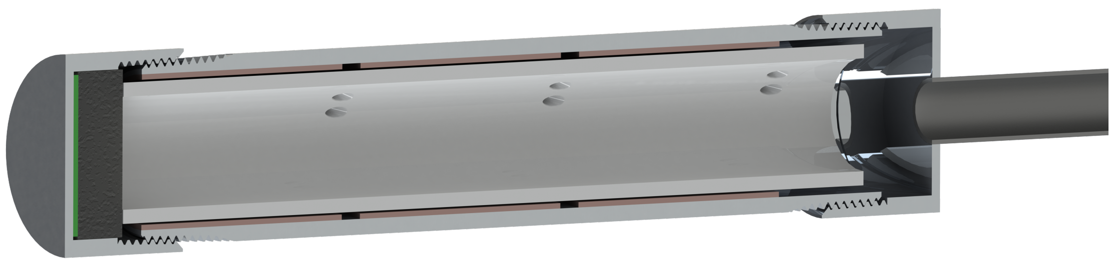

Figure 5.7: Thermal probe V3 render

The external tube is, as always, made out of Aluminium and is threaded on both ends using the NPT standard which allows for a water-tight seal when screwing on a threaded cap with enough torque. NPT stands for "National Pipe Thread" and has a conical shape. The threaded caps are rated to withstand 10 atmospheres of pressure and are thus much wider than the pipe; thus, the cap are trimmed to a much smaller and more uniform dimension using a lathe.
Analogously to the previous thermal probe versions, this probe's "main body" assembly is still composed by an external tube, flexible heaters and an internal tube that pushes the heating elements against external tube's inner surface. In this particular design, a general improvement is that there are three separate sidewall heaters which allows finer control on the power density profile which can be made look like the theoretical power density curve extracted from the simulations of chapter 2 thus wasting less energy in the process.
Double sided tape allows adhesion between flexible heater and internal tube. In addition, there are two layers of Aluminium tape that homogenize the heater's heigh (power cabling and thermocouples are 1.5 millimetres thicker than the nichrome wire). The internal tube

is made out of SLA printed high-temperature resin and has guiding channels that allow for cable management - each section of the pipe has its own power, a single ground and two thermocouple cables.

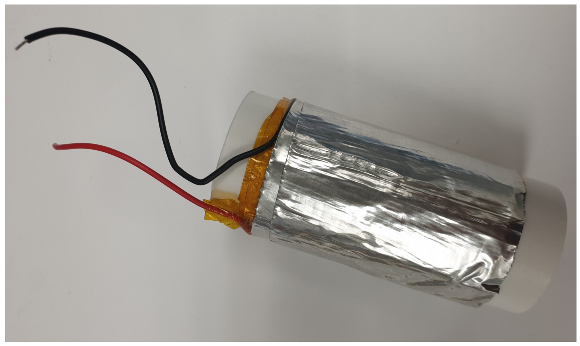

Figure 5.8: Mock-up of an internal body's section

The tip section is powered by a custom circular PCB heater which is pressed against the cap's lower-internal surface. This PCB is basically made out of a wafer on which a heater wire coil is deposited and an insulating surface coating; this solution is chosen as flexible heaters with a circular geometry of the correct diameter were not commercially available. Once positive, ground and two thermocouples are routed towards the probe's rear, the whole tip assembly is potted in a thermally conductive epoxy which serves the purpose of keeping all elements into position (there are no other mounting mechanisms) and improving the thermal path between heating element and the rest of the probe.
The tail section is made out of the same cap as the tip, but in this case, there is a $15mm$ through-hole drilled along the symmetry-axis. This allows to epoxy in position a pipe with ID of $13mm$ and OD of $15mm$ that can serve both as a guiding rod and a cable-routing pathway.

The ideal heat flux distribution around a thermal probe at a given descent rate and ambient conditions resembles figure 5.9 and is computed as the heat flux necessary to maintain a temperature gradient which allows the sidewalls to be just above 0 C. Thus, increasing the number of sidewall heaters allows to optimize the power output's spacial distribution to resemble the ideal case. Starting from the simulation model described in Chapter 2, the sidewalls are divided in three sections and heat-flux requirements are computed and plotted as a function of desired descent rate (figure 5.10) in ambient conditions compatible with the experimental setup which will be described later.

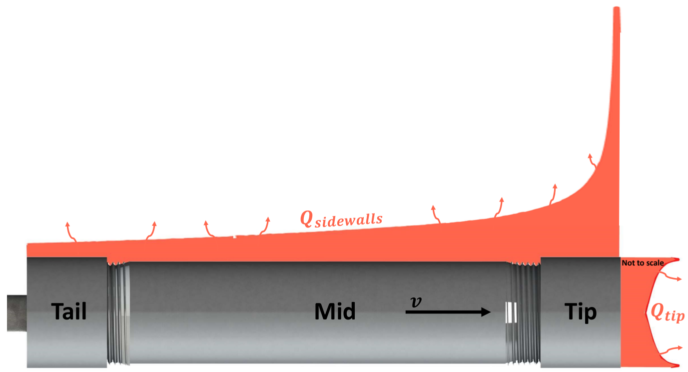

Figure 5.9: Spacial distribution of heat flux

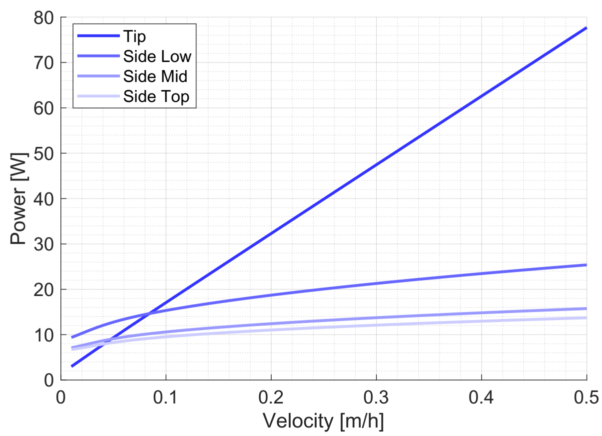

Figure 5.10: Heater power as a function of descent rate

5.2 Plasma drill initial designs

5.2.1 Self embedding electrodes V0

The initial question regarding plasma drill construction was related to electrodes design. At this stage, the idea was still to have a discharging tip. Thus, the nature of interaction between heating elements and discharge apparatus and the risk of unintentional arcing were both open questions.

The first idea was to have self-embedding electrodes that pushed the discharge event as far from the probe's sidewalls as possible by partially melting into ice. From a practical standpoint, this initial idea was to use the metal casing of cartridge heaters both as anode and cathode. Protection from arcing backwards through the heater wires is given by detaching all power cables from all connections before discharging. A first simple prototype was built (figure 5.11) to test potential electrical connections and verify the self-embedding concept out of only 4 components.

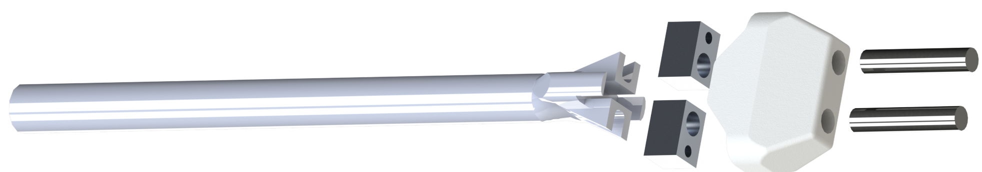

Figure 5.11: Plasma drill V0 render

The cartridge heater is connected to the discharge wire via a rectangular Aluminium block which is drill-pressed to have two holes. One hole has the same diameter as the cartridge heater and allows for electrical contact between Aluminium block and metal casing, while the second hole can house the high voltage wire's banana connector termination. A 3D-printed structure holds both heaters and connectors into position while also providing protection from unintentional arcing between connectors. A 3D-printed guide structure is press fitted into position and further improves arcing protection.

Initial tests of this prototype made evident the insufficient thermal properties of PLA, which has a maximum service temperature of $52C$. When the PLA structure softens up at temperature, the electrodes - which are press-fitted into their holding position - loosen and risk moving from their nominal location. This problem is compounded by PLA's low thermal conductivity which requires much higher temperature gradients to obtain similar heat fluxes to a metal component.

5.2.2 Self embedding electrodes V1

The experience gained with the V0's testing was at heart of the first real plasma drill design candidate.

Similarly to the first thermal probe prototype (In fact they share most of the design), the tip section is made out of an SLA printed structure which houses tightly 4 cartridge

heaters surrounded by an Alumina ceramic tube. Alumina, has in fact a good dielectric strength ($400kV/mm$) and an acceptable thermal conductivity ($30W/mK$). This allows to have self-embedding electrodes and, at the same time, constrains the discharge to occur between tips. Inside the probe, four pieces of thin copper tubing are crimped on the heaters. This helps maintain all components in place under thermal deformations or softening and also functions as a connector for the high voltage cables which could not be soldered to the heater's stainless steel casing.
The rest of the probe coincides with the thermal probe V1 described in a previous section.

This design candidate did not reach maturity and was not subjected to testing, as the insight coming from the model pointed at focusing on reducing thermal conductivity radially rather than longitudinally.

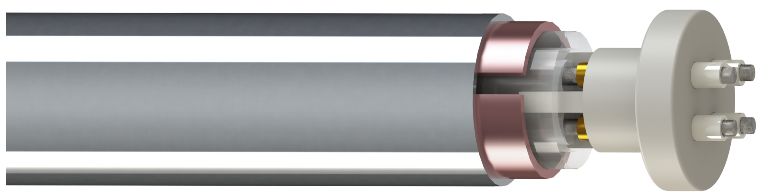

Figure 5.12: Self embedding electrodes V1 render.

5.2.3 Sidewall discharge tests

As ice temperature decreases, a thermal probe uses gradually more power to heat up its sidewalls and avoid refreezing into position. This suggests trying to maximise radial cracking, which can be achieved by moving the electrodes from the tip to the sidewalls in a small "discharging" module.
Deciding a discharge path which minimizes system complexity is an important requirement for the side-wall discharging module. Multiple electrodes all around the external diameter which are toggled with some form of internal high voltage switch are clearly not an ideal solution due to excessive complexity and risk of switch failure. Additionally, it is important to avoid discharging asymmetrically (*e.g.* only two electrodes radially separated by 90 degrees), as this could lead to asymmetric low thermal-conductivity regions which in turn could lead to differential heating and probe instability.

These considerations lead to adopting a configuration in which there are an anode, a cathode and the discharge path is guided 360 degrees around the sidewalls by a number

of floating electrodes. Each gap between these intermediate pieces of conductive material dissipates a fraction of the total discharge energy proportional to the gap's length. Obviously, ground and positive electrodes can not be situated at the same height; that is to avoid discharging directly from positive to ground. Therefore, the discharge follows a helical path.
Each electrode should jut out of the probe's external surface and facilitate the discharge occurring as far from the probe's sidewalls as possible. Flat-head screws seemed to be the perfect prototyping tool as they are very easily acquirable, their mounting requirements are easy to meet (it suffices to have a hole of the correct diameter in which to screw them in) and the head's shape decreases the distance between electrodes at the maximum radial displacement. In addition, the likelihood that the discharge will occur in the desired position is increased by the flat-head's "sharp" side which intensifies electric field at the desired discharge point of origin.

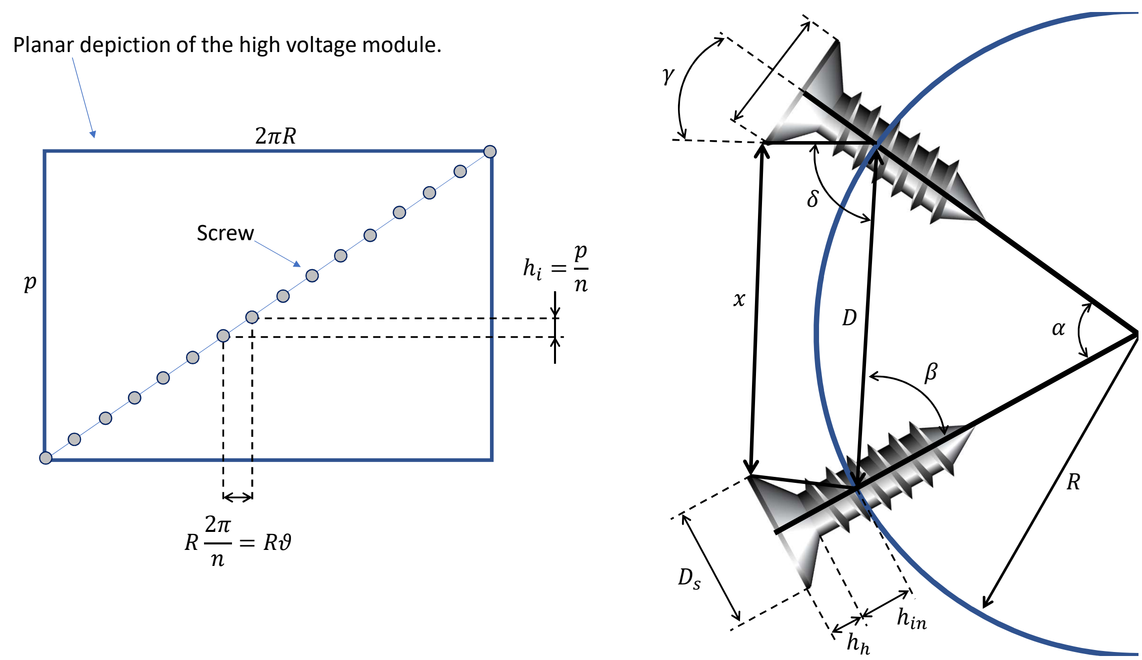

Figure 5.13: Sidewall discharge physical schematic

The screw number is tuned in such a way that the in-ice gap between screw heads is smaller than the helix's pitch by some margin - in this way, the path of least resistance should be along the helix, and axially along the probe walls. These geometrical considerations are modelled in a MATLAB script which takes as an input the type of screw and fundamental helical parameters and recommends a minimum number of screws to equally space along the path to respect the distance constraint.

Considering a helical path with radius R and pitch p, the in-ice gap between n flat head screws which jut from the sidewalls of a distance $h_s = h_i n + h_h$, can be derived from the geometric relations displayed in figure 5.13.
The linear distance D between screws can be computed from the planar linear distance D_p and the height between screws h_i as:

$$D_p = 2Rsin(\frac{\theta}{2}) \rightarrow D = \sqrt{D_p^2 + h_i^2}$$

Now, the in-ice gap can be found by subtracting two times the projection of the "screw hypotenuse" ($s = \sqrt{R_S^2 + h_s^2}$) along the distance D from the D itself.

$$\alpha = 2asin(\frac{D}{2R}) \rightarrow \gamma = \frac{1}{2}(\pi - \alpha)$$

$$\beta = atan(\frac{D_s/2}{h_s}) \rightarrow \delta = \pi - \gamma - \beta$$

$$x = D - 2(s \cdot cos(\delta))$$

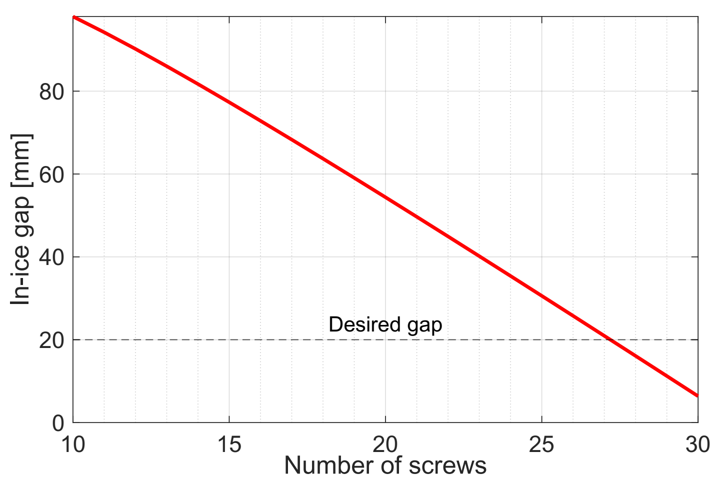

Figure 5.14: Results from the screw calculator

The desired helical in-ice distance $D_{ice} = nx$ is a fraction of the minimum "vertical" distance D_v which can be visually seen in figure 5.15 and is computed as:

$$D_v = p \cdot \cos(\text{atan}(\frac{p}{2\pi R})) \rightarrow D_{ice} < D_v$$

Now the number of screws which satisfies this constraint can be graphically identified by iterating on the number of screws as seen in figure 5.14.

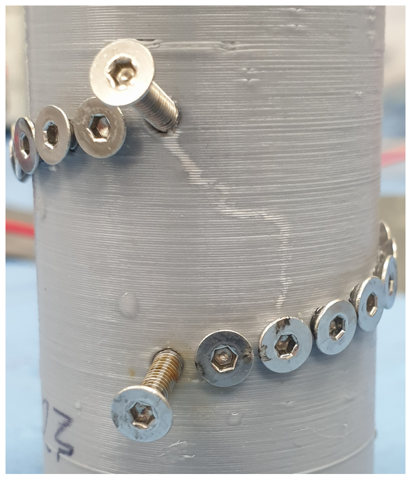

Figure 5.15: Discharge damage on PLA module

To demonstrate the possibility of achieving helical discharges and verifying the screw calculator described above, a series of 3D-printed PLA mock-up high voltage modules capable of housing M2.5 screws were constructed and tested. In this simple configuration, all cabling is external (the structure has in fact a 100% infill) and electrical connections are out of crocodiles or eyelets.
An unfortunate finding is that FDM 3D printing is not precise enough to space out and insert the screws with sufficient accuracy to respect constant sub-millimetre in-ice gaps. In fact, considering a probe diameter of 1.25 inches and a helical pitch of $2cm$ to discourage short-cutting discharges, the number of equally spaced M2.5 screws that calculator returns is 23 (varying slightly with insertion depth). It is then clear that the minimum distance between screws has to be very small and the manufacturing technique has to be correspondingly accurate.
Even if with slightly inaccurate screw-distancing, the possibility of guiding the discharge path was tested, first along half-revolution helical paths (figure 5.16) and subsequently along a full helix revolution (figure 5.17).

A DSLR camera used in conjunction with custom Neutral Density filers was employed to take long exposure images of the discharging event. This tool allows to easily visualize the discharge path and quickly determine problems or identify successful designs.

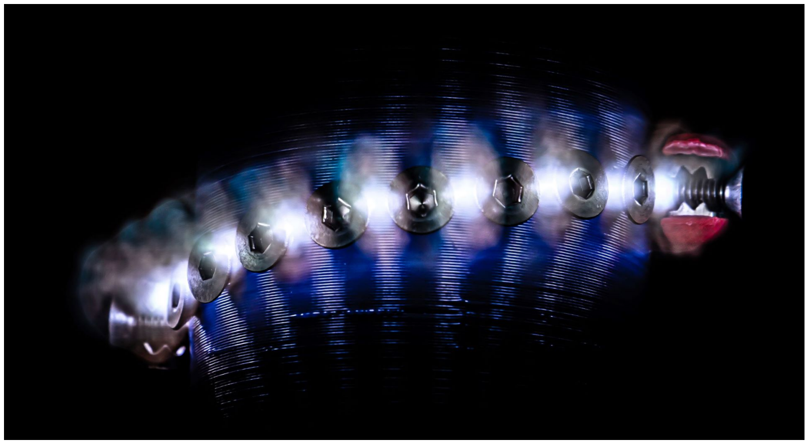

Figure 5.16: Half helical discharge - equally spaced electrodes

Figure 5.17: Full helical discharge - equally spaced electrodes

With equally spaced screws, the discharge energy is subdivided identically in each gap.

Considering a $0.1\mu F$ capacitor at $40kV$ and an "ideal spark gap" which has a unitary efficiency, the discharge energy is of $80J$. In reality, the energy deposited in-ice is much lower than the ideal case, as the discharge rarely occurs exactly at $40kV$ due to the difficulty of fine-tuning the exact required spark gap length; thus, the real discharge voltage is often between $30KV$ and $35kV$; in addition, the spark-gap dissipates 30% of the total available energy.
It is clear then that with screw numbers ranging from $20 - 30$, each gap dissipates under ideal circumstances an energy ranging from 2.6 to 4 Joules.

Texas A&M's Plasma Engineering and Diagnostics Laboratory quantified the densely cracked region's area at a fixed electrode distance with varying energy and found a general increase in cracked area with pulse energy. Below $100J$, there seems to be a lot of variability in results due to unidentified phenomena which make judging cracked area growth type - whether it is linear or non-linear - fairly difficult. Furthermore, the situation at very low energies was not investigated at all.
The first in-ice tests of the sidewall-discharging module pointed at the presence of some form of non-linearity in the cracked region's extent at low pulse energies. In fact, the densely cracked region's area with 20 gaps is visibly smaller than if the same overall energy were deposited in a single, larger gap.

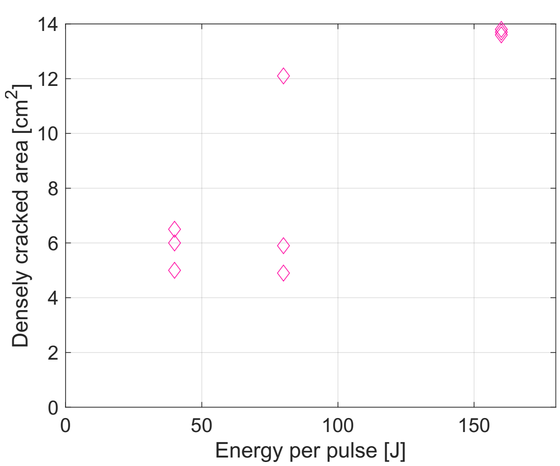

Figure 5.18: Densely cracked region extent with varying pulse energy - Courtesy of X. Tang, Dr. D. Staack and C. Adkins at Texas A&M's Plasma Engineering and Non-Equilibrium Processing Laboratory

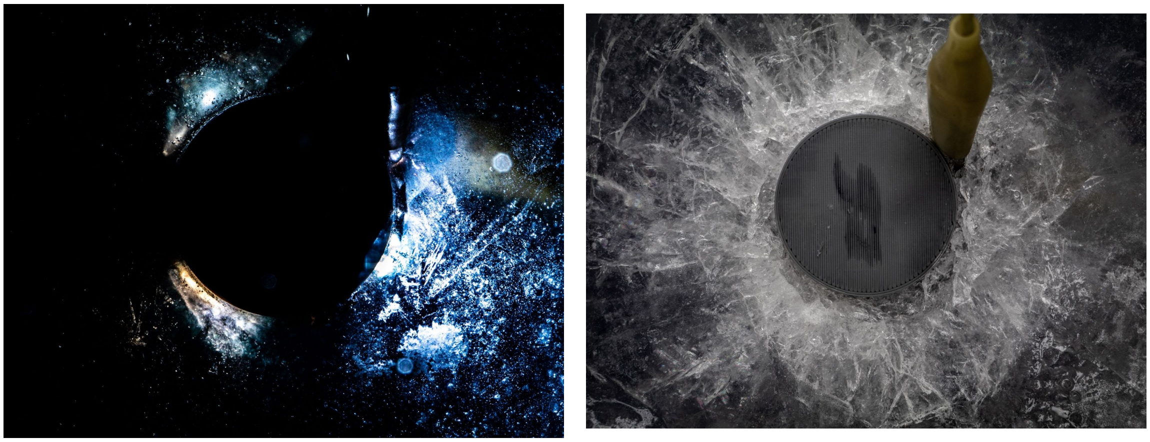

(a) Discharge (b) Aftermath

Figure 5.19: Three-gap discharge event and aftermath

Although quantitative results are lacking and the gap distance was not constant between experiments, this anecdotal evidence suggests to modify the sparking module to have fewer, larger gaps.

To test this hypothesis without having to redesign radically the sidewall-sparking module, a continuous electrical path is made by increasing the number of screws above the $0mm$ in-ice distance value, thus causing a continuous overlap. Three screws separated by a 120 degree interval are then removed from the pattern therefore achieving the desired configuration with only three larger gaps.
As can be seen in figure 5.19, the cracking which results from using fewer, larger gaps each dissipating more energy than the equally spaced case is promising.

Another problem often observed with both the 3 and $20 - 30$ gap configurations was that even if the path of least resistance is along the helix, sometimes, the discharge occurs from positive to ground following an almost direct route (figure 5.15).
This happens because pulse-discharges are highly transient phenomena and under these circumstances, circuit inductance becomes the predominant factor when trying to predict current path. In other words, the discharge will try to minimize circuit inductance rather than resistance when the phenomena's time scales lead to very large temporal gradients. This is not an absolute law, as resistance also counts when determining discharge paths, but the important takeaway is that in order to increase the chance of having a discharge follow the desired path, it is useful have it coincide with both the path of least resistance and the path of least inductance. In addition, this also leads to less ringing and EMI which counts as another argument in favour of lower circuit inductance.

Inductance reduction can be achieved by minimizing circuit loop area which in practice translates into routing the return cable along the helical path such as in figure 5.20.

This inductance reduction scheme was successful and it resulted in reliable discharge behaviour, with no short-cutting observed for more than 10 consecutive discharges.

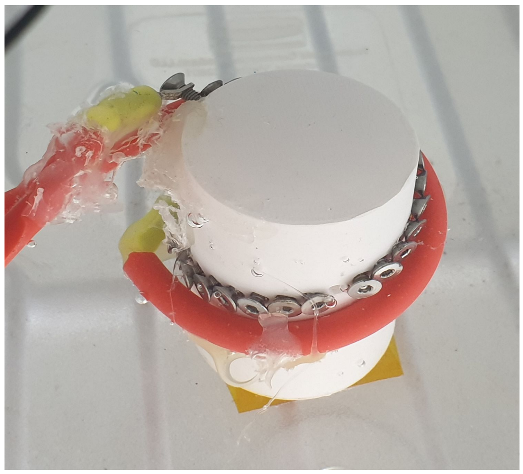

Figure 5.20: Lower inductance, three-gap discharge.

5.2.4 Plasma drill continued

Having investigated the sidewall discharging technique, remaining challenge is to integrate the high voltage module it in a functioning thermal probe.

Plasma drill V2

The sidewall discharging module has to be constructed out of electrically insulating materials, which usually are not good thermal conductors. There are materials - mostly ceramic - which are both good electrical insulators and good thermal conductors - such as Beryllium Oxide or diamond - but their niche application requires specialized equipment to fabricate and thus was not considered in this phase of the project.
When considering also the requirement of having a water-proof module, the only available manufacturing technique is Stereo-Lithography.
In addition, the previous thermal probe experiments showed the importance of having a tip with high thermal conductivity; thus, the logical placing for a sidewall discharging module is just aft from the tip-assembly. In this way, the tip heater module can be manufactured out of Aluminium which is sufficiently good for ice-penetration (Ideally it would be made out of Copper as it has a higher thermal conductivity, but Aluminium is cheaper and easier

to machine). Additionally, the high-voltage module remains close enough to the probe's tip that any cracking-induced thermal conductivity reductions are felt by most of the probe's sidewalls.

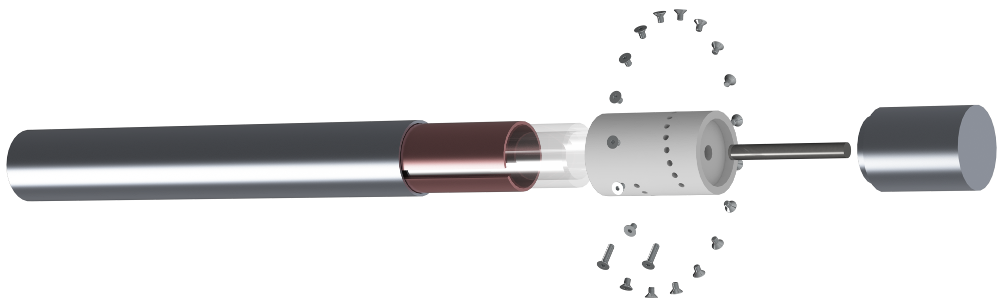

Figure 5.21: Plasma drill V2 render, exploded view.

The plasma drill V2 is a modification of the thermal probe's second version. It was designed before the conclusion of the sidewall discharging tests and therefore is characterised by equally spaced floating electrodes instead of fewer, larger gaps. Positive and ground screws are significantly longer than all other floating electrodes as they have to pass through the module's external walls. This allows for M2.5 through-hole binding post to be used as both a mechanical and electrical connector. In fact, solder does not stick to the carbon steel which comprises M2.5 screws; the Aluminium binding post on the other hand, is compatible with the use of solder.
The "upper" screw connects to the positive wire, while the lower screw is grounded via a wire which follows internally the helical path backwards to minimize circuit inductance.
There module is closed off on the lower surface, which allows to pot the everything with thermally conductive, electrically insulating epoxy which should protect from internal arcing.
Cables coming from the tip assembly are routed through an internal tube which is built-in the high voltage module itself along the symmetry axis.
This module is connected to the rest of the probe through a permanent Silicon seal. This particular iteration was abandoned before construction and testing in favour of a larger diameter, threaded system.

Plasma drill V3

The transition to the threaded thermal probe design was used as a pretext to redesign the plasma drill's high voltage module around a a three-gap setup.
Screws and their through-hole connectors are still used as electrodes, but the connection between gaps occurs via regular cabling in the module itself - the external conductive channel made out of overlapping screws is obviously eliminated in favour of an internal path. A schematic of the discharge structure can be seen in figure 5.22; note that the side-walls should be where the threaded part of the screws is.
Cables are soldered to the through hole connectors and the return wire follows the helical path backwards to reduce inductance. In this 3 gap configuration, there is no real risk of the discharge path short-cutting from the positive electrode straight to ground as they are 120 degrees apart. Nevertheless, the inductance reduction measure is still desirable to reduce EMI and circuit ringing.

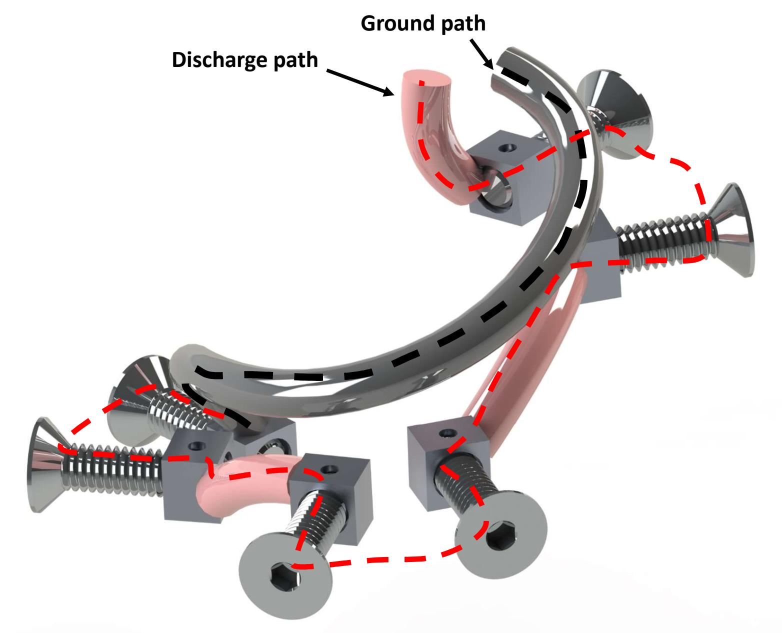

Figure 5.22: Sidewall discharge path schematic.

This high voltage module is intended to be integrated in the thermal probe V3, which is based on a threaded pipe-caps configuration with a PCB heater in the tip. The discharge

module structure has NTP threads on both ends, one male and the other female which allow for rapid mounting and unmounting (the male thread goes into the tip-assembly while the female side connects to the main body).
The housing structure is printed out of SLA and ample space is left in the middle to account for future modifications. All the internal space that is not devoted to tip cable routing or discharge cabling is supposed to be potted with thermally conductive epoxy.
As stated previously, NTP threads are supposed to be water-tight if sufficiently torqued. Waterproofing testing showed that while metal to metal NTP connections are indeed water-tight, metal to SLA is not intrinsically waterproof. In this case, having a water-tight seal requires to place some Teflon tape on the metal thread when assembling this version of the plasma drill.
The tail tube has a sufficiently large internal diameter to house two high-voltage wires with all the heaters and thermocouples. In addition, the fact that all cabling passes axially means that the tail cap can be screwed and unscrewed in place without risking to twist and break any wires.

Figure 5.23: Plasma drill V3 section render.

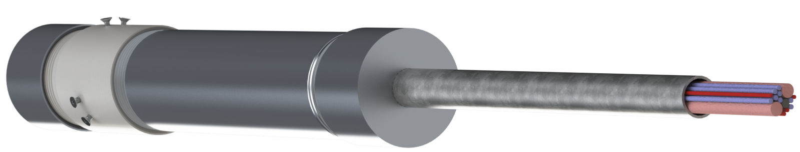

Figure 5.24: Plasma drill V3 render with cabling in the tail.

Internal arcing protection

Looking at figure 5.22 it is evident that there is a substantial risk of internal arcing between the through-hole connectors. If the holes were to follow a radial path, the internal section would have a smaller gap than the external section, even considering a flat-head screw; therefore, the internal gap would have both the least inductance and the least resistance which would certainly lead to consistent internal arcing.
There are a number of actions which have been taken to reduce the risk of internal arcing. The first and probably the most important is to incline the holes through which the screws pass in such a way that the distance between screw tips is reduced and internal connectors are pushed farther apart - as can be seen in figure 5.25. Consequently, the path of least resistance is shifted to the outer path.

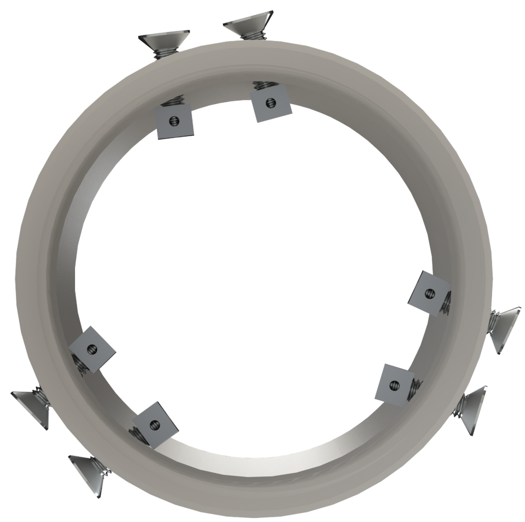

Figure 5.25: High voltage module with flat-head screw electrodes - top view.

Another way to improve the likelihood of the discharge following the desired path is to increase the dielectric strength of the region between connectors.

Figure 5.26 shows a test in which the same geometry as in figure 5.25 is used with two thin layers of a high voltage protective coating with a dielectric strength in excess of 150 kV/mm called "Super Corona Dope". The discharge path with this configuration is entirely internal and the result would not change when performing the test in ice, as the in-ice path resistance would be even higher than through air, which would make internal arcing even more likely.

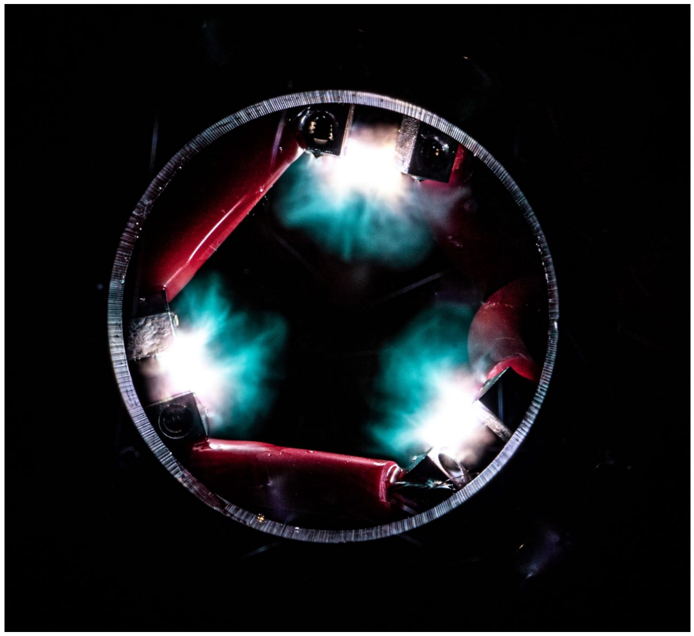

Figure 5.26: Unsuccessful use of super corona dope as an internal arcing mitigation strategy.

Before transitioning to a more aggressive geometry, an attempt was made to insulate the space between connectors with a high-temp Silicone epoxy. In fact, Silicone compounds have good dielectric strength ($> 17kV/mm$) and high-temp Silicone specifically, has high viscosity which allows for a localized application precisely between connectors where it is most needed. The problem of using this kind of epoxy is that the manufacturing process becomes significantly more complicated as much care has to be placed in avoiding air bubbles which would nullify the insulating effort.
This problem can be observed in figure 5.27 where one gap is successfully protected by the silicone potting, while the insulation around another gap probably has a number of air bubbles which results in internal arcing.

The correct manufacturing procedure requires that the silicone gun's tip or some other object (such as tweezers or a screw driver) be used to homogenize the Silicone compound before the curing process. Figure 5.27 shows a second attempt at internal insulation using high-temp silicone which resulted in consistent, successful discharges.

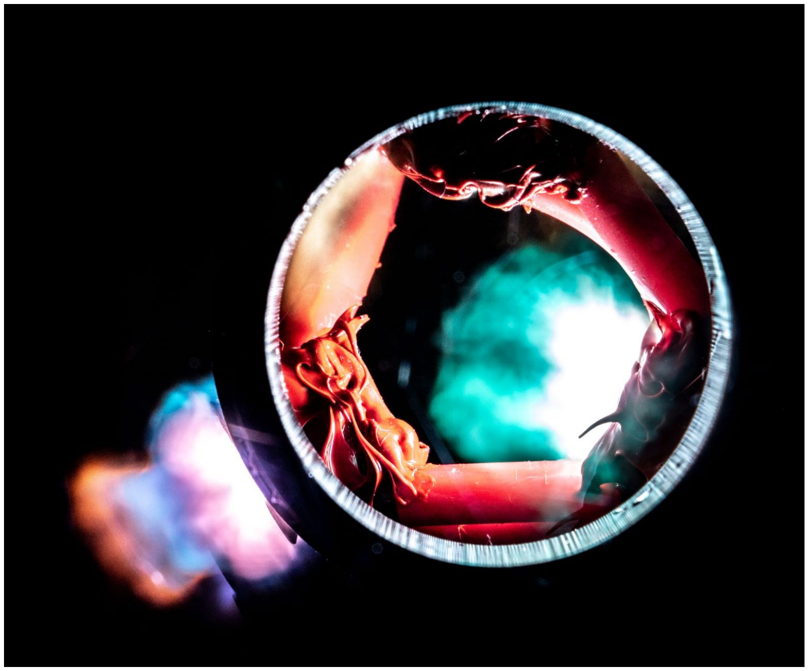

Figure 5.27: Air bubbles in the Silicone pot lead to internal arcing.

With tests in figure 5.27 the internal arcing problem is solved, but a number of improvements are still possible.
Firstly, all the difficulties in applying the internal insulation uniformly can be removed by using a lower viscosity epoxy. In fact, most thermally conductive epoxies have a dielectric strength of 15-20kV/mm which is in the same order of magnitude as high-temp Silicone. With these epoxies, the low viscosity takes care of making the insulating material permeate all the space in-between gaps and thus the whole sparking module can be potted accordingly. This thermal epoxy's homogeneity can be further improved by favouring out-gassing by curing in a vacuum chamber at the recommended temperature (usually higher than ambient conditions).
The easiest way to fully pot the high voltage module is by having an epoxy-retaining structure on the structure's lower surface. With such a feature, it suffices to pour the epoxy up to the desired level without having to use a removable support (like tape). This feature also requires to design a feed through for the cable coming from the tip.

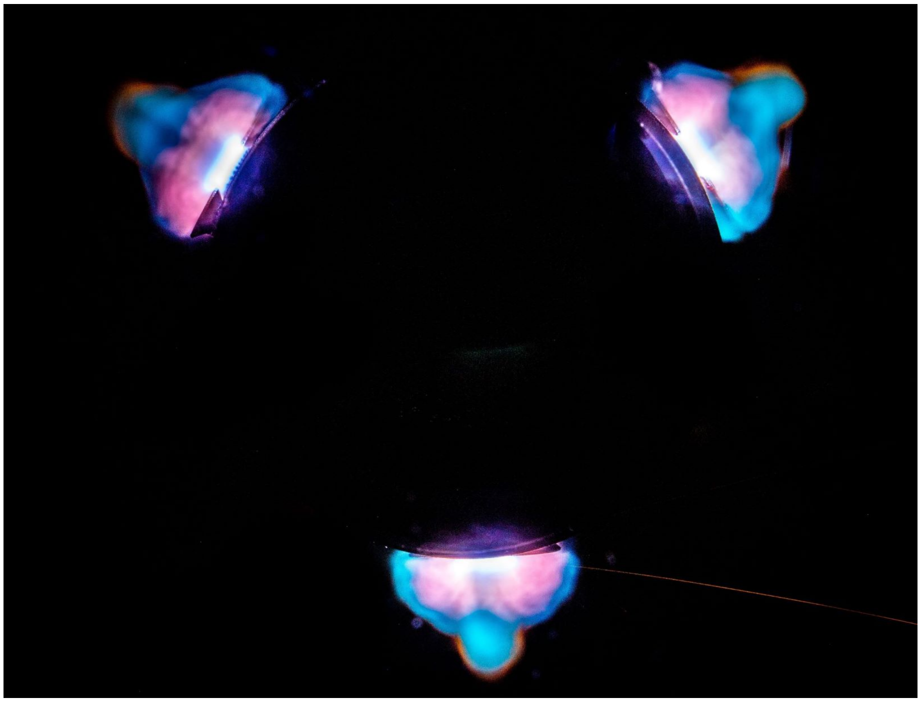

Figure 5.28: Success of internal arcing mitigation strategies.

Internal arcing can be made even less likely by increasing the angle between electrode. Beyond 40 degrees, flathead screws have to be substituted by head-less set-screws, to avoid parts of the screw from touching the sidewalls. This more aggressive geometric solution can be seen in figure 5.29.
This last configuration should be even better at mitigating internal arcing and the use of set-screws would also provide less in-ice electrode surface with respect to flat-head screws thus reducing the risk of stalling due to an electrode freezing in-ice.
Note also how there are no design features specifically aimed at waterproofing the electrode's feed-through, this is because the high voltage module's waterproofing is ensured by the potting compound.

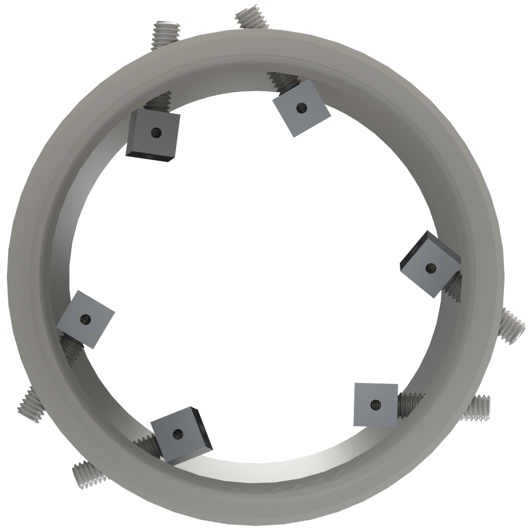

Figure 5.29: Discharge module with set-screws and more aggressive geometry.

5.3 Thermal probe and plasma drill experimental setup

The plasma drill and thermal probe should be compared directly against each other in order to judge their performance characteristics in the same environment. The main testing requirement can be expressed as measuring the energy consumed by the two systems when penetrating a certain depth of ice or alternatively measuring penetration rate at a fixed power.

The experiment has to be performed in the presence of an ice reservoir, whose temperature should be kept at a constant value to reduce the number of parameters that may affect results. The commercial freezer used to prepare the ice samples for the thermal conductivity experiments is well suited for the task of housing this setup as its internal volume can easily contain a bucket with diameter of $15 - 18$ inches with space to spare for a framing structure. In addition, the available vertical space is of 52 inches which grants ample probe travel.

Figure 5.30 shows a schematic for the experimental setup with its most important components.

The probe is vertically constrained by a guiding mechanism which clamps the metal "tail" tube. This part is important to allow test reproducibility as an unconstrained classical thermal probe is unstable and tends to topple over when penetrating ice [77].

The optimal use of the 52 inches of vertical space is characterised by the guide length equal to the ice depth. In this way all the probe is constrained throughout its whole de-

scent and all of the vertical space is used (Note that the probe's own length ($13''$) is seen as wasted space and the optimal ice depth is then $(0.5 \cdot (52'' - 13''))$). Alternatively, the probe could be frozen in at the beginning of the experiment, thus achieving "fully submersed" ice penetrations throughout the experiment. In this case, the guide would be 19.5" and the ice bucket would be 32.5" tall; the main problem with this last configuration would likely relate to the process of "probe insertion" and "removal", which would require the whole ice/water bucket to be extracted out of the freezer with probe and annexed framing.
The ice container is a high aspect ratio water drum which is trimmed to the desired height. An 8020 framing structure is used to maintain all components in position. Additionally, a spring potentiometer is used to measure displacement and is attached to the probe's tail end section. A number of waterproof thermocouples can be embedded in ice on small mounting structures thus allowing temperature gradients visualization. All low-voltage cables are fed to a PCB enclosed in a box situated in the freezer while high voltage cables are fed outside, through a manual cut-out, towards the high voltage generation and storage system, which in turn is located on a bench-top close to the freezer.

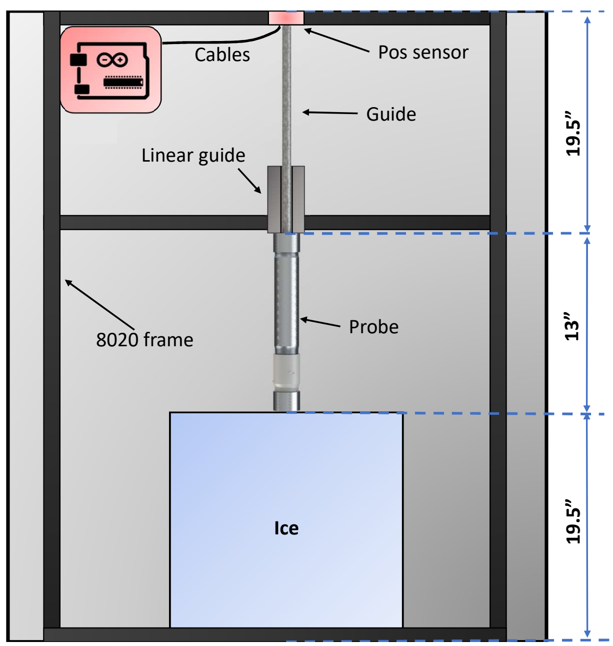

Figure 5.30: Freezer setup schematic.

The support framing is made out of 2 main sections. Firstly, there is a large parallelepiped which encloses the whole setup. It serves the purpose of being the skeleton which all other assemblies are mounted to and it is made out of 2" 8020 extruded Aluminium which provides mechanical sturdiness and design flexibility due to the abundance of mounting points. The frame is kept together using L-brackets and it is laid down on the freezer's lower plate.

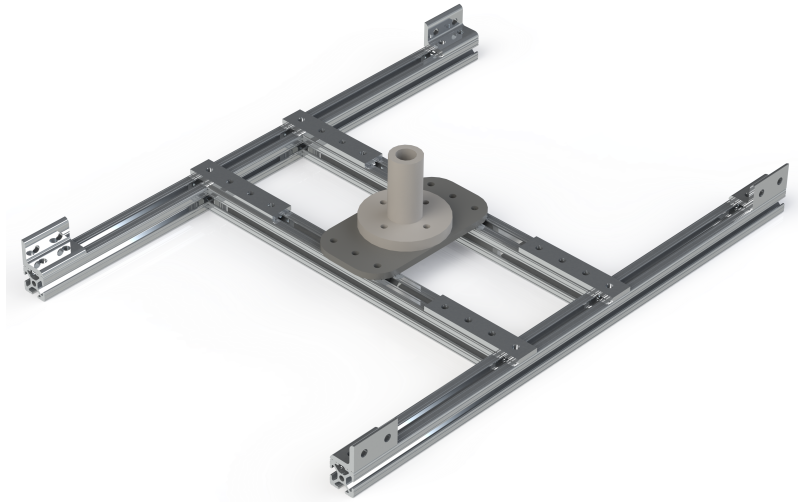

Figure 5.31: Probe guiding mechanism and relative framing.

The second part of the frame (figure 5.31) is a mounting structure for the guide mechanism. The main feature of this assembly is the ease of mounting and unmounting from the external skeleton frame by using four, two-slot L-brackets. The guiding mechanism is also easily removable and it is made out of a 3D printed tube which is screwed onto a laser-cut acrylic plate - used for its more homogeneous surface finish - which in turn rests on top of the removable mounting structure and is connected to it by the use of screws and fasteners.
Figure 5.32 shows the connection between probe tail, potentiometer and framing. The metal tube which functions as the probe's tail is inserted in a 3D printed component where two set-screws ensure a rigid connection. All the cables coming from the probe can be fed through a hole on the 3D printed connector's side.

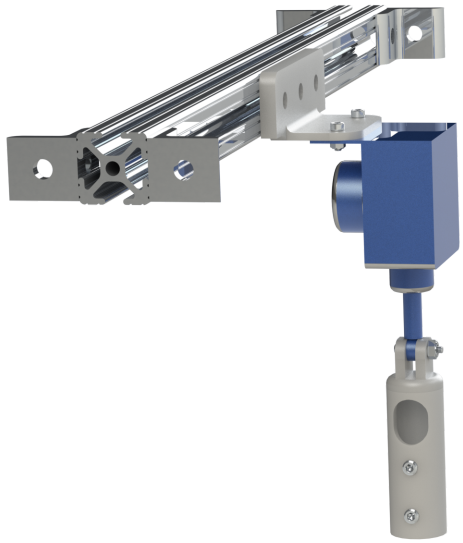

Figure 5.32: Potentiometer (in blue) with framing and 3D printed connector.

A hinge mechanism interfaces the tail-holder with the potentiometer which in turn is connected to the main frame via a 3D printed L-bracket. The spring potentiometer measures linear displacement by using a spooling spring, a constant torque spring and a rotation sensor, this means that exact alignment of the potentiometer's body is not paramount to measuring accuracy - this is why a 3D printed mounting mechanism, which might deform under the potentiometer own weight, is allowable.

Unfortunately, the rapid spread of SARS-Cov-2 in the United States resulted in the restriction of access to the Jet Propulsion Laboratory to all non-essential personnel. Therefore, the experimental setup and the final iteration of both thermal probe and plasma drill were neither fully constructed nor tested.

Figure 5.33: Thermal probe / plasma drill experimental setup complete render. The freezer is set as a transparent component.

Conclusions

This investigated the potential of pulsed plasma discharges as a performance enhancer for thermal probes.
The first part of this work consisted in the adaptation of a melt probe simulation pipeline to mimic the effects of plasma discharges in the ice-domain. Fractured ice has a lower thermal conductivity than regular ice and therefore a plasma drill, which is surrounded by a layer of fractured ice, loses less heat via conduction than a regular thermal probe.
A high voltage storage and distribution system capable of delivering $80J$ at $40kV$ was designed, constructed and iterated upon. This system is based on a power supply, a capacitor, a spark gap and a safety / telemetry collection apparatus. The high voltage system was consequently used in combination with a commercial thermal properties analyzer (KD2-pro) to derive the thermal conductivity reduction which occurs as a consequence of pulsed plasma discharges. Three main cracked regions were identified which are here reported in order of increasing distance from the electrodes. Firstly there is a region characterized by a quasi-pulverized ice shard dust. This region has thermal conductivity reduction values of up to 25%. Secondly, there is a densely cracked region which appears as mangle of radial and longitudinal cracks. This second region is characterized on average by a 15% reduction of thermal conductivity. The last region is characterized by large cracks likely following lines on which stress accumulated during the sample freezing process.
All the necessary steps to perform a direct experimental comparison between a regular thermal probe and a plasma-enhanced thermal probe have been taken. Specifically, a melt probe has been designed, tested and iterated upon and similarly, a high-voltage sparking module has also been designed and tested.
The thermal probe is based on the use of flexible heaters and a PCB heater inside of a tube with threaded end-caps. The high voltage module leverages the insight gained from the simulation by focusing on sidewall discharging, as the majority of a melt probe's power budget in cryogenic ice is spent to avoid refreezing along the sidewalls. In practice, this module guides the discharge along a helical path along which there are 3 spark-gaps.
The infrastructure necessary to complete the direct comparison was also designed and partially constructed. The main components are a commercial grade freezer, a frame, a guiding mechanism, position and temperature sensors and a micro-controller.
Unfortunately, due to the spread of SARS-CoV-2 in the United States, the direct experi-

mental comparison was not completed.
Some key aspects still need to be investigated. The most important item is the completion of a direct experimental comparison between a thermal probe and a pulsed plasma - enhanced thermal probe.
The simulation environment could also be enriched by including gravity effects and viscous dissipation and the cracked domain could be further refined. Furthermore, a trade study could be conducted to determine if the power savings provided by discharging would translate to overall mission savings (*e.g.* less launch mass, enabling the use of solar panels where previously impossible). The effects of pulsed discharges should also be more thoroughly investigated with varying system and ice parameters (Voltage, Capacitance, Temperature, Pressure *etc.*).
Finally, penetrating ice solely with pulsed plasma discharges should be investigated.

Acknowledgements

The research was carried out at the Jet Propulsion Laboratory, California Institute of Technology, under a contract with the National Aeronautics and Space Administration (80NM0018D004).

List of Figures

List of Tables

Bibliography

[1] J Klinger. Extraterrestial ice. a review. *The Journal of Physical Chemistry*, 87(21):4209–4214, 1983.

[2] AM Lagrange, DE Backman, P Artymowicz, V Mannings, AP Boss, and SS Russell. Protostars and planets iv, 2000.

[3] Christopher F Chyba and Cynthia B Phillips. Possible ecosystems and the search for life on europa. *Proceedings of the National Academy of Sciences*, 98(3):801–804, 2001.

[4] L Hays, L Achenbach, J Bailey, RK Barnes, JA Baross, C Bertka, and RD Wordsworth. Nasa astrobiology strategy 2015. *Retrieved from the NAI website https://nai. nasa. gov/media/medialibrary/2015/10/NASA_Astrobiology_Strategy_2015_15100*, 8, 2015.

[5] Planetary science and astrobiology decadal survey 2023-2032. https://www.nationalacademies.org/our-work/planetary-science-and-astrobiology-decadal-survey-2023-2032.

[6] John C Priscu, Edward E Adams, W Berry Lyons, Mary A Voytek, David W Mogk, Robert L Brown, Christopher P McKay, Cristina D Takacs, Kathy A Welch, Craig F Wolf, et al. Geomicrobiology of subglacial ice above lake vostok, antarctica. *Science*, 286(5447):2141–2144, 1999.

[7] Brent Sherwood, Jonathan Lunine, John Elliott, Travis Imken, Morgan Cable, Sascha Kempf, Ben Southworth, Scott Tucker, J Hunter Waite, Andreas Frick, et al. Sylph: life detection probe for a europa plume. 2016.

[8] Stanton J Peale, P Cassen, and Ray T Reynolds. Melting of io by tidal dissipation. *Science*, 203(4383):892–894, 1979.

[9] Jonathan I Lunine. Ocean worlds exploration. *Acta Astronautica*, 131:123–130, 2017.

[10] Matthew S Dodd, Dominic Papineau, Tor Grenne, John F Slack, Martin Rittner, Franco Pirajno, Jonathan O'Neil, and Crispin TS Little. Evidence for early life in earth's oldest hydrothermal vent precipitates. *Nature*, 543(7643):60–64, 2017.

[11] William Martin, John Baross, Deborah Kelley, and Michael J Russell. Hydrothermal vents and the origin of life. *Nature Reviews Microbiology*, 6(11):805–814, 2008.

[12] J Hunter Waite, Christopher R Glein, Rebecca S Perryman, Ben D Teolis, Brian A Magee, Greg Miller, Jacob Grimes, Mark E Perry, Kelly E Miller, Alexis Bouquet, et al. Cassini finds molecular hydrogen in the enceladus plume: evidence for hydrothermal processes. *Science*, 356(6334):155–159, 2017.

[13] Shane Byrne. The polar deposits of mars. *Annual Review of Earth and Planetary Sciences*, 37:535–560, 2009.

[14] CJ Bierson, RJ Phillips, IB Smith, SE Wood, NE Putzig, D Nunes, and Shane Byrne. Stratigraphy and evolution of the buried co2 deposit in the martian south polar cap. *Geophysical Research Letters*, 43(9):4172–4179, 2016.

[15] MH Hecht, KE Fishbaugh, S Byrne, KE Herkenhoff, SM Clifford, TN Titus, and O Aharonson. Next steps in mars polar science: In situ subsurface exploration of the north polar layered deposits. In *AGU Fall Meeting Abstracts*, 2009.

[16] Isaac B Smith, Serina Diniega, David W Beaty, Thorsteinn Thorsteinsson, Patricio Becerra, Ali M Bramson, Stephen M Clifford, Christine S Hvidberg, Ganna Portyankina, Sylvain Piqueux, et al. 6th international conference on mars polar science and exploration: Conference summary and five top questions. *Icarus*, 308:2–14, 2018.

[17] Christopher P McKay. The search for life on mars. In *Planetary and Interstellar Processes Relevant to the Origins of Life*, pages 263–289. Springer, 1997.

[18] Space Studies Board, National Research Council, et al. *Vision and voyages for planetary science in the decade 2013-2022.* National Academies Press, 2012.

[19] Mark Buchanan. Colonizing mars. *Nature Physics*, 13(11):1035–1035, 2017.

[20] Pavel G Talalay. *Mechanical ice drilling technology.* Springer, 2016.

[21] Gary D Clow, Bruce Koci, et al. A fast mechanical-access drill for polar glaciology, paleoclimatology, geology, tectonics and biology. 2002.

[22] Stephan Ulamec, Jens Biele, Oliver Funke, and Marc Engelhardt. Access to glacial and subglacial environments in the solar system by melting probe technology. In *Life in Extreme Environments*, pages 1–24. Springer, 2006.

[23] K Philberth. Geophysique-une methode pour mesurer les temperatures a linterieur dun inlandsis. *COMPTES RENDUS HEBDOMADAIRES DES SEANCES DE L ACADEMIE DES SCIENCES*, 254(22):3881, 1962.

[24] Herbert T Ueda and Donald E Garfield. *Core drilling through the Antarctic ice sheet.* Corps of Engineers, US Army, Cold Regions Research and Engineering Laboratory, 1969.

[25] K. Schüller and J. Kowalski. Melting probe technology for subsurface exploration of extraterrestrial ice – critical refreezing length and the role of gravity. *Icarus*, 317, 2019.

[26] Haldor WC Aamot. The philberth probe for investigating polar ice caps. 1967.

[27] Norbert I Kömle, Patrick Tiefenbacher, Peter Weiss, and Anastasiia Bendiukova. Melting probes revisited–ice penetration experiments under mars surface pressure conditions. *Icarus*, 308:117–127, 2018.

[28] Melanie Treffer, Norbert I Kömle, Günter Kargl, Erika Kaufmann, Stephan Ulamec, Jens Biele, Alexander Ivanov, and Oliver Funke. Preliminary studies concerning subsurface probes for the exploration of icy planetary bodies. *Planetary and Space Science*, 54(6):621–634, 2006.

[29] DF Woerner et al. Next-generation radioisotope thermoelectric generator study final report. In *JPL D-99657*. Jet Propulsion Laboratory, 2017.

[30] Pavel G Talalay. *Thermal Ice Drilling Technology.* Springer, 2019.

[31] Thomas Cwik, Wayne Zimmerman, and Miles Smith. An architecture for a nuclear powered cryobot to access the oceans of icy worlds. In *Nuclear and Emerging Technologies for Space, American Nuclear Society Topical Meeting, American Nuclear Society, La Grange Park, IL. Available online at http://anstd. ans. org/NETS-2019-Papers/# abstract-122*, 2019.

[32] William Stone, Bart Hogan, Vickie Siegel, John Harman, Chris Flesher, Evan Clark, Omkar Pradhan, Albin Gasiewski, Steve Howe, and Troy Howe. Project valkyrie: Laser-powered cryobots and other methods for penetrating deep ice on ocean worlds. In *Outer Solar System*, pages 47–165. Springer, 2018.

[33] Joan C Horvath, Frank D Carsey, James A Cutts, Jack A Jones, Elizabeth D Johnson, Bridget M Landry, Arthur L Lane, Gindi Lynch, Kenneth C Jezek, Julian Chela-Flores, et al. Searching for ice and ocean biogenic activity on europa and earth. In *Instruments, Methods, and Missions for the Investigation of Extraterrestrial Microorganisms*, volume 3111, pages 490–500. International Society for Optics and Photonics, 1997.

[34] E Eshelman, R Bhartia, G Wanger, M Willis, B Carrier, W Abbey, M Malaska, LW Beegle, L DeFlores, J Priscu, et al. Wireline analysis tool for subsurface obser-

vation of northern ice sheets (watson). In *Lunar and Planetary Science Conference*, volume 48, 2017.

[35] Kris Zacny, Honeybee Robotics, Juergen Mueller, Tighe Costa, Tom Cwik, Andrew Gray, Wayne Zimmerman, Paul Chow, Fredrik Rehnmark, and Grayson Adams. Slush: Europa hybrid deep drill. In *2018 IEEE Aerospace Conference*, pages 1–14. IEEE, 2018.

[36] Slush – the search for life using submersible heated drill. https://honeybeerobotics.com/portfolio/slush/.

[37] WC Stone, B Hogan, V Siegel, S Lelievre, and C Flesher. Progress towards an optically powered cryobot. *Annals of glaciology*, 55(65):2–13, 2014.

[38] Omkar Pradhan, Srikumar Sandeep, Albin J Gasiewski, and William Stone. Design of a forward looking synthetic aperture radar for an autonomous cryobot for subsurface exploration of europa. In *2017 IEEE International Geoscience and Remote Sensing Symposium (IGARSS)*, pages 1012–1015. IEEE, 2017.

[39] Brian H Wilcox, Jason A Carlton, Justin M Jenkins, and Fletcher A Porter. A deep subsurface ice probe for europa. In *2017 IEEE Aerospace Conference*, pages 1–13. IEEE, 2017.

[40] Konstantinos Konstantinidis, Claudio L Flores Martinez, Bernd Dachwald, Andreas Ohndorf, Paul Dykta, Pascal Bowitz, Martin Rudolph, Ilya Digel, Julia Kowalski, Konstantin Voigt, et al. A lander mission to probe subglacial water on saturn moon enceladus for life. *Acta astronautica*, 106:63–89, 2015.

[41] Bernd Dachwald, Jill Mikucki, Slawek Tulaczyk, Ilya Digel, Clemens Espe, Marco Feldmann, Gero Francke, Julia Kowalski, and Changsheng Xu. Icemole: a maneuverable probe for clean in situ analysis and sampling of subsurface ice and subglacial aquatic ecosystems. *Annals of glaciology*, 55(65):14–22, 2014.

[42] H Niedermeier, J Clemens, Julia Kowalski, S Macht, D Heinen, R Hoffmann, and Peter Linder. Navigation system for a research ice probe for antarctic glaciers. In *2014 IEEE/ION Position, Location and Navigation Symposium-PLANS 2014*, pages 959–975. IEEE, 2014.

[43] J Biele, S Ulamec, M Hilchenbach, and NI Koemle. In situ analysis of europa ices by short-range melting probes. *Advances in space research*, 48(4):755–763, 2011.

[44] Mera F Horne. Thermal probe design for europa sample acquisition. *Acta Astronautica*, 142:29–36, 2018.

[45] Igor V Timoshkin, John W Mackersie, and Scott J MacGregor. Plasma channel miniature hole drilling technology. *IEEE Transactions on plasma science*, 32(5):2055–2061, 2004.

[46] LA Yutkin. Electrohydraulic effect, mashgiz. *Moscow, Russia*, 1955.

[47] BH Bergstrom. The electrohydraulic crusher. *Engineering and Mining Journal*, 162(2):134–40, 1961.

[48] Pu Cui, A-Man Zhang, Shiping Wang, and Boo Cheong Khoo. Ice breaking by a collapsing bubble. *Journal of Fluid Mechanics*, 841:287–309, 2018.

[49] WC Maurer. Advanced drilling techniques [m1. *Tulsa ok: The Petroleum Publishing Company*, 1980.

[50] Satoshi Ihara and Chobei Yamabe. Breaking of ice sheets using shock waves produced by pulsed power. *Japanese journal of applied physics*, 42(5A):L489, 2003.

[51] Satoshi Ihara and Chobei Yamabe. Breaking of ice using pulsed power. *Japanese journal of applied physics*, 43(8R):5528, 2004.

[52] I Kocis, T Kristofic, M Gebura, G Horvath, M Gajdos, and V Stofanik. Novel deep drilling technology based on electric plasma developed in slovakia. In *2017 XXXIInd General Assembly and Scientific Symposium of the International Union of Radio Science (URSI GASS)*, pages 1–4. IEEE, 2017.

[53] William M Moeny and Niels K Winsor. Electrohydraulic pressure wave projectors, April 10 2001. US Patent 6,215,734.

[54] William M Moeny and David M Barrett. Portable electrohydraulic mining drill, April 27 1999. US Patent 5,896,938.

[55] BW Johansen, P Lee, K Naesje, W Lekens, PH Sorensen, O Wetteland, B Glass, C Hoftun, and K Zacny. A new plasma drilling technology with applications for moon, asteroid, and mars exploration and isru. In *Lunar and Planetary Science Conference*, volume 45, page 2594, 2014.

[56] Haldor W.C. Aamot. Heat transfer and performance analysis of a thermal probe for glaciers. Technical report, Hanover, New Hampshire, 1967.

[57] J.C. Jaeger H.S. Carslaw. *Conduction of heat in solids.* Oxford University Press, Amen House, London E.C.4, 1959.

[58] M. Brandt, W. Zimmerman, D. Berisford, J. Mueller, M. Barry, M. Durka, R. Kristof, B. Hogan, and W. Stone. Modeling of cryobot melting rates in cryogenic ice. In *2019 IEEE Aerospace Conference*, pages 1–17, 2019.

[59] Eugene Chumachenko. Some problems associated with design of cryobots. *Cosmic Research*, 47:226–234, 06 2009.

[60] Erokhima Chumachenko, Nazirov. Specific features of cryobot movement in the ice structures of europa. *Cosmic Research*, 48:553–557, 2010.

[61] Ekaterina Zakharova and Mikhal Purin. Mathematical modeling of the melting of ice under conditions of motion of a heat drill. *MATEC Web of Conferences*, 194:01063, 01 2018.

[62] Ekaterina Zakharova, Arkadii Zakharevich, and Nadehzda Gutareva. The dynamics of ice melting in the conditions of crybot movement. *MATEC Web of Conferences*, 110:01090, 01 2017.

[63] Per-Olof Persson and Gilbert Strang. A simple mesh generator in matlab. *SIAM review*, 46(2):329–345, 2004.

[64] Francis Nimmo and Michael Manga. Geodynamics of europa's icy shell. In *Europa*, pages 381–404. University of Arizona Press Tucson, 2009.

[65] T. Kohno, H. Nakazawa, M. Kosaki, and K. Horii. Electrical breakdown of ice at cryogenic temperatures. *IEEE Transactions on Electrical Insulation*, EI-15(1):27–32, 1980.

[66] Davide Tommasini. Dielectric insulation and high-voltage issues. *arXiv preprint arXiv:1104.0802*, 2011.

[67] Kenneth L Kaiser. *Electrostatic discharge*. CRC Press, 2005.

[68] Petr Veselý, T Tichý, Ondrej Sefl, and Eva Horynová. Evaluation of dielectric properties of 3d pr inted objects based on printing resolution. *IOP Conference Series: Materials Science and Engineering*, 461:012091, 12 2018.

[69] Henry W.Ott. *Noise reduction techniques in electronic systems*. Wiley, 1988.

[70] Edward Bennett Rosa. *The self and mutual inductances of linear conductors*. Number 80. US Department of Commerce and Labor, Bureau of Standards, 1908.

[71] JJ Petrovic. Review mechanical properties of ice and snow. *Journal of materials science*, 38(1):1–6, 2003.

[72] Norman Anderson and Alex Travesset. The many phases of ice.

[73] Martin Truffer. Ice physics. *University of Alaska Fairbanks*, 2013.

[74] Armin Kleinböhl, John T Schofield, David M Kass, Wedad A Abdou, Charles R Backus, Bhaswar Sen, James H Shirley, W Gregory Lawson, Mark I Richardson, Fredric W Taylor, et al. Mars climate sounder limb profile retrieval of atmospheric temperature, pressure, and dust and water ice opacity. *Journal of Geophysical Research: Planets*, 114(E10), 2009.

[75] LJ Bonales, Antonio C Rodríguez, and PD Sanz. Thermal conductivity of ice prepared under different conditions. *International journal of food properties*, 20(sup1):610–619, 2017.

[76] Frank P Incropera, Adrienne S Lavine, Theodore L Bergman, and David P DeWitt. *Fundamentals of heat and mass transfer*. Wiley, 2007.

[77] Haldor WC Aamot. Instruments and methods: a buoyancy-stabilized hot-point drill for glacier studies. *Journal of Glaciology*, 7(51):493–498, 1968.

[78] Frank R Rack. Enabling clean access into subglacial lake whillans: development and use of the wissard hot water drill system. *Philosophical Transactions of the Royal Society A: Mathematical, Physical and Engineering Sciences*, 374(2059):20140305, 2016.

[79] Stephen M Clifford, Kenji Yoshikawa, Shane Byrne, William Durham, David Fisher, Francois Forget, Michael Hecht, Peter Smith, Leslie Tamppari, Timothy Titus, et al. Introduction to the fifth mars polar science special issue: Key questions, needed observations, and recommended investigations. *Icarus*, 225:864–868, 2013.

[80] Yoseph Bar-Cohen and Kris Zacny. *Drilling in extreme environments: penetration and sampling on earth and other planets*. John Wiley & Sons, 2009.